Effectiveness of a Serpentine Inlet Duct Flow Control Scheme at Design and Off-Design Simulated Flight Conditions

by

Angela C. Rabe

Dissertation submitted to the Faculty of the
Virginia Polytechnic Institute and State University
in partial fulfillment of the requirements for the degree of

DOCTOR OF PHILOSOPHY
in
Mechanical Engineering

Wing F. Ng, Co-Chairman
Ricardo Burdisso, Co-Chairman
Walter O'Brien
Milt Davis
Alan Hale
Peter King
Marvin Gridley, Guest Member

August 1, 2003
Blacksburg, Virginia

Key Words: AIP, Angle of Attack, Distortion, Serpentine Inlet

Effectiveness of a Serpentine Inlet Duct Flow Control Scheme at Design and Off-Design Simulated Flight Conditions

by
Angela C. Rabe
Committee Co-Chairmen: Wing F. Ng and Ricardo Burdisso
Department of Mechanical Engineering

Abstract

An experimental investigation was conducted in a static ground test facility to determine the flow quality of a serpentine inlet duct incorporating active flow control for several simulated flight conditions. The total pressure distortion at the aerodynamic interface plane (AIP) was then used to predict the resulting stability for a compression system. This study was conducted using a model of a compact, low observable, engine inlet duct developed by Lockheed Martin. A flow control technique using air injection through microjets at 1% of the inlet mass flow rate was developed by Lockheed Martin to improve the quality of the flow exiting the inlet duct. Both the inlet duct and the flow control technique were examined at cruise condition and off-design simulated flight conditions (angle of attack and asymmetric distortion). All of the experimental tests were run at an inlet throat Mach number of 0.55 and a resulting Reynolds number of $1.76*10^5$ based on the hydraulic diameter at the inlet throat.

For each of the flight conditions tested, the flow control scheme was found to improve the flow uniformity and reduce the inlet distortion at the AIP. For simulated cruise condition, the total pressure recovery was improved by ~2% with the addition of flow control. For the off-design conditions of angle of attack and asymmetric distortion, the total pressure recovery was improved by 1.5% and 2% respectively. All flight conditions tested showed a reduction in circumferential distortion intensity with flow

control. The cruise condition case showed reduced maximum circumferential distortion of 70% with the addition of flow control. A reduction in maximum circumferential distortion of 40% occurred for the angle of attack case with flow control, and 30% for the asymmetric distortion case with flow control.

The inlet total pressure distortion was used to predict the changes in stability margin of a compression system due to design and off-design flight conditions and the improvement of the stability margin with the addition of flow control. A parallel compressor model (DYNTECC) was utilized to predict changes in the stability margin of a representative compression system (NASA Stage 35). Without flow control, all three cases show similar reduced stability margins on the order of 30% of the original stability margin for NASA Stage 35 at 70% corrected rotor speed. With the addition of flow control, the cruise condition tested improved the stability margin to 80% of the original value while the off-design conditions recover to 60% of the original margin. Overall, the flow control has been found to be extremely beneficial in improving the operating range of a compression system for the same inlet duct without flow control.

Acknowledgements

I would like to thank my co-advisors, Dr. Wing Ng and Dr. Ricardo Burdisso, for their support and guidance throughout my work. I would also like to thank the rest of my committee members: Dr. Walter O'Brien, Dr. Milt Davis, Dr. Alan Hale, Dr. Pete King, and Skip Gridley, for all of the time they devoted to this work and for the expertise they provided. Their efforts have improved the quality of this work. In addition, I am grateful for the setup that allowed this work to take place. The work began as an SBIR Phase II Research project awarded to Techsburg and succeeded through the collaboration of Virginia Tech, Techsburg, Air Force Research Labs, and Lockheed Martin. Without this combined focus and support this project would not have been possible. I would also like to thank members of these organizations, specifically Dr. Semih Olcmen, Dan Miller, and Phil Truax for their technical support. I would like to thank Lockheed Martin for the data they provided in addition to their critical role in the project. A special thank you to Greg Dudding and other machinists who provided rapid turn around on all of the manufacturing requirements for this project. Without their special efforts the project could not have finished on time. A special thank you also to Jason Anderson who shared the early burden involved in the development of a large scale experimental setup.

Finally, I would like to thank those without whom I may never have begun this endeavor, much less completed it. My family provided continuous support and encouragement, in addition to their technical support. I would also like to thank my friends who patiently listened to my frustrations throughout the more stressful portions of this process. Lastly, I thank God. Without His love and guidance in my life I never could have finished this.

Table of Contents

List of Figures

List of Tables

Nomenclature

AIP	Aerodynamic interface plane
a_n	Fourier series cosine coefficient
$Area_{P\text{-}low}$	Area of low-pressure region
b_i	Slope of P(θ)
b_n	Fourier series sine coefficient
CFD	Computational fluid dynamics
FOD	Foreign object debris
K	Number of low-pressure regions
M	Mach number
N	Number of rings
n/rev	Harmonic coefficient
NR	Number of circumferential locations
P	Static pressure
P_{avg}	Ring average total pressure
P_o	Total pressure
P(θ)	Total pressure ratio at any angle θ for a given ring
PAV	Ring average total pressure
PAVLOW	Average total pressure of low total pressure region for a ring
PFAV	Face average total pressure
PR	Pressure ratio
x	Coordinate
y	Coordinate
ΔPC/P	Circumferential distortion intensity element
ΔPR/P	Radial distortion intensity element
γ	Specific heat ratio
θ	Circumferential location in degrees
θ^-	Extent of low pressure region

1.0 Introduction

1.1. Background and Motivation

As aircraft continue to evolve, the requirements for their development are becoming more and more stringent. For military applications, the overall thrust to weight ratio requirement is increasing, demanding either lighter aircraft through length reductions or lighter materials, or more powerful engines which tend to add weight. By reducing the overall aircraft length, large weight savings may be realized with an increase in overall thrust to weight ratio for the same engines. A reduction in weight leads to lower costs and lighter, more compact high performance aircraft.

Reduction in radar cross-section is another area of design focus. With advancements in radar technology, it is necessary to continue to decrease the radar cross-section (RCS) of aircraft. Many technologies have been developed which decrease the radar cross section of an aircraft. A large reduction in RCS can be realized by eliminating the engine fan face as a radar return source. The fan face can be hidden from radar by developing an inlet duct that is offset so that there is no direct line of sight from the entrance of the inlet duct to the engine fan face. This prevents a direct path for radar beams to strike the engine fan face and return to the receiver. These ducts are included in a general class of serpentine inlet ducts.

Serpentine inlet ducts have been in existence for some time and can be found in many of today's commercial and military aircraft including the Boeing 727, F-16 and F-117. Commercial aircraft use serpentine ducts to allow the thrust vector from rear mounted engines to be aligned with the axis of the aircraft. Some examples of current aircraft with serpentine inlet ducts can be seen in Figure 1.1. The recent emphasis on

unmanned aerial vehicles (UAVs) includes the ability to take new risks in enhancing aircraft abilities and performance. Stability margins can be decreased since loss of life is no longer a concern. The developments in technology and reduction in radar cross-section requirements are leading to serpentine inlet ducts that are shorter and have larger height offsets throughout the duct. To improve aircraft thrust to weight ratio, the serpentine shape of the inlet duct is becoming more aggressive as an ultra-compact, highly offset inlet duct, allowing a reduction in the overall aircraft length. While these inlet ducts reduce the radar cross section, they also reduce the stability margin of the propulsion system. The more aggressive inlet ducts result in increased turning which in turn produces secondary flow within the duct. The compact nature of the duct limits the length for diffusion and dissipation of these secondary flows and leads to greater distortion levels at the engine fan face. This inlet distortion can produce a reduction in stability margin for the compressor or fan of the turbine engine. In addition, inlet distortion can result in high cycle fatigue, which may lead to catastrophic loss of aircraft, loss of aircraft operability, and increased maintenance costs.

Figure 1.1 Examples of Current Aircraft with Serpentine Inlet Ducts

There are several design challenges posed by these serpentine inlet ducts. In many cases, the flow from the inlet duct is not of an acceptable flow quality for the engine airflow. The flow must be controlled or corrected to improve the flow quality entering the turbine engine. Several attempts to control the flow within the duct and improve exit flow uniformity have been demonstrated and will be discussed in the literature review. Additionally, the secondary flow generated within the serpentine duct will be more severe at off-design conditions for these more aggressive serpentine ducts. Because the effect of off-design conditions is not yet well understood for these ducts, design revisions may be required in order to ensure acceptable flow quality at any condition that may occur during a flight mission. This includes off-design conditions such as angle of attack and asymmetric distortion.

With the advent of ultra compact, highly offset, diffusing, serpentine ducts, off-design conditions pose a significant design challenge. The serpentine inlet duct creates distortion at the aerodynamic interface plane (AIP), where the exit of the inlet duct meets the engine fan face, which will be ingested into the propulsion system following the inlet duct. Flight conditions such as angle of attack may increase the engine fan face distortion to unacceptable levels in terms of stability margin and/or high cycle fatigue.

The present research sought to expand the capacity of static ground testing by adding the ability to simulate different flight conditions. This research developed a method to examine the effect of off-design flight conditions such as angle of attack and an asymmetric inlet distortion similar to sideslip. In this way vehicle design can be verified through ground testing and improved computational analysis tools at an earlier design stage. These off-design flight conditions are generally tested in a wind tunnel phase following the static ground test phase. The wind tunnel testing is more expensive as the facility demands more resources and the model involves more detail, including forebody and other pertinent aircraft structures. At this stage, design changes become more expensive. This can be avoided by pre-testing off-design flight conditions in the static ground test stage.

The present research also explores the effectiveness of a specific flow control technique applied to an ultra compact, highly offset, inlet duct at design and at off-design flight conditions. The inlet duct and flow control technique were developed by Lockheed Martin. The inlet duct was tested experimentally for cruise condition, angle of attack, and asymmetric distortion flight cases to determine the change in inlet

performance and flow control performance at different flight conditions. The flow at the AIP was examined in detail to determine the characteristics of the flow from the inlet duct at varying conditions. These data were then used to predict the change in stability range of a compressor from a gas turbine engine due to the variations in incoming flow uniformity.

1.2. Literature Review

Several different aspects of duct flow have been studied in the past and are available in the literature. The nature of the flow development within a serpentine duct will be examined through past research efforts including the effects of the degree of turning, diffusing cross-sectional area (exit to entry area ratio), and transitioning cross-sectional area (continuous change in cross sectional shape). In addition, studies have been conducted examining ways to correct the flow distortion produced in these ducts. The various attempts to control the flow within a diffusing serpentine inlet duct will be reviewed. The flow exiting the inlet duct will enter the gas turbine engine. Flow non-uniformity at this stage can decrease engine performance in several ways. This will be discussed in order to understand the importance of improving the flow uniformity at the exit of the inlet duct. Finally, engine modeling techniques will be reviewed in order to find a suitable means to predict the effect of inlet distortion on a compression system. In this way the changes in flow quality can be presented in a way that demonstrates the improvement in engine operating conditions including increased stability margin.

1.2.1. Serpentine Ducts

A great deal of literature is available detailing the flow within ducts. As the design of the duct becomes more complex, there is less literature available, and the flow is not as well understood. Experiments have been conducted on simple circular ducts, circular ducts with centerline curvature, and ducts of transitioning cross-section. The circular duct experiments are popular for the simplicity of the geometry and the application to more mature aircraft systems. Much of the literature on serpentine or S-ducts is for circular cross-section ducts with two equal turns, in opposite directions, bending the flow and then exiting the flow axially. These ducts are often diffusing ducts, with increasing area streamwise along the duct and are being tested with aircraft intake duct applications. A representative serpentine or S-duct inlet is shown in Figure 1.2 along with a graphical representation of common terminology.

A numerical investigation by Kramer and Stanitz (1952) sought to better describe the behavior of real fluids in a fluid machinery environment. They investigated two-dimensional, incompressible, non-viscous shear flows in a 90^{o} elbow. With an increase in negative vorticity, the static pressure drop through the elbow diminished; however, there was only a slight change in the local pressure coefficient which was relatively similar for corresponding positions on either wall. The pressure drop along the inside of the turn was well represented as was the corresponding increase in velocity.

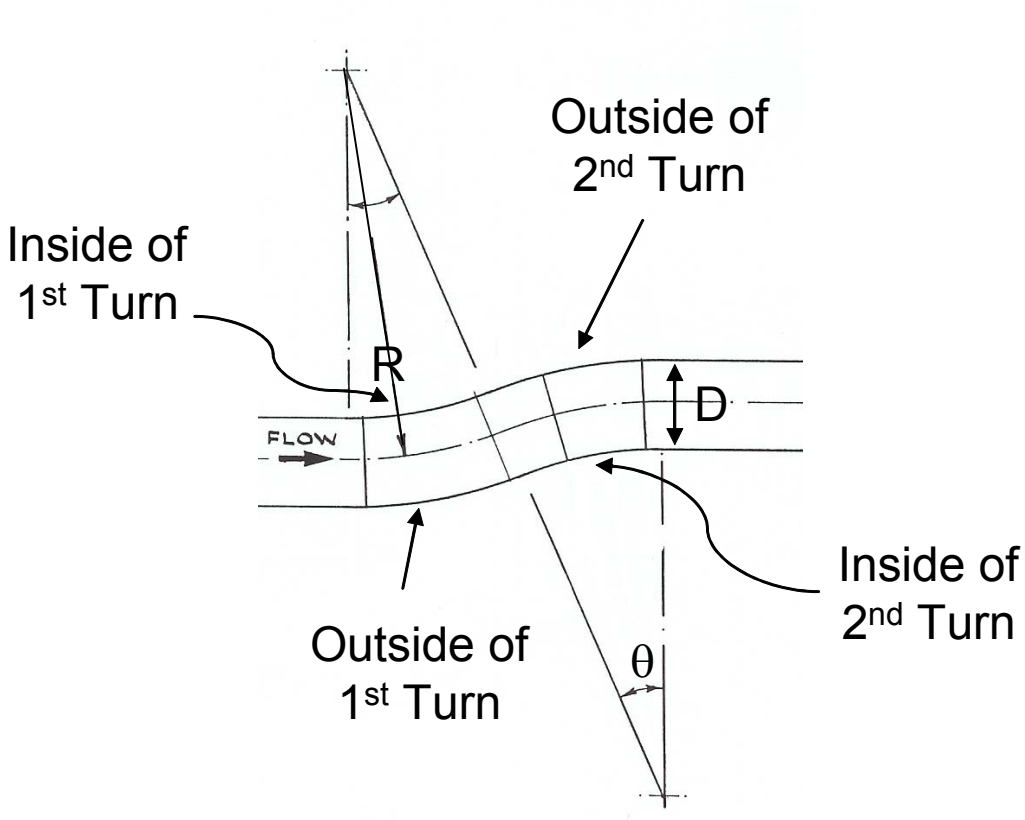

Figure 1.2 Representative S-Duct with Common Terminology

Rowe (1970) reported on flow in 180^o bends and a 45^o/45^o S-duct and compared the experimental measurements with inviscid theory. He described the counter-rotating vortices formed in turning ducts. The ducts he investigated were all of circular cross section and therefore produced vortices at the center of the inside turn. In the 180 degree bend studied, he found that over 61 pipe diameters were required for the flow to return to the pre-turn flow uniformity following the end of the bend. In the S-duct tested by Rowe, the same radius of curvature and duct cross sectional geometry as the 180 degree bend were used, but only about 13 pipe diameters were required for the flow to return to the pre-turn flow uniformity. This implies that the second turn of the S-duct tends to dissipate the effect of the first turn. In addition, in the S-duct, the flow is turned only 45

degrees at a time. Therefore, the total pressure gradient is reversed after only a quarter of the turning experienced in the 180 degree bend. This fact greatly contributes to the different recovery lengths required for the two ducts tested. In the S-duct examined here, there are no separate vortices initiated at the second turn. The distortion from the first turn begins to migrate toward the inside wall of the second turn, but no distinct pressure loss is realized by entering the second turn. This is partially due to the circular cross-sectional geometry which does not force the distortion from the two turns into different regions of the cross-sectional area. Since the duct remains circular in cross section, any secondary flow will tend towards the center of the duct. Additionally, in most S-ducts, only two turns are present resulting in a height offset and no overall change in flow direction. In a separate study, by Sullivan et al (1982), the S-duct under investigation involved two 45 degree turns. In this case flow separating vortex pairs were produced at the bottom (inside) of the first turn and the top (inside) of the second turn. This process was documented through dye injection in a water tunnel, and the results show the importance of the severity of the turn in producing secondary flow fields. A schematic of the vortex development captured through photographs is shown in Figure 1.3. Here the two sets of counter-rotating vortices formed at each turn can be seen clearly.

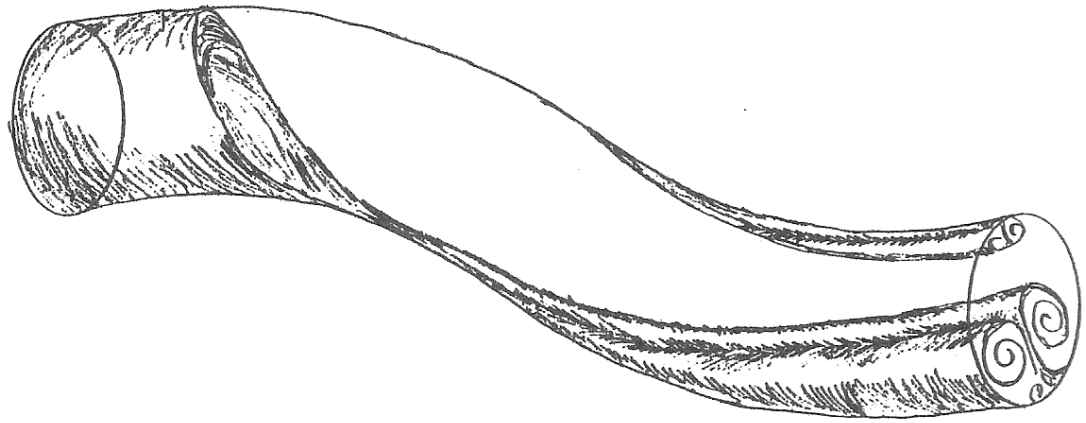

Figure 1.3 Natural Vortices in a Serpentine Duct (Sullivan et al, 1982)

Rowe (1970) also compared his results to a numerical calculation for inviscid flow. The inviscid approximation of Squire and Winter showed similar trends but failed to capture the proper area and intensity of the flow non-uniformity. The calculation does not account for any vortex dissipation due to viscosity and therefore tends to predict total pressure non-uniformity that is significantly greater than that realized in experimental testing. This same trend continues to persist in numerical calculations today.

Bansod and Bradshaw (1972) examined the flow in several different S-shaped ducts to determine the effect of different radii of curvature of the first and second turns. This study found it was beneficial to have a smaller R/D at the first turn. The shorter intake was found to have better total pressure recovery which indicates that lengthening the turns will allow more distortion to form rather than providing an opportunity for greater dissipation. However, the differences in the various inlet ducts were rather small.

Further testing would be required for more conclusive evidence of an advantage for more compact inlet ducts.

Vakili et al (1983) performed a detailed study on a $30^o/30^o$ circular cross section S-duct. They took five-port cone probe measurements at various cross sections along the duct, including the entrance and exit of the duct. Using the five-port cone probe they obtained three-dimensional velocity profiles and total and static pressures at each point. They also collected wall static pressure measurements for three streamwise profiles. The radius of curvature to duct diameter was rather large at R/D=5, and no separation of the flow was indicated through surface oil flow visualization. This study found that the secondary flow development generated at the first turn was convected throughout the duct with additional vorticity generated at the second turn, in the opposite sense. Taylor et al (1984) examined a different circular cross section S-duct with two 22.5 degree turns and an R/D of 7. This duct is also gently turning, similar to the duct tested by Vakili et al. In this study Laser-Doppler velocimetry was used to measure the three dimensional velocity profiles. The results were similar to those obtained by Vakili et al.

In a later study, Vakili et al (1985) examined a 30^o-30^o circular cross section S-duct, with an area ratio of 1.51. Here the flow was found to separate in the first turn in the form of a vortex, and did not reattach within the duct. The flow separation was determined through both wall static pressure measurements and surface oil flow visualization.

Povinelli and Towne (1986) examined inlet ducts to determine the main cause of distortion generation. They looked at transitioning cross section (with constant cross-sectional area) in combination with centerline curvature, centerline curvature alone, and

transitioning cross section alone. In this portion of the study, the centerline curvature was found to have the largest effect on the distortion generated by the inlet duct. Povinelli and Towne also tested a diffusing duct (increasing cross sectional area) which was found to produce more distortion than the centerline curvature alone.

Wellborn et al (1992) thoroughly tested a diffusing S-duct inlet with an area ratio of 1.52 and two identically shaped turns of 30^{o}. The formation of counter-rotating vortices from the inside of the first turn was observed. In this case, these vortices separated from the wall as shown through surface oil flow visualization and wall static pressure measurements. The vortices were also seen to reattach following the second turn in the duct.

The flow within a serpentine inlet duct is affected by the centerline curvature, diffusing cross section and transitioning cross section. The flow distortion produced by these design elements varies based on the design. However, all of these factors contribute to inlet distortion. With the advent of more aggressive serpentine ducts, the flow distortion requires correction prior to entering the gas turbine engine. For this reason, flow control techniques have been studied in order to improve the flow uniformity at the exit of the inlet duct.

1.2.2. Flow Control

In order to combat the effects of secondary flow within the serpentine inlet duct, several attempts to control the flow within the duct and improve exit flow uniformity have been demonstrated. The approach for inlet flow control varies: some devices employ means to energize the low momentum boundary layer while others seek to enhance mixing in the region of flow separation.

Vortex generators can be designed to direct high energy flow into the low momentum region to re-energize flow near the wall. This approach does not generally reduce secondary flow in the duct and does not always reduce total pressure distortion at the exit of the inlet duct. Furthermore, this approach involves vortex generators in the classical sense, where the generators are additions to the duct wall in the form of vanes or airfoil structures attached to the duct wall on the inside of the first turn, upstream of the turn. This approach is successful in reducing the separated region of flow along the duct wall.

Current approaches focus on the source of secondary flow within the duct, that is, the turning of the duct, which creates a series of adverse and favorable pressure gradients. An adverse pressure gradient is associated with the inside of a turn in the duct. The adverse pressure gradient at each turn leads to flow separation along the wall in a pair of counter-rotating vortices. The flow control technique for the current research involves the creation of a second pair of counter-rotating vortices opposite in direction to those formed by the duct. In this flow control approach the two sets of secondary flows tend to cancel each other out. The second set of counter rotating vortices can be formed by vane vortex generators or the injection of air through microjets. Both concepts have been explored in the past and will be presented in more detail.

Flow control can be classified in several ways. Active flow control includes an actuator to change the flow such as air injection through microjets while passive flow control includes a fixed modification to the flow such as vane or fin-type vortex generators. Closed loop flow control means that the flow control can respond to changes in the flow through a feedback loop which provides information on the flow in real time.

Closed loop flow control in a serpentine duct has only recently been examined (Anderson, 2003). Sensing technology which would enable closed loop flow control to be readily available for serpentine inlet duct applications is still in the research and development stage. Open loop flow control, on the other hand, has no feedback loop. However, it can involve different prescribed settings based on engine speed for example, with no real time corrections. The literature review that follows involves open loop flow control that can be either active or passive in nature.

Reichert and Wendt (1993) used a boundary layer energizing approach and explored the effect of different vortex generator parameters on the effectiveness of vortex generator flow control. They included the effect of vane type vortex generator height, streamwise location of vortex generator array and vortex generator spacing. There was no account for varying the spacing of the vortex generators with circumferential distance from the point of separation or any effect of varying the circumferential extent of the vortex generators. However, their study found that the axial location of the vortex generators can be very important. It is critical that the vortex generators be upstream of the point of separation. When in doubt, it is best to move them safely upstream as there is only a small penalty associated with placing the generators farther upstream of the point of separation. Placing the vortex generators too close to the point of separation, or worse, downstream of the point of separation causes them to have a minimal effect on the flow. The variation in vortex generator height had mixed effects on the flow field. Total pressure recovery was most improved with vortex generator height close to boundary layer height in the region of interest. However, continued reduction of distortion level was found by increasing the vortex generator height. A similarly confusing trend was

found by varying the spacing between the vortex generators as well as the number of vortex generators while keeping the circumferential extent of the vortex generators constant. Decreased spacing between generators was found to reduce the separation area of the flow, verified through surface oil flow visualization. However, decreasing the separation area did not increase the total pressure recovery or reduce the distortion in the flow field. These mixed results led to further testing.

In a later study, Reichert and Wendt (1994) concentrated their flow control approach on countering the secondary flow within the duct by creating vortices in direct opposition to the vortices which naturally form in a serpentine duct. This involved more knowledge of the flow field and more precise location of the vortex generators. The fin or vane type generators were still employed. With this approach, it can be easier to find the proper orientation of the vortex generators, but the manufacturing is more difficult. In addition, if the vortex generators were to break in flight they would result in foreign object debris in the engine. However, the flow control effectively eliminated the separation in the duct and improved the total pressure recovery while reducing the distortion generated within the duct. A flow control scheme was found that improved the duct flow in all aspects. This technique provided a second approach to flow control in a serpentine duct.

Jaw et al (2001) used air jets to improve the flow qualities in an engine testing environment. This flow control occurred following the inlet duct, just upstream of the engine fan face. The distortion to be controlled was provided by distortion screens and a hot air injection system to simulate inlet distortion (pressure and temperature). They sought to improve the flow distortion due to temperature variations in addition to

pressure variations. Two flow injection designs were examined. The first design provided air injection from angled holes around a circumference and met with limited success. The second approach involved a row of axially spaced injection holes which met with greater success. One important discovery from this study was an optimum injection rate. They found that with too much air injected, a secondary flow source developed, further degrading the flow. With too little air injected, the distortion generated upstream was not well abated. This work suggests that control systems will need to be optimized because additional fluid injection is not always beneficial.

There have been some more recent studies on the use of microjets as vortex generators. In some cases, the flow control consists of air jets inserting high pressure air into the flow at a specific angle to create a vortex. This approach has met with some success as well. The use of air jets allows more flexibility in the flow control technique and the air jets are generally easier to manufacture than the vane type vortex generators. However, it has been more difficult to orient the jets to have the same positive effects as the vane vortex generators. In a study by Hamstra et al (2000) such a strategy was tested with both vane type and air jet vortex generators. At most inlet Mach numbers of interest, the vane type vortex generators offered the best flow at the aerodynamic interface plane. The air jet vortex generators also successfully improved the flow but not to the degree of the vane type vortex generators. A computational fluid dynamics (CFD) study was utilized to determine the most optimal flow control configuration prior to manufacturing the model inlet. The CFD study was found to successfully predict the flow in the cases with the flow control turned on while it under-predicted the flow distortion without flow control.

In an earlier phase of the current research (Harper, 2000), a flow control technique was employed on a small scale inlet model. The model size was on the order of a four inch exit diameter. The flow control configuration tested utilized a combination of fluid removal upstream of separation and fluid injection downstream of separation. Microphone sensors were used to determine the separation region and also to evaluate the flow at the exit plane in combination with total pressure measurements. This study found success for all flow control configurations with the greatest improvement in flow quality coming from the combination of fluid removal upstream of the separation point and re-injection downstream of separation.

The above mentioned studies have shown several examples of improvement in flow-uniformity with the addition of flow control. The improvement in flow quality is important because the uncontrolled flow exiting a serpentine inlet duct poses challenges for the gas turbine engine following the inlet duct. The stability margin of the engine can be affected by the flow non-uniformity as can the overall life of the engine. In this respect, it is important to understand what factors within the distortion of the inlet flow have the largest impact on the engine performance.

1.2.3. Factors Affecting Engine Performance

There are several main contributors to inlet distortion for an engine. Total pressure distortion is perhaps the most well-studied and well-documented form of inlet distortion. Other forms of inlet distortion that have been studied include total temperature distortion, planar waves and inlet flow angularity or swirl (ARD50015, 1991; ARD50026, 1995; Inlet Flow Angularity, 2000). Total pressure distortion will be used throughout the current research as a measure of inlet distortion due to the well

established methodologies (ARP 1420, 1998; AIR 1419, 1999) for describing total pressure distortion and predicting the effect of total pressure distortion on a fan or compression stage. Total pressure distortion is directly generated by the serpentine shape of the inlet duct in addition to the flow disturbances generated by the presence of a diffusing inlet duct or one with transitioning cross-sectional shape. The Society of Automotive Engineers has a sub-committee (S-16) whose task is to describe inlet distortion issues and quantify the different forms of inlet distortion into standardized methodology. Several documents have evolved from their efforts including SAE Aerospace Recommended Practice 1420 and its more descriptive counterpart Aerospace Information Report 1419. The methodology outlined in these documents has been used throughout this research in order to describe the distortion generated by a serpentine inlet duct and to quantify changes in inlet flow distortion at the AIP. These distortion descriptors are defined in detail in the following chapters.

Inlet swirl is known to effect engine performance and the S-16 committee is working on recommended practices regarding inlet swirl (SAE Committee S-16, 2000). Swirl in the same direction as engine rotation, or co-swirl, actually enhances engine performance stability by turning the flow in the same direction as the blades. Following this same thought, swirl rotating in a direction countering engine rotation forces the engine to do more work and results in a negative impact on the fan or compression system stability. Inlet guide vanes could be used to reduce the affect of inlet duct swirl (counter-swirl) or to enhance the affect of inlet duct swirl (co-swirl).

Swirl is produced in the natural flow through a serpentine duct and will be discussed in more detail in Chapter 2. In general, the flow forms a pair of counter-

rotating vortices when the turn in the S-duct is significant enough to cause flow separation. However, this swirl is generally not strong enough to negatively impact the compression system performance. Guo and Seddon (1982) performed a study on the swirl in S-ducts and concluded that at low incidence the secondary flow in serpentine ducts does not negatively impact engine operation. However, with increased incidence angle the swirl can affect the operability range of the engine. This will depend on the nature of the aircraft and the location of flow separation due to high incidence angle.

Beale (2001) describes the future of inlet distortion testing from the engine performance point of view. He outlines the growing importance of distortion factors such as inlet swirl and time-variant total temperature and total pressure variations. His work outlines the development of distortion generators which will reproduce these effects caused by stealthy inlets. However, this work is still in a developmental stage.

Ultimately, several forms of inlet distortion can impact the performance of the gas turbine engine. However, many of these factors are still being studied to establish a universal methodology to describe their effect on the gas turbine engine. Total pressure distortion has been studied in detail over the last several decades, resulting in established methodologies for describing the flow quality at the AIP. In addition to this description of the flow field, engine modeling codes can be used to further determine the effect of inlet distortion on engine performance. Based on the established methodologies, there are several models available to evaluate total pressure distortion impact on engine performance. There are also computer codes which examine other inlet distortion factors in various manners.

1.2.4. Compression System Modeling

Inlet distortion typically affects the compression system of a gas turbine engine. Both the stability limits and the life of the engine can be affected by inlet distortion. A compression system model can be utilized to predict the effect of inlet distortion on the stability limit of a compression system. A typical compressor map displays total pressure ratio versus corrected mass flow as shown in Figure 1.4. The stability limit is marked by the dotted line. At this point the compression system operation is no longer stable due to the reduced mass flow through the system at the same corrected rotor speed. The reduced mass flow increases the incidence angle of the incoming flow on the blade. The increased incidence angle will induce positive incidence flow separation over the blade. This separation will reduce the amount of turning of the flow, affecting the following stage. Under certain conditions, and if the flow is reduced far enough, global flow reversal may occur. This is also known as surge.

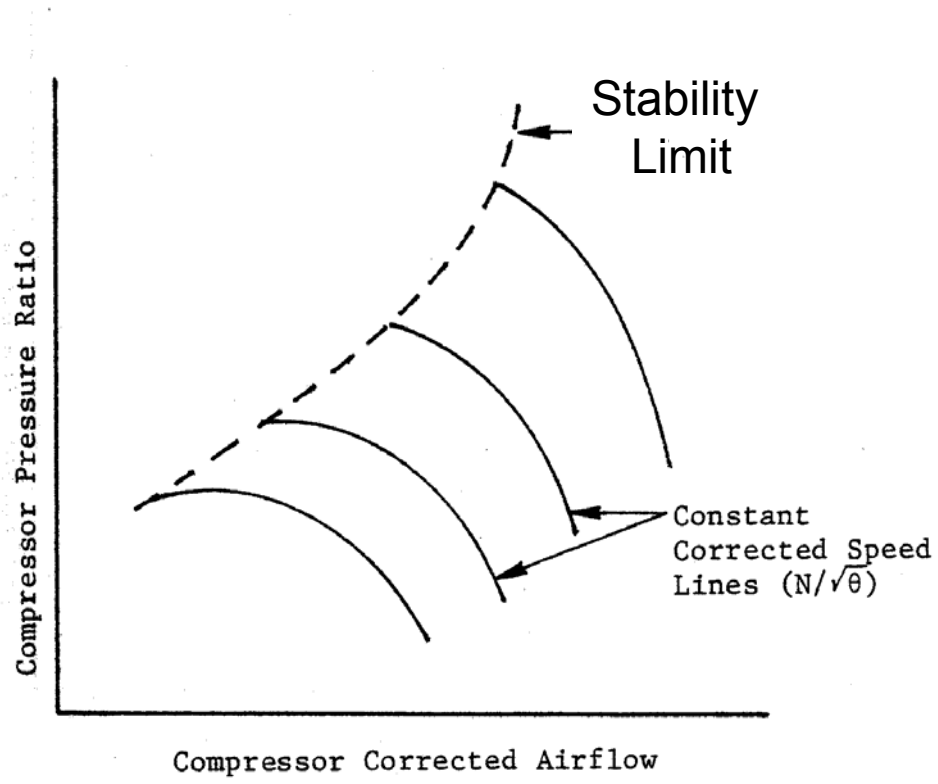

Figure 1.4 Typical Compressor Map (modified from Campbell, 1981)

The surge or stability margin can be defined in several different ways but always serves as a measure of the region of stable operation between the operating point and the stability limit. The stability margin can be defined in terms of constant corrected airflow or in terms of constant corrected speed, as shown in Figure 1.5. In this work, the constant corrected speed definition will be used to describe the stability margin and change in pressure ratio. The stability margin definition used throughout this work is:

$$SM = \frac{PR_{SL} - PR_{OP}}{PR_{OP}} * 100$$

where PR_{SL} is the pressure ratio at the stability limit and PR_{OP} is the pressure ratio at the operating point.

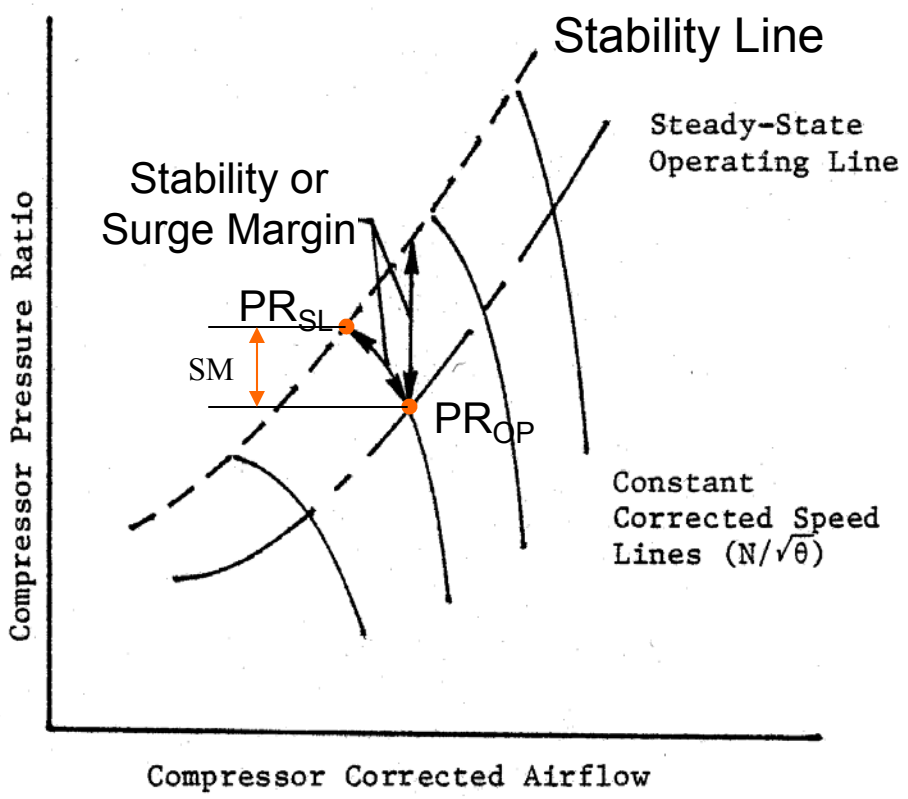

Figure 1.5 Stability Margin Definition (modified from Campbell, 1981)

The stability margin of a compressor can be reduced from either end. The stability limit can be reduced, or the operating point could move higher on the speed line. There are several factors which will affect the stability margin of a compressor. For example, the operating point will move up due to engine transients (acceleration/deceleration), engine tolerances, bleed effects, afterburner transients, and steady state inlet total pressure and temperature distortion. The stability limit will be reduced from deterioration, manufacturing tolerances, variable stator rigging and more. Figure 1.6 and Table 4.1 show some of the factors affecting the stability margin of a compression system. The steady state total pressure distortion has been found to affect

both the operating line (increase) and the stability line (decrease), reducing the overall stability margin for the compression system.

Table 4.1.1 Factors Affecting Compressor Stability Margin (taken from AIR 1419, 1983)

FACTOR	OPERATING LINE	SURGE LINE
INLET DISTORTION		
A. STEADY-STATE TOTAL-PRESSURE DISTORTION	X	X
B. TEMPERATURE DISTORTION	X	X
C. SWIRL DISTORTION	X	X
D. MAX. INSTANTANEOUS TOTAL-PRESSURE DISTORTION		X
RAM RECOVERY	X	
HORSEPOWER EXTRACTION	X	
PLA TRANSIENT	X	
ENGINE DETERIORATION	X	X
FUEL CONTROL DETERIORATION	X	
DETERIORATION EFFECT ON TRANSIENT FUEL FLOW RATE	X	
FUEL CONTROL TOLERANCES	X	
VARIABLE GEOMETRY CONTROL TOLERANCES	X	X
ENGINE-TO-ENGINE VARIATION	X	X
ENGINE VARIATION EFFECT ON TRANSIENT FUEL FLOW RATE	X	
COMPRESSOR BLEED	X	X
REYNOLDS NUMBER EFFECTS	X	X
NOZZLE MATCHING EFFECTS	X	
HUMIDITY	X	X
CONTROL MODE	X	
BACK PRESSURE DISTORTION	X	X
COMRESSOR INTERACTION EFFECTS	X	X
TRANSIENT VARIABLE GEOMETRY EFFECTS	X	X
PLA TRANSIENT HEAT TRANSFER	X	X

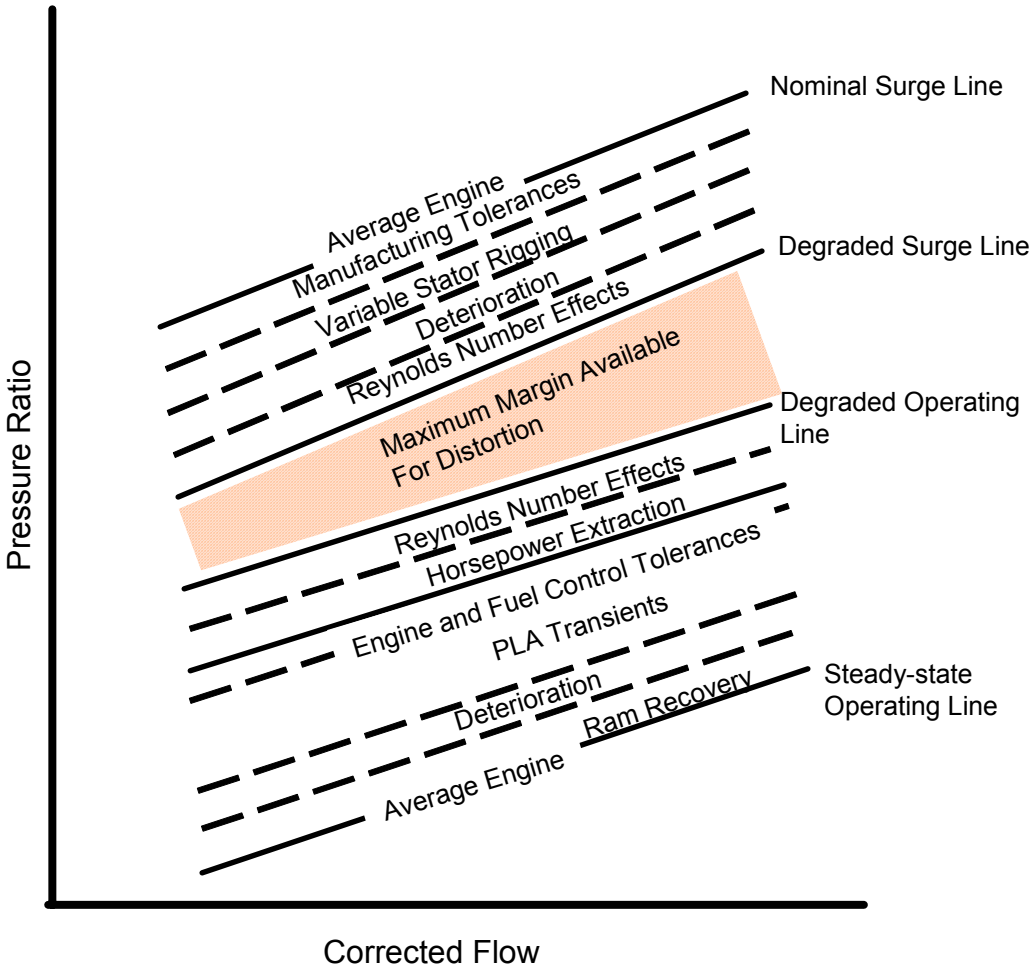

Figure 1.6 Factors Affecting Compressor Stability Margin (taken from AIR 1419, 1983)

Figure 1.7 shows a schematic of the change in operating point for distorted flow compared to undistorted flow. The distorted flow operating point for the same corrected rotor speed is seen to move off the undistorted flow speed line. AIR 1419 (1983) shows experimental results from engine testing which reveal that some forms of total pressure distortion force the constant speed line to a lower position on the compressor map. This effect can be seen in Figure 1.8.

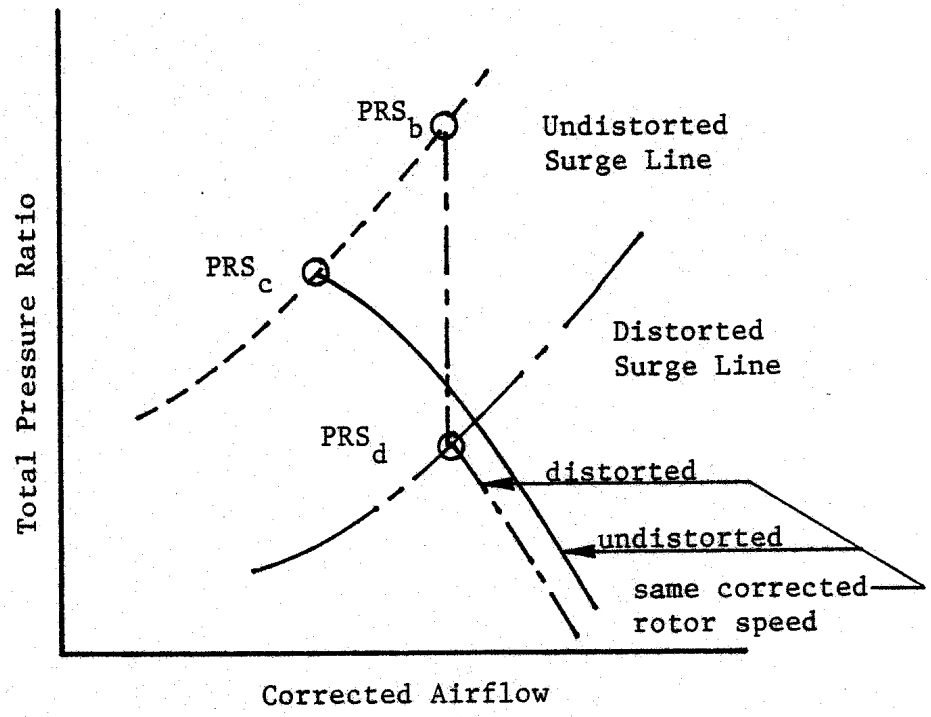

Figure 1.7 Undistorted and Distorted Speed Line Representation (taken from Campbell, 1981)

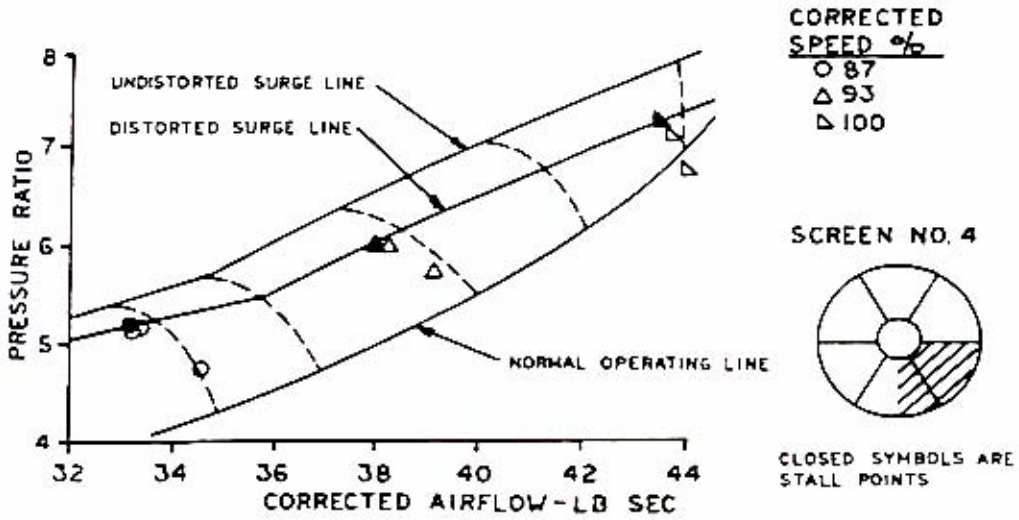

Figure 1.8 Experimental Display of Distorted Speed Line for Circumferential Distortion (taken from AIR 1419, 1983)

It is important to develop a computational capability to determine not only the distortion generated by complex serpentine inlet ducts but also the influence this distortion has on the stability of the gas turbine engine receiving the inlet flow. Given the total pressure distortion, the effect on a compression system can be predicted. The total pressure distortion should reduce the stability limit for a compression system while increasing the operating point. In addition, the constant speed line may shift inward on the compressor map for distorted flow as compared to undistorted flow. A compression system model could be used to predict the improvement in compression stability margin for design and off-design conditions with the addition of flow control. To this end, compression system models exist of varying complexity. The most basic model involves simple cycle analysis while the most complex models are fully viscous three-dimensional models, with varying levels of complexity between these extremes. Three-dimensional models exist which are simpler and less costly to run than the full Navier Stokes solutions. These models include approximations such as steady, adiabatic, and inviscid flow. Component modeling is also available through this range of model complexity. The advantage of component modeling is that the engine component thought to be most effected can be isolated and evaluated in relevant detail.

Davis et al (2002) have suggested a new test program focus which utilizes advancements in predictive models for both inlet duct and engine component performance. The use of these models can reduce the required test matrix for both inlets and engines as well as compatibility for the airframe/propulsion system. In this study, arguments were made for the design of experiments methodology which reduces the test matrix while ensuring that all parameters thought to be important are tested in some

fashion. This paper also discusses the current practices involved for both inlet and engine testing with the bulk of the testing included in wind tunnel tests (inlets) and direct connect tests (engines). The minimal coupling between the inlet and engine testing is highlighted as a technical challenge in airframe propulsion integration. With the advent of stealthier inlet ducts (S-ducts) the flow at the AIP is becoming more complicated.

This study by Davis et al (2002) also highlights the current computational codes available for decreasing the test matrices required for airframe propulsion integration. Computational fluid dynamic codes are still in their infancy and are not yet capable of describing the complicated flow through a complete engine in a reasonable time. However, component level CFD codes are available for detailing the flow through complicated inlet ducts. There are still inaccuracies to be resolved particularly regarding the turbulence modeling in the code. Turbulence models are not yet available with great accuracy in capturing the flow physics involved in turbulence dissipation. Some computational codes have been developed with simplifications that allow prediction of the compression system response to inlet distortions. One of these codes is TEACC (Turbine Engine Analysis Compressor Code). TEACC can describe the flow through blade rows in a compression system by using the Euler equations and representing the turbomachinery source terms through a streamline curvature approach. This streamline curvature approach uses semi-actuator disk theory to calculate source terms which simulate the effects of the blades. The conservation of mass, momentum and energy equations including the source terms are solved three-dimensionally in this way allowing complicated flow patterns to be followed through the stages of a compression system.

Hah et al (1996) have developed a full annulus CFD code using the Reynolds averaged Navier Stokes equations and a k-ε turbulence model. They have calculated the effect of full annulus three-dimensional distortions on the stalling behavior of a compressor using this code. This code uses full annulus solutions rather than actuator disc theory and can therefore provide more detailed solutions, with a corresponding increase in computational time.

One-dimensional codes also exist to examine the impact of inlet distortion on compression system stability most of which employ parallel compressor theory. Parallel compressor theory models the compressor by circumferentially dividing it into several equal area segments (up to 6). Each division is treated as a separate compressor with individual inlet boundary conditions and a common exit boundary condition. The compressor model is said to stall when one of the parallel compressors reaches the stability limit of the original compressor. The stall point is then calculated by averaging the operating point for the segments at this point where one of the segments has stalled. In this way circumferential distortion can be modeled as the inlet boundary condition. In more recent years, several variations of the original model have been added to improve the predictive capability of the simple model.

Mazzawy (1977) looked at parallel compressor models for the application of inlet distortion. In Mazzawy's model the parallel compressor model is modified by accounting for deviations from undistorted compressor performance. The model can handle total temperature or total pressure variations as inlet boundary conditions and can also account for circumferential variations in exit static pressure. The model can be run for each blade row, in which case undistorted performance characteristics for each blade

row are needed for input. Alternatively, the model can be executed for overall compressor performance, which requires overall undistorted compressor performance characteristics.

A DYNamic Turbine Engine Compressor Code (DYNTECC) was originally developed by Davis (1986). Recent modifications to the code have expanded the parallel compressor portion of the code based on research by Kimzey to include circumferential mass redistribution, radial mass redistribution, dynamic blade response, and radial work redistribution (Shahrokhi, 1995). In this way the individual parallel compressors are no longer isolated from one another and cross-flow between adjacent segments based on static pressure differences is accounted for. In this code, incompressible flow is assumed allowing the use of Bernoulli's equation in addition to conservation of mass.

Several engine and compression system modeling codes have been reviewed, illustrating the current state-of-the-art of predictive capabilities of varying complexity for the study of engine response to inlet distortion. Each model includes different assumptions creating different capabilities, with the biggest tradeoff being accuracy of the results at the expense of increased computational effort. Based on the available modeling codes, DYNTECC was chosen in this research to predict the effect of the inlet distortion measured experimentally on a representative compression system. The inlet duct tested is still in the early design stages and therefore a more complex code is not warranted due to the increased computational costs.

1.3. Summary

Serpentine ducts have been studied in the past for aircraft inlet duct applications. Various design qualities have been examined to determine the effect on the flow

uniformity at the exit of the duct including centerline curvature, transitioning cross section and diffusing cross section. These factors contribute to inlet distortion that is ingested by the gas turbine engine following the inlet duct. In order to improve the flow uniformity at the aerodynamic interface plane, several flow control techniques have been demonstrated. The flow non-uniformity at the AIP affects the gas turbine engine, primarily the compression system, in a variety of ways. The most established form of inlet distortion is total pressure distortion which decreases the operability range of an engine and reduces the overall life of the engine. The effect of total pressure distortion on a gas turbine engine compression system can be further studied through the use of a compression system model.

In this research, a technique has been developed to examine off-design flight conditions during the static ground test phase. The flight conditions were determined through CFD predictions provided by Lockheed Martin. Data were collected at the aerodynamic interface plane in order to quantitatively define the flow exiting the inlet duct. For inlet testing, the AIP is defined as the exit of the inlet duct which, in a direct connect test, would be coincident with a plane one diameter upstream of the engine fan face. These AIP data were then used to predict the effect of the experimental total pressure inlet distortion on a compression system through the use of a parallel compressor modeling code, DYNTECC. This work has allowed early awareness of potential design challenges due to the aggressive nature of the serpentine inlet duct tested.

2.0 Flow Development

Several factors have been addressed which affect the flow development within serpentine or S-duct inlets. The centerline curvature is known to influence flow separation. The area ratio and transitioning cross-sections can also contribute to the inception of flow separation. These design factors tend to be driven by aircraft configuration requirements including improved thrust to weight ratio and low observable criteria. The combination of these design characteristics will determine how the flow develops and whether or not the flow separates. From the propulsion point of view, the flow properties at the exit of the duct are of most concern since this is the flow that will enter the turbine engine. The flow development is important as a means to understanding how the exit profiles develop and how they may be corrected.

At the risk of being repetitive, this chapter will re-visit some of the references presented in Chapter 1, concentrating on the findings regarding flow development pertinent to this research. Computational fluid dynamics results from Lockheed Martin will also be presented to describe the expected behavior of the flow development through the specific duct tested throughout this research.

2.1. Background

As shown in the previous section, much information regarding the flow trends within S-duct inlets can be found in the literature. In general, a serpentine inlet duct involves two turns in addition to a height offset. Much of the information in the literature involves simple cross-sectional geometries with emphasis on circular S-ducts. A numerical study on flow in a turning duct is found in a report by Kramer and Stanitz

(1952) where they examined a 90 degree elbow. Their work showed that the inside wall of a turn will experience higher velocities but a lower static pressure coefficient while the outside wall of a turn encounters lower velocities and a higher static pressure coefficient. Schlichting (1955) describes the formation of vortices within a curved pipe based on the radial variation of centripetal force. The flow in the center of the duct has a higher velocity and will be subjected to a larger centripetal force than the flow near the wall at the inside of the turn which has a lower velocity. The low velocity near the wall is due to the no slip condition where the fluid velocity goes to zero at a stationary wall. This variation in centripetal force leads to secondary flow which circulates from the center region towards the wall and from the wall into the center region.

Extensive experimental work has been done on circular cross-section S-ducts involving benchmark quality measurements describing the detailed flow within an S-duct (Vakili et al., 1984; Vakili et al., 1985; Wellborn et al., 1992). These studies used geometrically similar 30^{o}-30^{o} S-ducts. Streamwise wall static pressure measurements and oil flow visualization provided information concerning flow development and details about flow separation. The oil flow visualization in each case indicated flow separation downstream of the first turn. This flow separation is believed to be due to the low momentum, large boundary layer fluid from the first turn in combination with a large increase in cross-sectional area (high diffusion rate). The study by Vakili et al (1984) indicated that the separated flow never reattached in the baseline case; whereas Wellborn et al found that the flow separated in a similar region but reattached further down the duct. In both cases (Vakili et al., 1984 and Wellborn et al., 1992) the flow separation shown in the oil flow visualization was also illustrated in the streamwise wall static

pressure measurements. The static pressure profiles were constant in the separated region indicating no change in static pressure. Since both studies were conducted on diffusing S-ducts, the static pressure should be constantly changing throughout the duct. In this way, constant values of wall static pressure along a diffusing duct were shown to indicate flow separation.

Bansod and Bradshaw (1972) describe the general behavior of flow in an S-duct. They found that the regions of low total pressure are associated with a pair of longitudinal vortices. The pressure gradients from the duct turning produce a larger deflection in the boundary layer fluid than in the core flow, inducing vortices in the flow. Rowe (1970) found a similar result with the wall fluid and central core flow interchanging through the duct turns.

Towne (1984) examined the flow within 180 degree bends and described the flow as "the classical flow pattern for flow in a curved pipe. The low energy flow near the wall migrates circumferentially away from the outside, or pressure side, of the bend and toward the inside, or suction side. The higher speed flow in the core region moves toward the outside of the bend due to centripetal effects. A pair of counter-rotating vortices is thus established." This study has also shown that for turbulent flow (as compared to laminar flow) the vortices tend to be closer to the wall and more concentrated.

In a study by Reichert and Wendt (1993), constant values of static pressure in the streamwise direction were shown to indicate flow separation. In addition to detailed streamwise wall static pressure measurements, their study included oil flow visualization. The results from the flow visualization agreed with the wall static pressure measurements

in terms of regions of separated flow. These results are comparable to those of Wellborn et al and Vakili et al.

Reichert and Wendt (1994) reported on the nature of the secondary flow within a diffusing S-duct inlet. The increase in area of the duct cross section in the streamwise direction results in an adverse pressure gradient. In their study this pressure gradient led to flow separation. In addition, the centerline curvature of the duct creates cross-stream pressure gradients which initiate fluid movement in the form of counter-rotating vortices. This process results in counter-rotating vortices which, uncontrolled, continue to gain momentum, axially transferring more energy into the secondary flow.

These studies show one set of counter-rotating vortices from the first turn of the S-duct while the second turn does not always produce additional vortices. The formation of vortices is dependent on the radius of curvature of the turns, the angle of the turns, the rate and degree of change in cross-sectional area, and the change in cross sectional shape.

In the STRICT inlet duct, shown Figure 2.1, there are actually three turns. If the inlet is split within the second turn, as shown in Figure 2.1, the duct can be divided into four turns or two S-ducts connected at the second turn. In viewing the duct in this way, two sets of counter-rotating vortices should be expected, one from each S-duct. The vortices from the "first" duct should dissipate somewhat through the length of the duct since they are created at the start of the duct. The "second" duct is shorter, and the vortices formed there would be expected to dominate the flow distortion at the AIP.

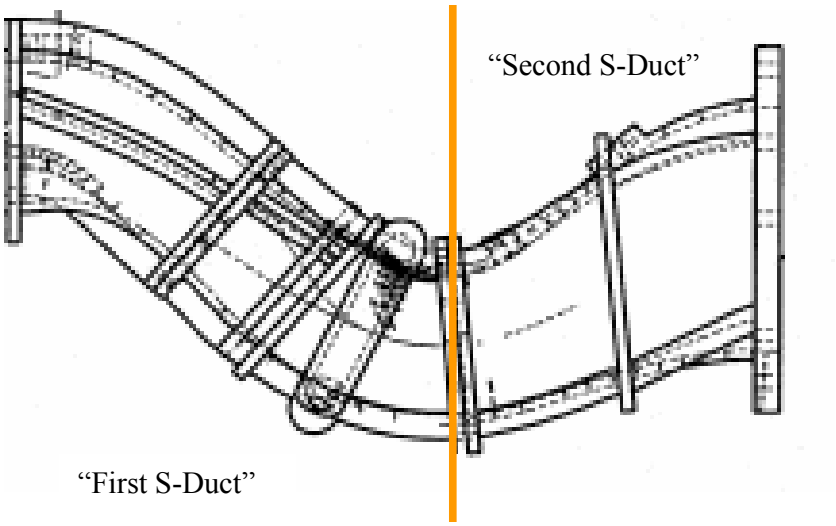

Figure 2.1 STRICT Inlet Duct Drawing (Courtesy of Lockheed Martin)

2.2. Computational Fluid Dynamic Results

Computational fluid dynamics (CFD) modeling is used to deduce the flow behavior within the inlet duct. Lockheed Martin provided the CFD results presented throughout this research using a solver known as Falcon. Falcon is a Reynolds-averaged Navier-Stokes code with an advanced vorticity model which allows numerical calculation of the effect of vortex generators as an additional source rather than including the vortex generators in the duct geometry.

Figure 2.2 shows the CFD generated total pressure ratios for the cruise condition case without flow control. The total pressure ratios are given at six different cross sections along the inlet duct. The total pressure ratio scale can be seen in Figure 2.2 where red is severe total pressure loss while blue represents good total pressure recovery. The first cross section is the initial cross section of the duct at the end of the constant area section, or the beginning of the first turn. The final cross section represents the exit of the inlet duct, or the aerodynamic interface plane (AIP). In Figure 2.2, frames two and

three show the formation of the counter-rotating vortices at the bottom corners of the duct cross-section. In frames 4-6 these vortices are still present, but they are beginning to lose their strength as evidenced by the color of the region of pressure loss. The vortices could die out completely if the duct were longer; but in the interest of a compact aircraft with improved thrust to weight ratio, the length of the duct is severely limited.

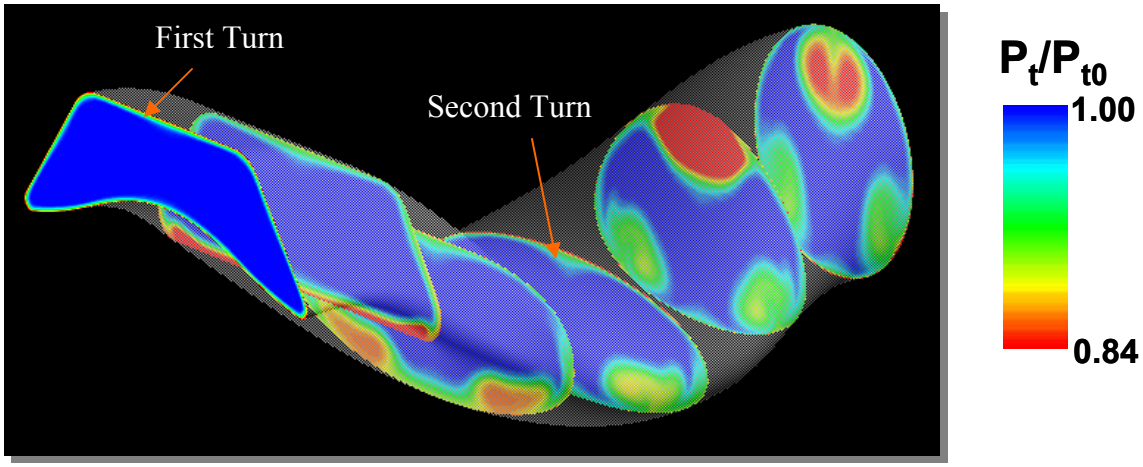

Figure 2.2 Vortex Formation CFD Results for Cruise Condition without Flow Control (Courtesy of Lockheed Martin)

The second turn occurs at the fourth frame in Figure 2.2. Two counter-rotating vortices are created along the top of the duct, or the inside of the turn. Due to the geometry of the duct cross section at this plane, which enters the second turn as an oval transitioning to a circular cross section, the separation is forming in the middle of the top wall of the duct. The fifth frame in Figure 2.2 clearly shows the intense region of separation from the second turn vortices, but the sixth frame shows the two separate vortices. Since the distance between the second turn and the aerodynamic interface plane is much shorter than the distance from the first turn to the AIP, the vortices from the second turn are much stronger at the AIP. In fact, the second turn vortices dominate the

total pressure loss at the AIP. For this reason, these are the vortices that are targeted by the flow control technique.

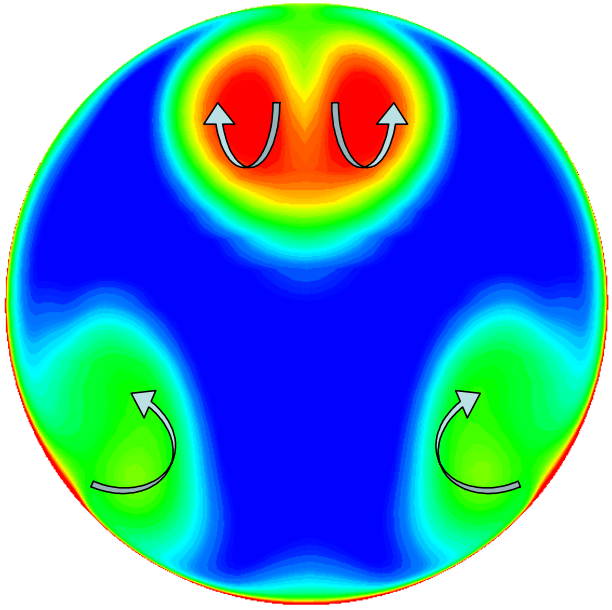

Figure 2.3 CFD Total Pressure Contour for Cruise Condition without Flow Control with Direction of Flow Vortices at AIP (Courtesy of Lockheed Martin)

The total pressure contour from a CFD prediction of the flow field at the AIP for cruise condition without flow control is shown in Figure 2.3. This shows clearly the two sets of counter-rotating vortices. Figure 2.3 also shows the direction of the flow vortices. It is possible that these two sets of vortices could become large enough to interact with each other. The upper vortices are rotating down into the core region of flow and then turning away from each other and back into the wall through the low pressure region at the top center of the duct. The side vortices that originated at the first turn of the duct are rotating up into the core flow region of the duct and then turning away from each other and back into the side wall through the low total pressure region remaining from the change in pressure gradient in the first turn of the duct. When these vortices grow large enough to interact with each other, there is some cancellation in the vortices. The two

vortices on the left side of the duct no longer act independently of one another and start to cancel some of the overall effect. The same holds true for the right side.

Figure 2.4 shows the formation of the vortices at the first turn in more detail. In the vortex development, the red streamlines initiate along the sides of the duct while the blue streamlines initiate along the bottom of the duct. These vortices are formed by the first turn in combination with the cross sectional geometry of the duct at this point. The turning of the duct produces the flow separation while the cross sectional geometry of the duct at that plane dictates the location along the inside wall of the turn where the flow will separate. In the case of the first turn, the geometry of the duct has distinct corners which are more likely to separate, even without turning, due to the growth of the boundary layers along the walls in the corner region as compared to growth in the core flow region.

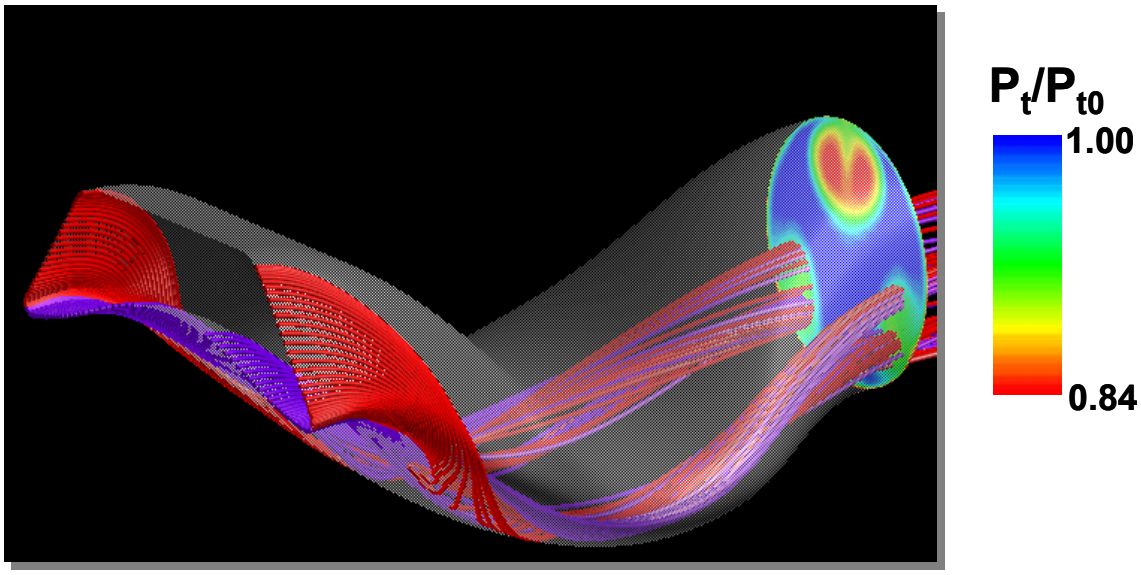

Figure 2.4 CFD of Corner Vortex Streamlines (Courtesy of Lockheed Martin)

2.3. Summary

Through a review of the available literature and examination of the streamwise CFD solutions, the flow profile at the AIP has been predicted. Two sets of counter-rotating vortices are expected to be produced within the serpentine duct, one set at each of the first two turns. These counter-rotating vortices will yield total pressure losses at the AIP of varying strength, dependent on the diffusion of the vortices prior to the AIP. The total pressure losses will appear at different positions at the AIP due to the cross-sectional shape of the duct at the time of inception. For instance, the cross-sectional geometry at the first turn of the duct yields flow separation in the corner regions. The total pressure losses at the AIP were studied experimentally to determine how they varied from the predictions.

3.0 Experimental Setup

Inlet ducts are typically tested in a static ground test facility as a preliminary design step to determine the distortion produced within the duct. This information is vital for engine development which often occurs parallel to inlet development. Static ground test facilities simulate pre-takeoff conditions and can also be modified to represent a cruise condition. In a cruise condition, the aircraft is moving through stagnant air creating a constant angle of flight relative to the incoming flow direction. Depending on the placement of the inlet duct and the surrounding body of the aircraft, the flow coming into the inlet duct may involve thick boundary layers and even secondary flow vortices from an upstream portion of the aircraft.

This project involved the development of a static ground test facility to simulate the flow behavior in an inlet duct at different flight conditions. The flight conditions examined were a baseline or cruise flight, angle of attack, and asymmetric distortion. The exit flow field is of primary importance for its impact on the gas turbine engine following the inlet duct. The compression system of the gas turbine engine is most affected by flow non-uniformity at the aerodynamic interface plane (AIP). This flow non-uniformity, or inlet distortion, can reduce the stability margin of the compression system. Reduction in stability margin can limit the aircraft maneuverability and the ability to carry out flight missions. The flow field is defined in terms of total pressure distribution at the AIP. Standardized distortion descriptors are used to describe the flow and determine how the flow distribution may affect the compression system following the inlet.

The required flow rate for this experiment was 16.5 lbm/s through the inlet in order to achieve a throat Mach number of 0.55. The Reynolds number based on the inlet throat hydraulic diameter was $1.76*10^5$ where the hydraulic diameter is defined as D_h=4*Area/Perimeter. Flow control was added in the form of mass injection to improve the flow qualities at the AIP. The combined flow rate through mass injection was limited to 1% of the inlet mass flow rate or 1.65 lbm/sec. This maximum mass flow rate was based on restrictions for available bleed air from typical gas turbine engines that might be used in unmanned aerial vehicles. In the aircraft configuration for this inlet duct application, there will be several areas requiring bleed so that the amount of bleed available is limited. The experimental facility is described in the following sections as well as the method for creating simulated flight conditions. A predicted flight condition, angle of attack, was simulated in order to evaluate the inlet duct and the flow control system at a realistic off-design condition. An asymmetric distortion similar to sideslip was also evaluated to determine the flow control response to asymmetric conditions. The experimental measurements are also described in this chapter as well as the flow control technique and sources of uncertainty.

3.1. Experimental Facility

A facility was developed in order to test inlet ducts in a static test environment. Figure 3.1 shows a schematic of the facility where the airflow is from left to right. The forward plenum chamber and bellmouth are present to bring the flow into the inlet duct uniformly. The flow must enter the inlet duct in a uniform manner to enable the appropriate simulation of flight conditions. Possible sources of non-uniformity include ground vortex ingestion, temperature non-uniformity, flow angularity, or turbulence from

the ambient air. In this setup there was not a problem with non-uniform air at the entrance due to the low speeds of the flow at the entrance of the front plenum chamber, the length of the plenum chamber, and the shape of the bellmouth. The uniformity of the airflow was confirmed through throat total pressure measurements. The airflow traveled through the bellmouth into the diffusing serpentine inlet duct. The diffusion takes place through a complex change in cross sectional area and shape. The inlet duct exit is a circular cross section with a ten inch diameter. The measurement duct has a constant circular cross section also with a ten inch diameter to match the exit area of the inlet duct. The measurement duct housed the pressure probes and provided an anchor for the traversing units. The measurement setup is discussed in more detail in following sections. The measurement duct exits into the aft plenum chamber. The aft plenum chamber is present to allow the flow to expand from the ten inch diameter jet leaving the measurement duct to supply the 20 inch diameter engine. Ideally, the engine should be uniformly loaded in order to decrease the stress on the engine during testing. The gas turbine engine is being used as a fluid driver. In aircraft applications the engine fan face would be coincident with the AIP and would cause interaction with the inlet duct distortion. However, experimental comparisons have shown total pressure and distortion results to be nearly identical between inlet/engine ground tests and inlet only ground tests (AIR 1419, 1983).

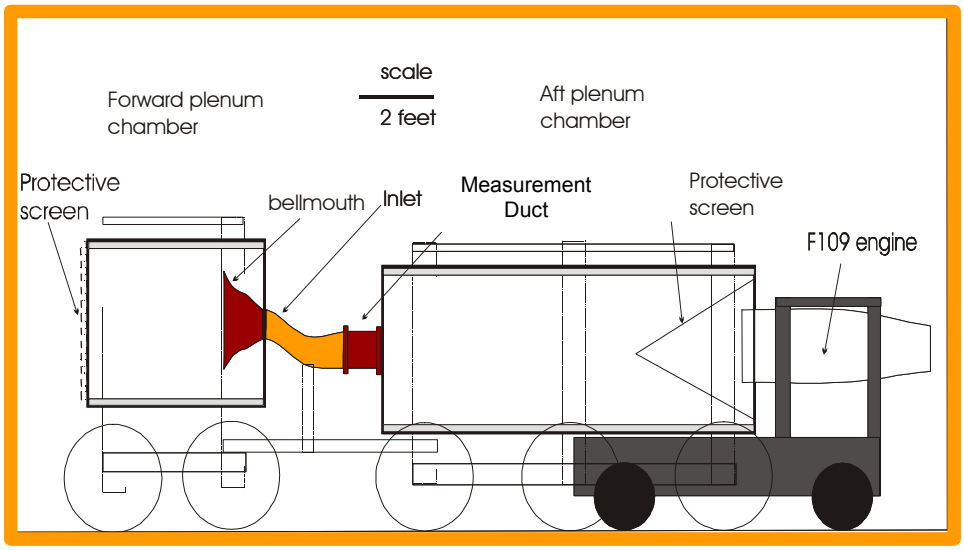

Figure 3.1 Schematic of Inlet Test Facility

Figure 3.2 Front Plenum Chamber

Looking at the setup in more detail, Figure 3.2 shows a photograph of the front of the test setup. Here the front plenum chamber can be seen clearly. The tires on the front plenum chamber were used in order to assemble the facility, but during testing both plenum chambers were supported by jack stands so that the tires were not in contact with the ground. The protective screen on the front of the plenum chamber is a two inch

square screen and is designed to prevent foreign objects from being ingested into the system. This plenum chamber is a ½ inch steel pipe, four feet in diameter. The forward plenum chamber is five feet long to allow for the incoming flow to straighten out before entering the setup. The velocity of the flow in the front plenum chamber is ~17 ft/sec. Based on this velocity, additional flow straightening screens were determined not to be necessary.

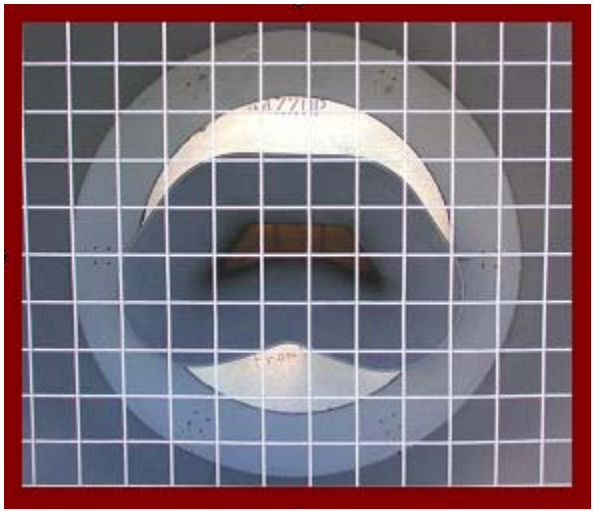

Figure 3.3 Front Plenum Chamber with FOD (Foreign Object Debris) Screen and Bellmouth (View is looking downstream into the inlet)

Figure 3.3 is a closer view of the front plenum chamber showing the bellmouth for the inlet duct that was used to bring the airflow in isentropically. From Figure 3.3 it can be seen that the bellmouth is attached to an aluminum plate at the rear of the front plenum chamber. Having the aluminum plate as the interface of the plenum chamber and the inlet duct allowed for a more versatile setup with the ability to switch ducts and adjust the height of the bellmouth to match the height offset of the inlet duct being tested. Figure 3.3 also shows the view from the front of the inlet duct where the bulk of the inlet duct is not visible. Only the top of the first turn is visible in this view of the inlet duct.

This shows how serpentine inlets can reduce the radar return signature by eliminating a direct line of sight to the engine fan face.

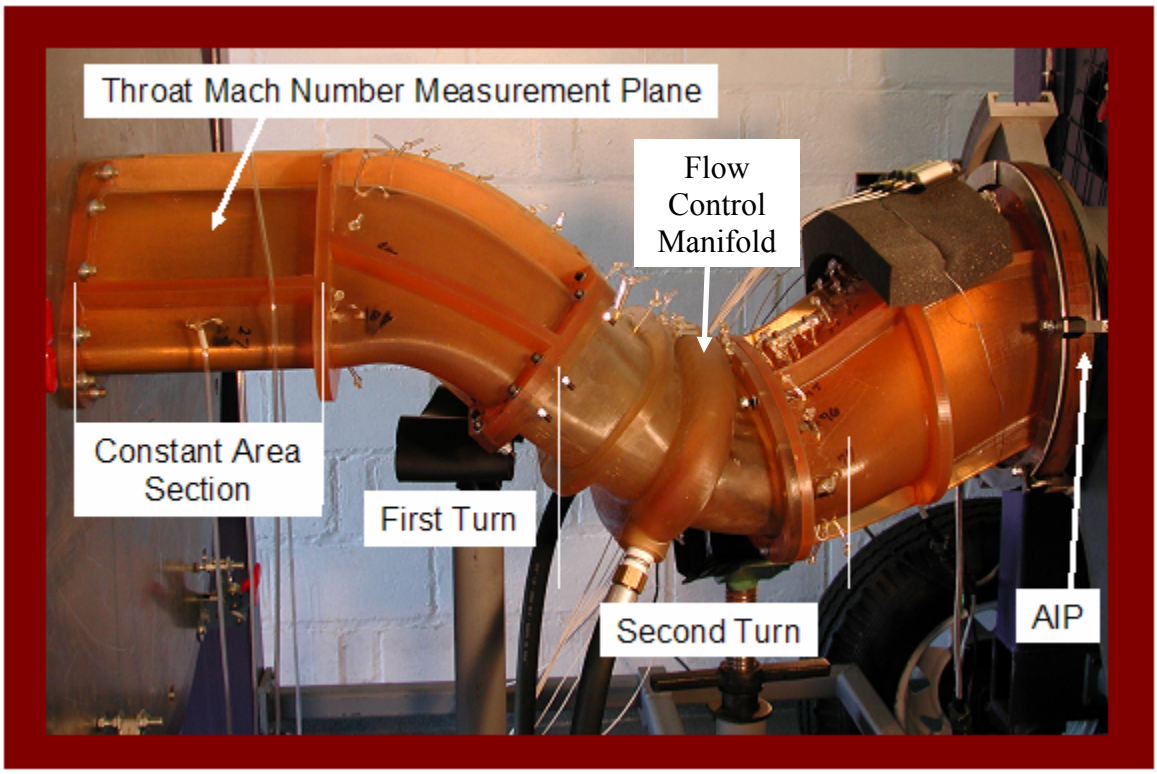

Figure 3.4 Experimental Inlet Duct

The experimental portion of this research concentrated on the flow behavior in a specific inlet duct developed by Lockheed Martin. This inlet duct is named the STRICT inlet duct based on the Air Force program for which it was designed (Structurally Integrated Compact Inlet Technology program). The program requirements included length to diameter ratio limitations, entrance geometry integration with the aircraft body, and height offsets to hide the engine fan face and adhere to space restraints. Figure 3.4 shows a side view of this inlet duct with airflow from left to right. From this view the aluminum plate can be seen on the far left side of the picture. The bellmouth lies on the opposite side of the plate. The first section of the duct is level for about ten inches. This

is known as the constant area section. The purpose of this section will be discussed later in terms of simulating flight conditions. It is in this constant area section that the throat Mach number is measured as seen in Figure 3.4. There are four static pressure ports around the circumference of the duct at a single plane within the constant area section. These pressure measurements are averaged to obtain an average static pressure at that plane. In addition, isentropic flow is assumed to this point, so the ambient total pressure is used for the total pressure at that point. From here the throat Mach number is calculated as $M = \sqrt{\left[\left(\frac{P_0}{P}\right)^{\frac{\gamma-1}{\gamma}} - 1\right]\left(\frac{2}{\gamma-1}\right)}$ to determine the flow in the duct. All of the tests in this study were run with a throat Mach number of 0.55 based on the facility capability for sustained run time.

At the end of the constant area section, the actual inlet duct begins. The length to diameter ratio of this inlet is three. The inlet duct can be seen in Figure 3.4. This first bend in the duct occurs immediately. Following the first turn, the duct is angled downward at ~35 degrees. At the completion of the first turn, the duct enters the second turn and turns upward at ~25 degrees. Following the second turn, the duct turns the flow back in the axial direction, with a final height offset of five inches. During all the turning, the duct cross-sectional geometry is also changing. This allows more sources for the development of flow distortion in the form of separating flow vortices. The flow physics will be discussed in more detail in the following chapter. Figure 3.4 is also useful in illustrating the height offset between the entrance and the exit of the duct.

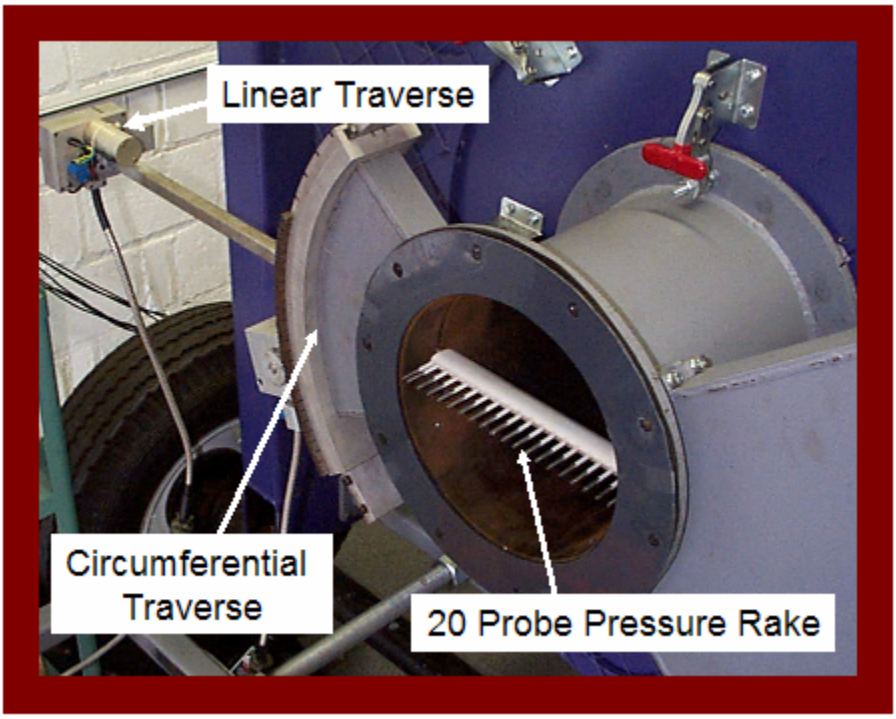

Figure 3.5 20 Head Total Pressure Probe Rake

Following the inlet duct is the measurement duct which houses the total pressure measurement probes. The measurement duct is one foot long to allow space for the instrumentation housed within and around it as seen in Figure 3.5. Both a circumferential and a radial traversing unit were used to move the probe throughout the exit area and acquire detailed flow field measurements. These traversing units can also be seen in Figure 3.5. The total pressure rake is held on one wall by the traversing units while the wall contains a slot for the opposite end of the rake. This slot allows the rake to be held at both ends, reducing the stress on the tubing. The pressure probe heads actually extend into the AIP or the exit plane of the inlet duct. The pressure probe rake consisted of 20 total pressure Kiel probes. Kiel probe heads reduce the effect of flow angularity on the total pressure measurements. They allow for the total pressure to be obtained for flow

within ±12 degrees of the Kiel-head axis. The rake itself was designed to withstand a flow that was 0.5 Mach, where the expected Mach number at the AIP is ~0.15, since any breach of material strength would result in foreign objects striking the engine. There were some precautions against such a situation, but the goal was to avoid any possibility of debris from the test setup. While the probe rake is sturdy in nature, it obstructs less than six percent of the flow area. The body of the rake was also designed as an airfoil so that it would minimally disrupt the flow.

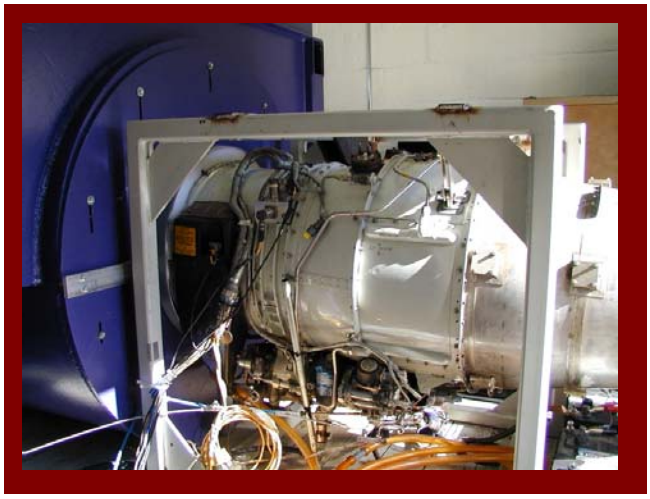

By-pass ratio- 5:1
1 stage axial fan
2 stage centrifugal compressor
2 stage axial HP and LP turbines
Thrust 1330 lbs
Weight 415 lbs
Mass flow rate
(full throttle) 43 lbm/sec
Fan-face diameter 20 in

Figure 3.6 Garrett F 109 Gas Turbine Engine

Following the measurement duct is the aft plenum chamber. The aft plenum chamber is a ½ inch steel tube, four feet in diameter and ten feet long. The size of the aft plenum chamber is to allow the flow to expand to the full inlet diameter of the turbine engine after exiting the ten inch diameter of the measurement duct. Figure 3.6 shows the engine attached to the aft plenum chamber.

Figure 3.6 also shows that the gas turbine engine inlet is inside the aft plenum chamber in order to maintain a closed system. The engine ratings are also listed in Figure 3.6 to illustrate the engine capabilities. To run the system at a throat Mach number of

0.55 required an engine setting of ~90% due to the additional inlet flow ducting upstream which included the test inlet. The engine setting varied somewhat depending on the ambient conditions for the day. In general, engines need to run faster on hotter days in order to achieve the same corrected flow conditions. Humidity also played some role in the ability of the engine to compress the air. An increase in ambient humidity will require a higher setting of the engine to achieve the same corrected conditions.

3.2. Measurements

Steady state total pressure measurements were taken at the AIP using the total pressure 20-probe rake in Figure 3.5. The 20 probes have a head to head spacing of ½ inch except for the 20th probe which is only ¼ inch from the 19th probe. This is in order that all the probes fit entirely within the duct. At each circumferential position, 39 unique data points were acquired. For each measurement, the probe was held stationary for 30 seconds following which 30 seconds worth of data were acquired. At each measurement point, the 30 seconds worth of data (1000 total data points) were averaged to acquire a single average total pressure for that point. These time-averaged total pressures were then used to describe the steady state flow qualities. The transducers used for the measurements were two Scanivalve DSA units with a measurement range of 0-5 Δpsi (differential pressure between the measured total pressure and the ambient total pressure). A total of 24 channels were used consisting of 20 total pressure measurements at the AIP to define the flow quality and four static pressure measurements for the throat Mach number measurement. Static pressure measurements were collected and processed through a Labview code to define the throat Mach number for each measurement station in real time.

Only total pressure measurements are acquired at the AIP in order to utilize the well established methodologies for describing the flow quality quantitatively through total pressure deficiencies. Inlet swirl may also effect the engine operation. This is left for future research.

Because a gas turbine engine was used to pull air through the system, there were some additional considerations in terms of length of testing and ability to increase the airflow. Length of test time becomes an issue, as the engine was run 90% power in order to obtain the desired airflow through the system. One full set of data required hours to obtain, with multiple data sets obtained on a given test day. This amount of time at a high power setting approaches the maximum continuous temperature constraints for the gas turbine engine. For this reason, it was desirable to reduce the test time as much as possible without compromising the quality of the data. Different lengths of data collection time as well as different frequencies of data sampling were tested before choosing a 30 second, 1000 data point, data collection sample. This was the shortest time that did not compromise the steady state time average. Even so, a full sampling of the data at the AIP required 1.5-2 hours.

Due to the facility setup, which pulls in ambient air, humidity can affect the pressure measurements by water condensation within the pressure lines. Due to the initial acceleration of the air, and therefore falling temperature, condensation will occur if the inlet air is too humid at the entrance. This was an important factor governing when testing could occur. Testing was limited to days where the ambient relative humidity was less than 75%.

In order to achieve a fine grid of data points at the AIP, two traversing units were used as seen in Figure 3.5. The circumferential traversing unit allowed automated movement of the pressure rake up to 45 degrees. Every 45 degrees, the measurement duct, with the traversing units attached, could be rotated 45 degrees. Since the probe rake covered the diameter of the AIP, the rake only needed to be rotated through 180 degrees. Five rotations were actually used so that there was some data overlap, but the edge points were more attainable (0 and 45 degrees for each section). Measurements were taken every ten degrees circumferentially. Looking downstream, the measurements always started at zero degrees in the Cartesian coordinate system and rotated counter-clockwise. The linear traverse was used to obtain a finer grid of data points at the AIP. With probe heads spaced ½ inch apart, only one movement in the radial direction was necessary. This allowed the collection of data points ¼ inch apart, radially. In all, this allowed for 702 unique data points at the AIP. This density of data points at the aerodynamic interface plane allowed the resolution shown in the total pressure contour plots. These contour plots are useful in providing a visual depiction of the flow field.

Due to the unsteadiness of the engine, a criterion was needed to determine whether the operating condition had changed. During testing, the throat Mach number was measured at each position of the probe rake. Therefore, the variation in Mach number was monitored at each position to determine whether the operating point had changed. Data points that were determined to be at a different operating condition were discarded, and the data set was repeated. The Mach number was required to stay within 0.01 of the desired Mach number.

3.3. Flow Control

The STRICT inlet duct is being considered for flight application. It is still in the static ground testing phase to evaluate the level of distortion produced at the AIP. A flow control technique was developed by Lockheed Martin to improve the total pressure recovery and flow uniformity at the AIP. CFD studies were used to evaluate several flow control configurations to determine which designs would be manufactured and tested experimentally. Throughout the work described in the current research, a single configuration was used. This configuration employed vortex generators in the form of a single row of microjets located on the top of the duct wall just upstream of the second turn in the duct. These microjets were angled to counteract the naturally occurring vortices from the inside of the second turn of the duct. The jets are angled in both the axial direction and the circumferential direction; however, the actual angles are proprietary. A schematic showing the angling of the air jets is shown in Figure 3.7. Here the jets can be seen to be angled with respect to the y and z axes, but inline with the x axis. This requires precise knowledge of the inception of flow separation in order for the jets to be positioned properly in the streamwise direction. The angle and strength of the vortices at the location of the microjets must also be known to some degree in order to provide flow control jets of the proper strength and in the right direction. Previous tests indicate that the configuration tested in this work is the optimum microjet configuration. Variations of the microjet vortex generators were tested previously in a study at NASA Glenn Research Center including multiple rows, different exit angles, and additional microjets.

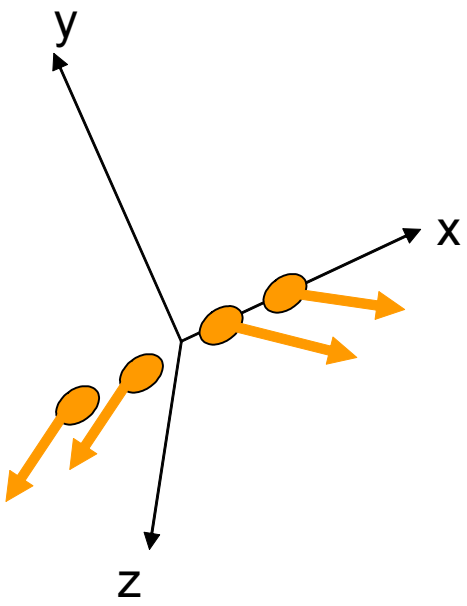

Figure 3.7 Schematic Showing Angle of Microjets

Figure 3.8 shows the location of the microjets on the inlet duct for the configuration tested here. The plenum surrounding the jet openings can also be seen in Figure 3.8. Air was supplied to this plenum through a separate stationary compressor, connective plumbing, and a control valve. The plenum chamber is fed from both sides in order to provide more uniform pressure at the base of each microjet. In the aircraft this air will be supplied by a direct bleed from the fan. The plenum chamber allows an even, steady distribution of air to each of the microjets. The pressure in the plenum chamber is ~40psi. Due to the large demand for bleed air in this particular application, the bleed air was limited to 1% of the inlet mass flow. This bleed does not significantly impact the engine operation, but in combination with expected bleeds for other applications, the limit is necessary.

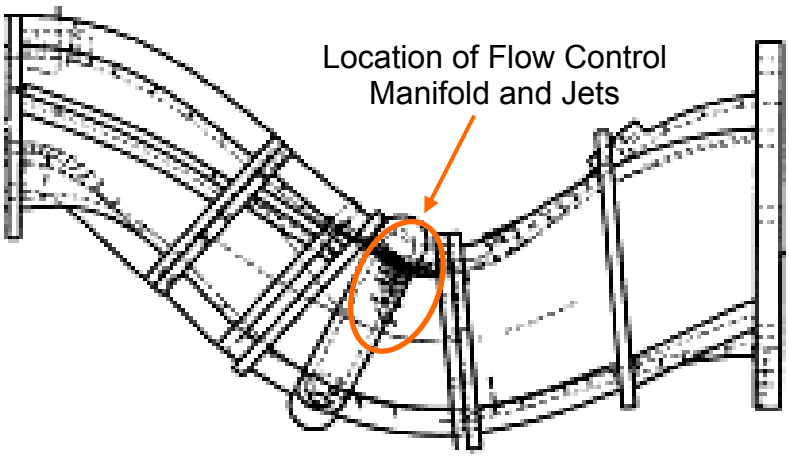

Figure 3.8 Location of Flow Control Microjets

3.4. Simulated Flight Conditions

Measurements were taken for different simulated flight conditions representing cruise flight, angle of attack, and asymmetric distortion. In this way the flow control system was tested at the design condition of cruise flight as well as for off-design operation with additional symmetric (angle of attack) and asymmetric distortions. The predicted flight condition of angle of attack was determined through computational fluid dynamic (CFD) solutions of the flow field at the inlet throat (courtesy of Lockheed Martin). These CFD predictions were then simulated experimentally by adding grids to produce total pressure losses in the predicted regions of loss. The flow field at the AIP was measured to determine changes in flow field due to angle of attack. Asymmetric distortion was created by removing one side of the grid. AIP measurements were also taken to determine the effect of asymmetric distortion on the AIP flow quality. Additionally, the flow control technique was tested to determine its effectiveness at the off-design conditions.

3.4.1. Cruise Flight

The cruise flight condition involved a ten inch long constant area section at the entrance to the duct. The cross sectional geometry matched that of the initial duct cross section. This constant cross sectional area section accounts for the forward flight effect, or the forebody boundary layer growth corresponding to the aircraft traveling through stagnant air at a cruise condition. The experimental tests were run at a throat Mach number of 0.55 due to facility limitations.

Figure 3.4 shows the constant area section prior to the first turn of the inlet duct. In this constant area section the Mach number measurements are made. Figure 3.9 is a CFD prediction of the boundary growth due to this ten inch segment. Based on CFD studies which included the entire airframe, this constant area section is used in order to simulate the forebody boundary layer ingestion.

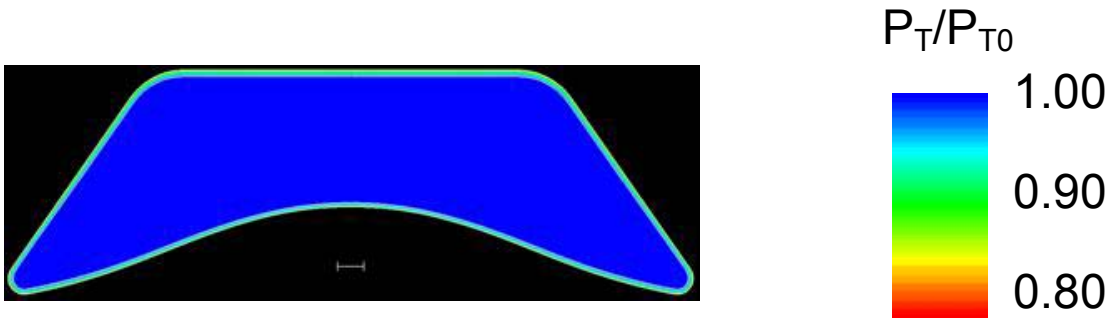

Figure 3.9 Throat Total Pressure CFD Profile for Cruise Flight Condition without Flow Control

3.4.2. Angle of Attack

For the angle of attack simulation, computational fluid dynamic results were used to generate the desired throat profile at several different angles of attack. The CFD solutions involved the entire airframe angled relative to the incoming flow. The total

pressures at the inlet throat cross section were provided by Lockheed Martin. These results show that at an angle of attack of 15 degrees, large flow distortion begins in the corners of the throat. With an angle of attack of 20 degrees, this region of flow distortion continues to grow. The total pressures at the inlet throat are used to experimentally reproduce the CFD predicted conditions because the CFD solutions are more accurate at the throat cross section than at the AIP. Due to the difficulties in accurately representing vortex dissipation within a CFD code, the results further downstream become less accurate.

Figure 3.10 shows the Lockheed Martin generated CFD profiles corresponding to an angle of attack of 15 degrees (Figure 3.10a) and 20 degrees (Figure 3.10b). Flight data and wind tunnel test data are not available for this inlet; therefore, CFD results are used. (In the future, when specific flight test data are obtained, they should be compared with the CFD predictions for angle of attack throat profiles to verify this testing procedure.) The cruise flight condition without flow control (Figure 3.9) shows uniform flow throughout the flow area with some boundary layer along the walls. There is virtually no pressure loss in the core flow region of the throat at cruise flight. Figure 3.10a (Angle of Attack = 15 degrees) shows the development of total pressure loss in the corner regions of the throat area. It also shows an increased boundary layer, as expected, primarily at the top and bottom of the duct with some increase along the side walls. Figure 3.10b (Angle of Attack = 20 degrees) shows continued increase in total pressure loss in the corner region especially towards the outside wall of the corner. In addition, the boundary layer is further increased with significant growth along the top and bottom

walls. Again, there is additional growth of the boundary layer on the side walls compared to the 15 degree angle of attack case.

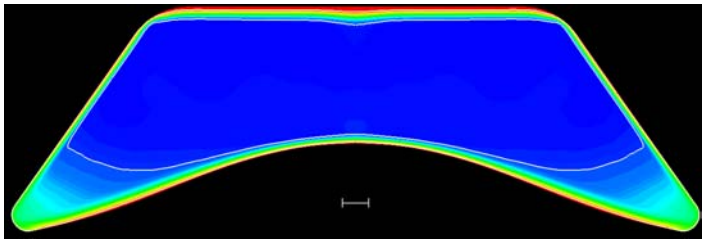

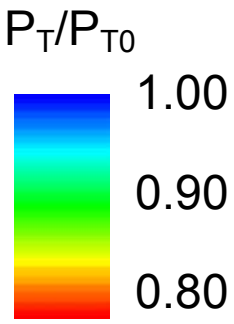

a) Angle of Attack = 15 degrees

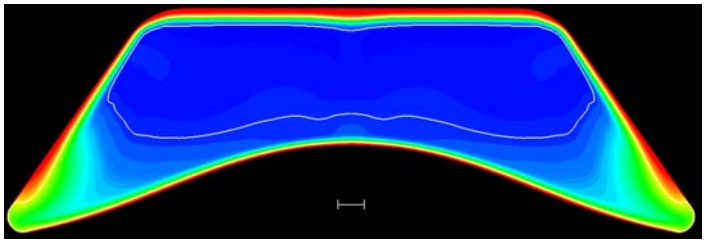

b) Angle of Attack = 20 degrees

Figure 3.10 CFD Throat Profiles for Angle of Attack =15 and 20 deg

Figure 3.10 illustrates the desired profiles to be generated experimentally to evaluate the resulting distortion at the AIP. Preliminary tests were run in a small-scale wind tunnel to determine the pressure drop generated with various screens and honeycomb materials covering only part of the available flow area. Ultimately, approaches using screens were decided upon. As an example, Figure 3.11 shows the screen tested to generate the desired angle of attack simulation.

Figure 3.11 Pressure Loss Grids used to Simulate Angle of Attack (Screen Material)

Although there is information available in the literature (Baines and Peterson, 1950; Doerffer and Bohning, 2000; Roach, 1985; Engineering Sciences Data Item No. 81039, 1981) regarding the pressure loss through screens, it deals with screens that cover the entire flow area. These studies in the literature were used to find a starting point in preliminary testing of screens in this research. In this case it was desirable to produce a pressure drop only in the corner regions of the throat area. In addition, the pressure drop required was on the order of 5-10% of the inlet total pressure. Because of the tendency of the flow to avoid the regions with additional blockage, having the screens cover only a portion of the flow area produced a greater pressure loss in that region than reported results for screens covering the entire flow area.

Figure 3.11 shows the two screens used to simulate the total pressure losses caused by angle of attack. The screens were located in the corners of the duct cross-section based on the CFD predictions which showed that angle of attack generates additional total pressure losses in these corner regions. The extent of the screen in the flow area is similar to the desired distortion region. The wire screen used in the test had a wire diameter of 0.06 inches and a spacing of 1.0 inches. The increased boundary layer due to angle of attack is generated by an additional six inch constant area section

upstream of the ten inch constant area section used for the cruise flight condition (see Figure 3.4). The six inch extension was chosen based on CFD predictions of the required boundary layer growth for the angle of attack simulation. The screen material shown in Figure 3.11 is in between the six inch constant area section and the ten inch constant area section.

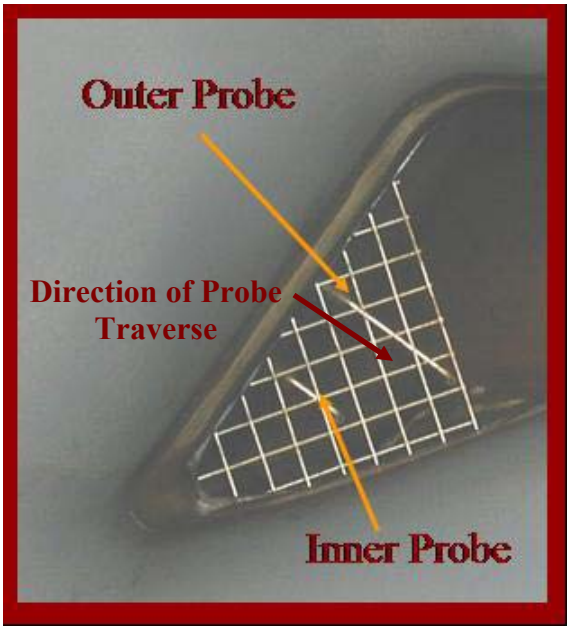

Figure 3.12 Throat Total Pressure Probes

Two probes were inserted ten inches downstream of the screen (Figure 3.12), at the end of the constant area section, to measure local flow behavior and determine if the experimental results matched the CFD desired flow profiles at the inlet throat. These probes are also shown in Figure 3.12 looking downstream. From the figure, it may appear that the probes are directly behind the screen, but they are actually ten inches downstream, still within the constant area portion of the duct. This is just upstream of the first turn of the inlet duct in the throat region. One probe is farther into the corner region in order to measure the higher total pressure gradient in this region. The spacing between

the probes is 1.5 inches. Both probes were traversed manually along the body of the probe. This enabled total pressure measurements to be obtained every ¼ inch. Figure 3.12 shows the direction of probe traverse. In order to obtain more measurements in the region of interest, the flow would have been disturbed either by having a probe rake that was too large relative to the flow region of interest or by having additional access holes in the inlet wall which may have affected the local boundary layer. The actual region of interest is only ~5-6 in^2. Once the throat total pressure profiles were obtained, they were compared to the CFD profiles. After verifying the throat total pressure profiles, these probes were removed and the access holes were plugged before obtaining total pressure profiles at the AIP.

3.4.3. Asymmetric Distortion

The asymmetric distortion case was generated by using only one side of the symmetric distortion generation system for angle of attack. In this way an asymmetric distortion was added to the duct and the response at the AIP was measured. It is unknown whether or not this represents a realistic flight condition. This experiment is only a first attempt to determine the effect of asymmetric distortion on the flow quality at the AIP. Asymmetric distortion would be encountered in flight through sideslip. Sideslip can be generated by a sharp turn or by strong cross winds. For this particular case, sharp turns are not expected to be a part of normal flight plans, but strong crosswinds could be encountered.

3.5. Uncertainty

As with all experimental work, there is uncertainty in the data acquisition process and the resulting calculations. In this work, the total pressure measurements for the AIP total pressure data and the static pressure measurements for the Mach number calculation were acquired using two Scanivalve DSA 3017 with 0-5 psid transducers. Additional measurements were required for the mass flow injection rate. Because the mass flow injection rate was controlled using a closed loop control system, the uncertainty presented here is based on experimental repeatability results. These uncertainties are found in Table 3.1. The method of uncertainty propagation is outlined in Appendix A.

Table 3.1 Uncertainty in Data Acquisition

Variable	Measurement	Uncertainty	Uncertainty (% Avg value)
Pressure	AIP Total Pressure Static Pressure for M	0.0025psid 0.0025psid	0.018% 0.021%
Mach Number	Uncertainty Propagation	0.000461	0.084%
Flow Injection Rate	Mass flow rate	0.05598lbm/s	3.4%

3.6. Summary

A static ground test facility was developed in order to create predicted flight conditions experimentally. In this way, the change in flow behavior at the AIP could be examined and evaluated for design and off-design flow conditions. A flow control technique has been developed by Lockheed Martin to improve the flow quality at cruise condition for this inlet duct. This flow control technique can now be evaluated at off-design conditions to determine its effectiveness. The method for simulating off-design

flight conditions was presented. Data will be presented to verify the effectiveness of this approach to produce off-design flight conditions in a static ground test facility. The uncertainty of these measurements was also presented.

4.0 Data Reduction Techniques

The experimental data consist of detailed total pressure measurements at the AIP. These data were then used to describe the flow field through established industry methodology. SAE Aerospace Recommended Practice 1420 documents the established industry methodology for describing inlet total pressure distortion. Its counterpart, SAE Aerospace Information Report 1419 outlines these recommended practices in more detail. This was the methodology used to determine what data to obtain and especially to reduce that data to a format which allows the most information to be drawn from the data. In addition, a general correlation has been found between harmonic content and fan blade strain limit (Cousins, 2002). Therefore, the harmonic content can be used as an indication of the level of high cycle fatigue or cyclic strain that the inlet flow distortion is producing on the fan blades.

Inlet distortion affects the stability margin of the compression system. The goal of the flow control system is to improve the non-uniform inlet flow to a level that will be acceptable to the engine, specifically the compression system. After examining the flow field at the AIP in detail, the next step is to determine how the different total pressure profiles will affect a compression system. The inlet duct tested throughout this work is in the static ground test phase and the inlet duct is still undergoing significant design revisions. Furthermore, the gas turbine engine to be used with this inlet has not yet been finalized. Given this situation, the benefits of using a high fidelity model do not outweigh the costs in terms of monetary costs, computing power and time. For these reasons, a simpler analytical model has been chosen to examine the effect of inlet

distortion on the stability of a compression system for the flight conditions tested in this research, with and without flow control.

The methodologies used to describe the experimental data are outlined below. The data were examined in detail in order to predict the affect of the different flow fields on the compression system of a gas turbine engine. In this way, potential design challenges can be realized at an earlier design stage.

4.1. AIP Distortion Descriptors

The purpose of the distortion descriptors is to provide an adequate, universal means to describe the flow field leaving an inlet duct or entering an engine. This provides continuity between inlet and engine testing. In addition, the descriptors outlined below serve to draw attention to critical inlet flow distortion.

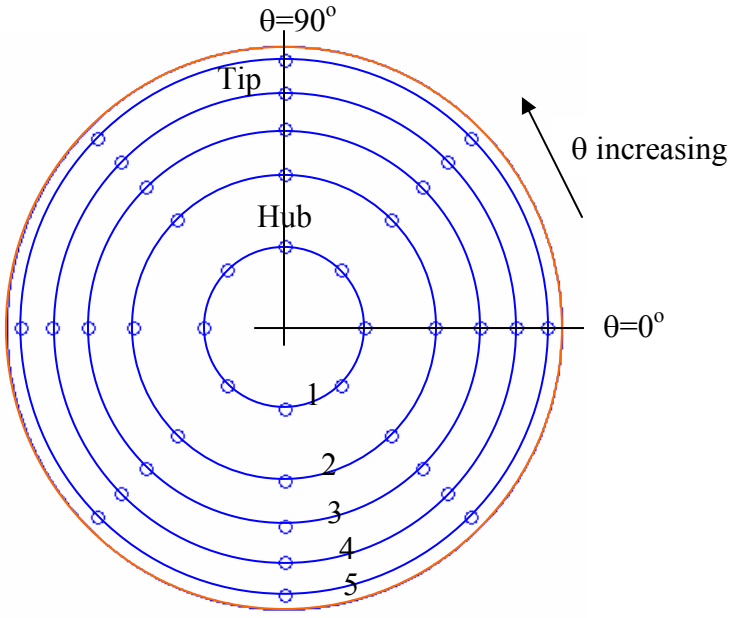

Figure 4.1 SAE 40 points grid

The distortion descriptor elements to be examined are circumferential distortion intensity, circumferential distortion extent, circumferential distortion multiple per revolution content, radial distortion, and harmonic coefficient. Each of the distortion descriptors relies on the recommended data grid which consists of 40 points. This grid is considered to be the minimum number of data points required to describe a flow field. The data plane to be measured is divided into 40 sections of equal area, and the 40 points are the centroids of these sections, as shown in Figure 4.1. The descriptors use the data in terms of five circumferential rings. The inner ring shown in Figure 4.1 is labeled ring one, and the outer ring is ring five. Ring one represents the hub region while ring five lies in the tip region. In some cases rings one and two are combined to describe the hub flow and rings four and five for the tip flow.

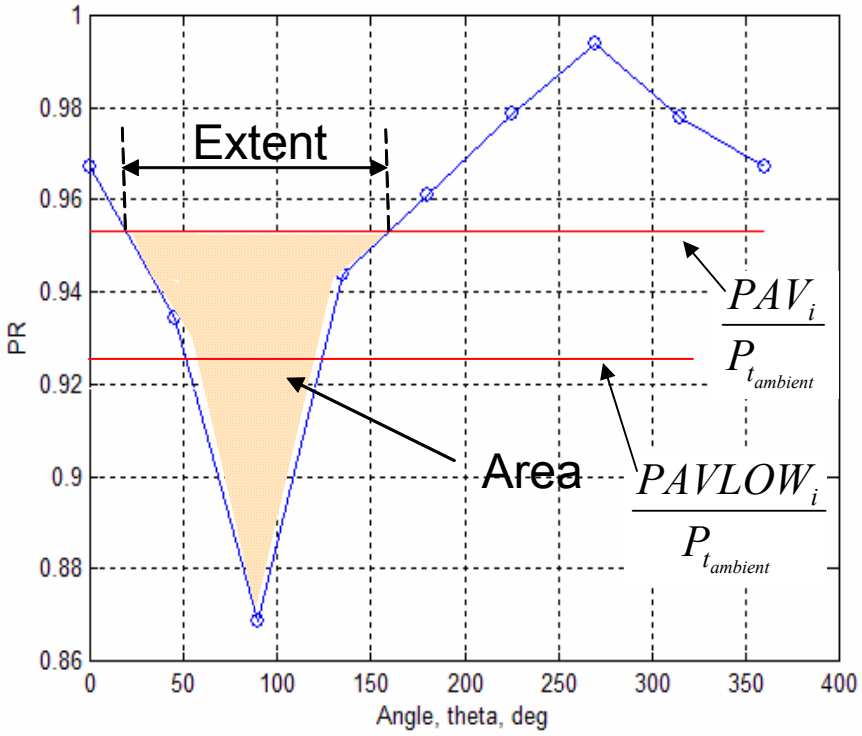

Figure 4.2 Sample Ring Total Pressure Recovery

Figure 4.2 shows a sample of the eight points in a ring. The total pressure ratio (total pressure normalized by ambient total pressure) is shown on the y-axis versus the circumferential position, θ, on the x-axis. The upper red line indicates the average total pressure for the ring (PAV_i). For the example shown, there is only one segment of lower than average total pressure. This is the segment addressed in the following descriptors.

The circumferential distortion extent is defined by:

$$Extent = \theta_i^- = \sum_{k=1}^{K} \theta_{ik}^-$$

$$K = number\ of\ low\ pressure\ regions$$

The extent function illustrates how much of the circumferential region (in terms of degrees) is made up of low pressure regions, as seen in Figure 4.2. The circumferential region of higher than average total pressure, in degrees, is simply θ_{high}=360-Extent. The extent function helps to determine if the distortion is spread out over a large region or concentrated in a smaller region. The addition of the intensity descriptor will better characterize this.

The circumferential distortion intensity is determined by:

$$Intensity = \left(\frac{\Delta PC}{P} \right)_i = \frac{AREA_{P-low}}{EXTENT} \text{ or}$$

$$Intensity = \left(\frac{\Delta PC}{P} \right)_i = \frac{(PAV)_i - (PAVLOW)_i}{(PAV)_i} \text{ where}$$

$$(PAV)_i = \frac{1}{360} \int_0^{360} P(\theta)_i \, d\theta = Ring\ \ Average\ \text{Pressure}$$

$$(PAVLOW)_i = \frac{1}{\theta_i^-} \sum_{k=1}^{K} \int_{\theta_i^-} P(\theta)_i \, d\theta$$

$$K = number\ of\ low\ pressure\ regions$$

$P(\theta)_i$ is a function represented by a linear fit between the total pressure points, and $Area_{P\text{-}low}$ is the area of the low pressure region. The intensity, in combination with the extent function, characterizes the distortion by illustrating whether the distortion is a large total pressure deficit concentrated in a short extent or a relatively mild total pressure deficit spread out over a large extent. This can be seen in Figure 4.2 by using the definition: $\frac{\Delta PC}{P} = \frac{Area_{P-low}}{Extent}$. It is important to look at both circumferential intensity and extent because substantially different cases may appear the same in the view of a single descriptor. The circumferential intensity is directly proportional to the loss in surge margin due to distortion. Therefore, it is desirable to keep the circumferential distortion intensity to a minimum.

For a total pressure distribution with more than one low pressure region, the above descriptors can change. If the second region of low total pressure is directly following the first region with only a small segment of high total pressure recovery in between, the high pressure recovery may or may not be long enough for the fan blades to respond. The extent of high pressure recovery region required for the fan blades to respond is known as the critical angle and will vary based on compression system and shaft speed. The time constant associated with the critical angle is the time required for a fluid particle to travel from the tip of the blade to the throat of the blade as shown in Figure 4.3. The time constant (seconds) is determined by dividing this distance by the relative velocity of the blade at the entrance to the blade passage. The critical angle, θ_{CR} (radians), associated with the time constant is defined as: $\theta_{CR} = \frac{U_{tip} * \tau}{r_{tip}}$. The fan blades

will not be able to respond to distortions or regions of high pressure recovery which cover a smaller angular extent than the critical angle.

Figure 4.4 illustrates the difference between the blade response for a long time constant versus the blade response for a short time constant. The long time constant shows a delayed response to the distortion and does not fully respond to the distortion. The longer time constant indicates that the fluid particles require more time to reach the throat of the blade. This would indicate that the throat of the blade is positioned farther from the tip of the blade or that the speed of the fluid is slower. The short time constant indicates less time for the fluid particle to reach the throat of the blade, allowing the blade to respond to the full magnitude of the distortion.

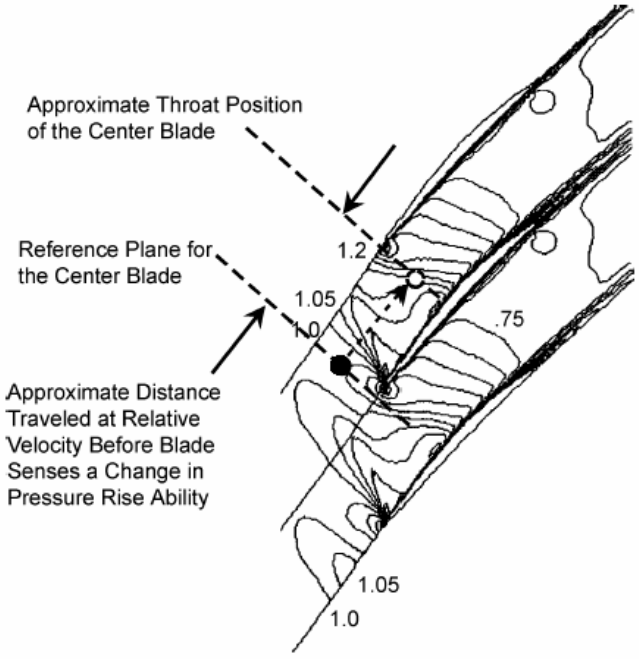

Figure 4.3 Distance Traveled by a Particle Before the Fan Blade Can Respond from Cousins (1997)

Figure 4.5 shows an example of the total pressure recovery in a ring where more than one region of low total pressure recovery occurs. If the extent of the region of

higher than average total pressure recovery does not exceed the critical angle, the circumferential intensity of the distortion is defined as: $Intensity = \left(\frac{\Delta PC}{P} \right)_i = \frac{AREA_1 + AREA_2}{EXTENT_1 + EXTENT_2}$. If the higher than average total pressure recovery occurs over an extent greater than the critical angle, the circumferential distortion intensity is equal to the intensity of the low pressure region with the largest area, and the multiple regions of low pressure recovery are represented through the MPR content.

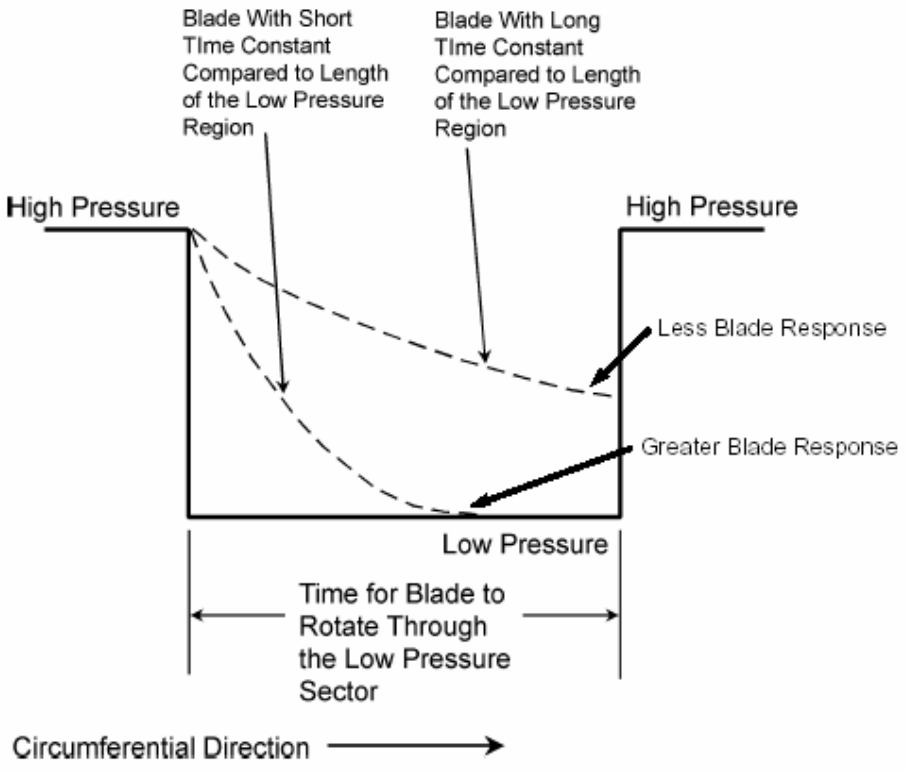

Figure 4.4 Effect of Time Constant on Blade Response from Cousins (1997)

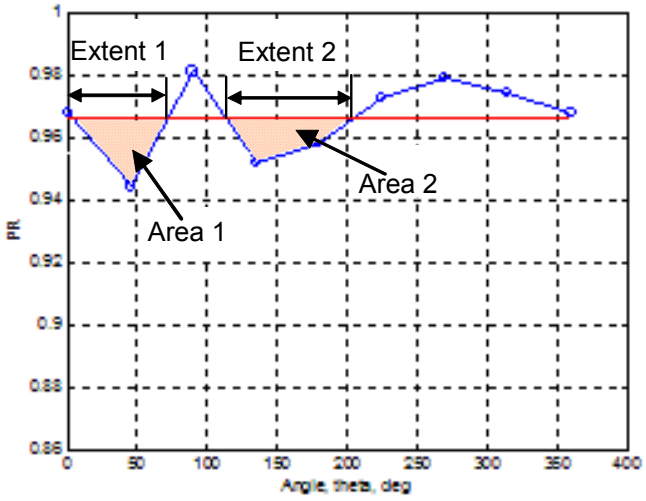

Figure 4.5 Ring Total Pressure Recovery for Multiple Low Pressure Recovery Areas

The circumferential multiple per revolution descriptor is:

$$(MPR)_i = \frac{\sum_{k=1}^{K}\left[\left(\frac{\Delta PC}{P}\right)_{ik}\theta_{ik}^{-}\right]}{\max\left[\left(\frac{\Delta PC}{P}\right)_{ik}\theta_{ik}^{-}\right]}.$$

The MPR descriptor indicates how many regions of low pressure are present in any given ring weighted by the area of these low pressure regions. For example, if there are two regions of low total pressure and one is half the area of the other, then the MPR value will be 1.5 even though there are two regions of low total pressure. In this way the MPR descriptor takes into account the relative severity of each region of low total pressure. From the point of view of the fan, just downstream of the AIP, the fan blades will travel through MPR regions of low total pressure each revolution.

The radial distortion intensity is defined as:

$$\left(\frac{\Delta PR}{P}\right)_i = \frac{(PFAV)-(PAV)_i}{(PFAV)} \quad \text{where}$$

$$(PFAV) = \frac{1}{N}\sum_{i=1}^{N}(PAV)_i$$

and N is the number of rings, five in general. Therefore, radial distortion can be either positive or negative. In addition,

$$\frac{1}{N}\sum_{i=1}^{N}\left(\frac{\Delta PR}{P}\right)_i = 0\,.$$

The radial distortion intensity is an indication of the concentration of distortion in each ring. A positive value of radial distortion indicates a total pressure loss, whereas a negative value of radial distortion signifies higher than average total pressure recovery.

The harmonic content is defined as the root mean square of the Fourier transfer sine and cosine coefficients. The Fourier transfer function is based on the blade reference frame which moves through the inlet distortion with each revolution of the fan blades. In this way the steady state pressure distribution becomes time variant in the blade reference frame. The harmonic content is defined as:

$$n/rev = A(n) = \frac{2\sqrt{\left(a_n{}^2 + b_n{}^2\right)}}{P_{avg}} \qquad \text{where}$$

$$a_n = \frac{1}{n^2\pi}\sum_{i=1}^{NR} b_i\left[\cos(n\theta_{i+1}) - \cos(n\theta_i)\right]$$

$$b_n = \frac{1}{n^2\pi}\sum_{i=1}^{NR} b_i\left[\sin(n\theta_{i+1}) - \sin(n\theta_i)\right]$$

$$b_i = \frac{PR(i) - PR(i+1)}{\theta(i) - \theta(i+1)}$$

$$NR = number\_of\_circumferential\_locations$$

The Fourier series coefficients are subject to the Nyquist criterion for sampling which requires two data points per frequency; therefore, the frequency content can only be determined up to half the number of data points. Using the SAE 40 points grid with 8 points per ring, this would allow frequency content up to 4/rev, and harmonic content can only be determined up to 3/rev.

These distortion descriptors will be used throughout this work to describe the experimentally determined flow fields for different simulated flight conditions with and without flow control. In this way, the improvement in flow field at the AIP due to flow control can be quantified and the changes in AIP flow field for different simulated flight conditions can be determined. The circumferential distortion intensity and extent will directly affect the stability margin of the compression system; while, the harmonic content will affect the cyclic fatigue. Compression system modeling can also be used to determine how the total pressure inlet distortion will affect the stability margin. This results in a more quantitative evaluation of the effect of inlet total pressure distortion.

4.2. DYNTECC – Dynamic Turbine Engine Compression Code

A modified parallel compressor model was utilized to describe the effect of several circumferential inlet distortion profiles on a compression system. The main advantage of this approach is the ability to break the incoming flow into several circumferential segments while still using a one-dimensional code. Since the engine for this inlet has not yet been chosen, and the inlet is still undergoing significant design changes, the detail of blade shape and radial distribution of the flow is not worth considering at this stage of the research.

Figure 4.6 shows a schematic of the parallel compressor concept. Here the compressor annulus is broken into four separate compressors which can have varying inlet conditions but a common exit condition. In this application, the inlet total pressures were varied for each parallel compressor while a common exit static pressure was imposed. The divisions are chosen based on divisions in the total pressure characteristics of the flow. In classical parallel compressor theory each compressor operates independently with no cross flow between compressors. Recent research has allowed advancements in the parallel compressor theory which enable cross-flow between adjacent segments to be accounted for.

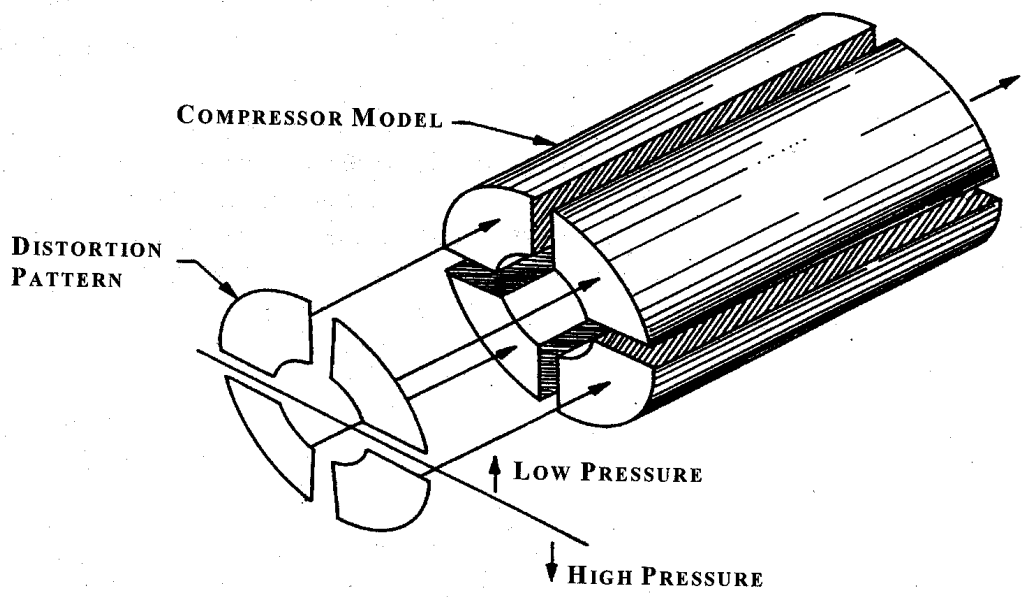

Figure 4.6 Parallel Compressor Concept (from Davis et al, 1995)

The DYNTECC model is a one-dimensional compression system model to evaluate the performance and stability of compression systems. A finite difference

technique is used to solve the conservation of mass, conservation of momentum and energy equations in the axial direction. Bleed effects, shaft work and blade forces are included as source terms in the equations. These source terms are determined from the pressure and temperature stage characteristics which are an input into the program. The model has been modified to include circumferential and radial mass redistribution, dynamic blade response, and radial work redistribution. In the current research only circumferential distortion was examined through DYNTECC; therefore, the radial modifications will not be discussed. To truly capture radial effects, a model of higher dimension is required, and this need must be balanced by the greater computational requirements that come with higher order models.

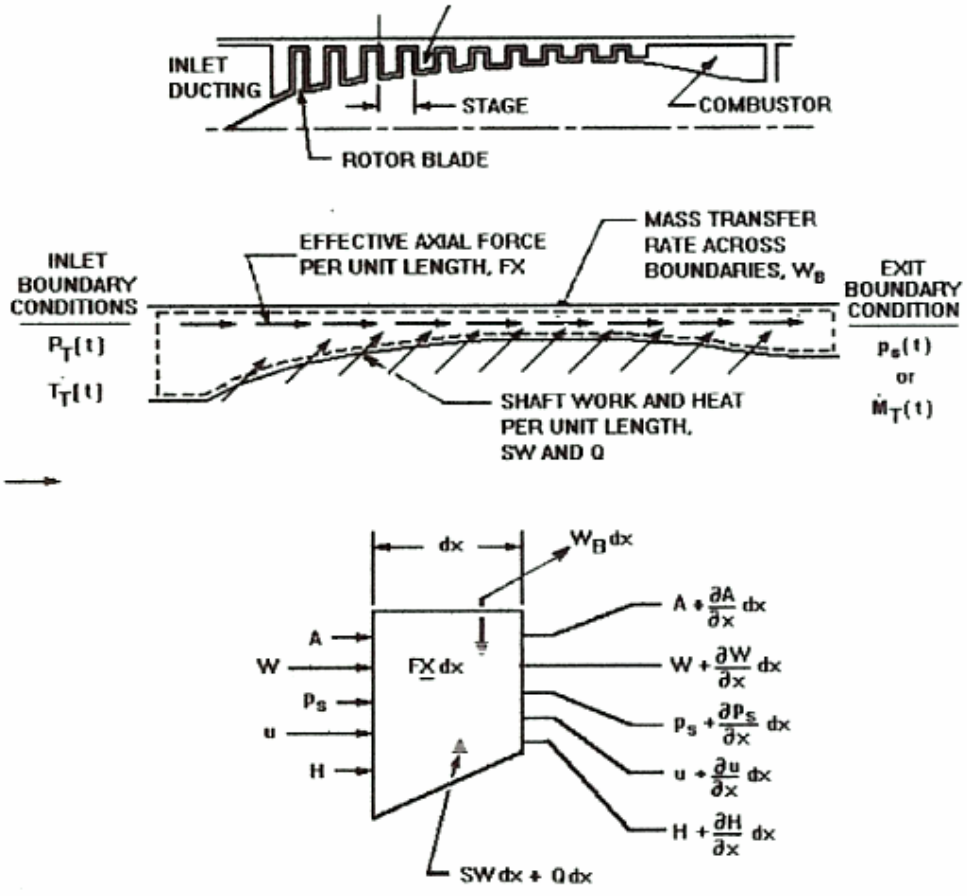

Figure 4.7 DYNTECC Control Volume Approach (from Davis et al, 1995)

DYNTECC uses a control volume approach, breaking the compression system into control volumes by stage consisting of rotor-stator or stator-rotor pairs, depending on how the stage characteristics are defined. Because this is a one-dimensional code, variations within the blade passage are too detailed for the overall complexity level of the code. Therefore, the grid resolution of one control volume per stage is adequate in keeping with the one-dimensional nature of the code. The other control volumes consist of entrance ducting and exit ducting which can have losses included in them. The three governing equations are applied to each control volume. The control volume approach can be seen graphically in Figure 4.7.

Each of the parallel compressors is evaluated separately, and in the modified parallel compressor theory there is some interaction between adjacent circumferential segments. Circumferential total pressure distortion distribution can induce circumferential mass flow due to static pressure differences. Rather than incorporating the circumferential momentum equation, the effects are modeled within the one-dimensional format of the code. The fluid can only move circumferentially in the gap between the rotor and stator, in a manner similar to orifice flow. This approximation was first used by Kimzey (1977). Figure 4.8 shows the orifice gap analogy graphically. For more details on the circumferential mass redistribution in DYNTECC, the reader may consult Shahrokhi (1995).

In parallel compressor theory, each of the parallel compressors is assumed to operate on the ideal stage characteristic. The overall operating point is determined by the average of the operating points for each of the parallel compressors as seen in Figure 4.9. The stall point for the parallel compressor model is determined in a similar fashion.

When one of the parallel compressors reaches the stall point on the ideal stage characteristic, the whole compressor is defined as stalled, and the parallel compressor operating points are averaged to obtain the stall point for that condition. In this way the stability line will drop with increased distortion in one segment of the parallel compressor model, and the operating point will move up, but the effects will be less severe than if the distortion were to cover the entire inlet area of the compression system.

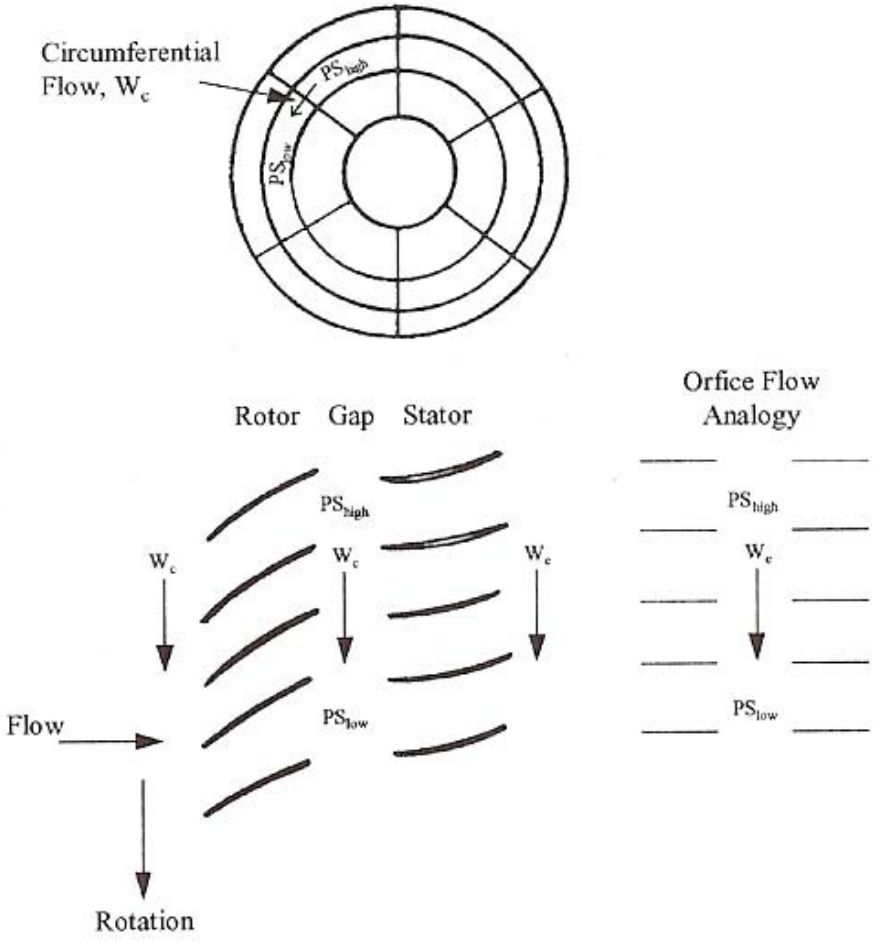

Figure 4.8 Circumferential Mass Redistribution – Orifice Flow Analogy (from Davis et al, 1995)

The compression system used for the modeling was NASA Stage 35. Stage 35 represents the inlet stage for an eight-stage compressor. It is a single-stage axial flow transonic compressor that was tested experimentally for three corrected rotor speeds (Reid and Moore, 1978). Therefore, there were three available speed lines for this simulation. Stage 35 was chosen based on availability of stage characteristics. The stage characteristics were already available as input files within DYNTECC. As an inlet stage, the pressure ratio across Stage 35 is not very aggressive, making it more similar to a fan stage. In this research the inlet distortion will affect the fan stages most severely and will be dissipated before reaching the rest of the compression stages.

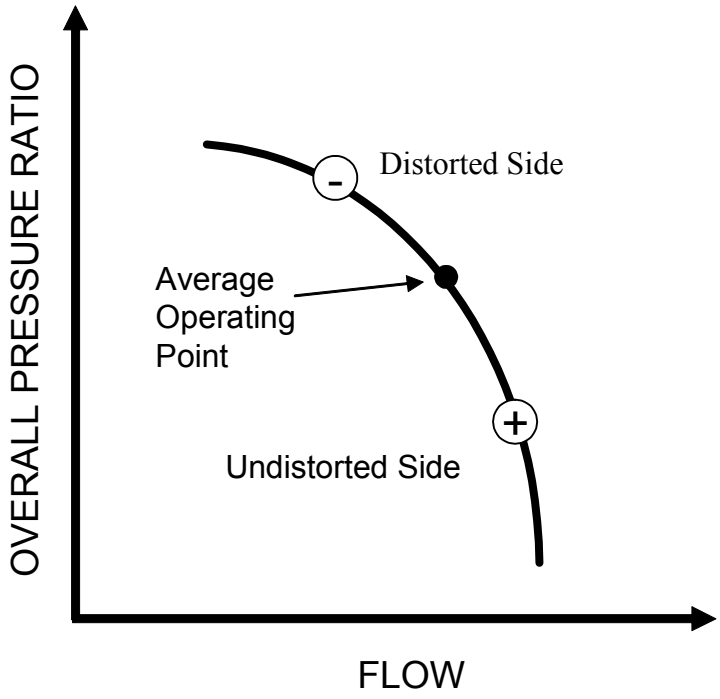

Figure 4.9 Parallel Compressor Operating Point Analysis (from Mazzawy, 1977)

The stage characteristics for Stage 35 can be found in Figure 4.10 where the total pressure ratio minus one is plotted as a function of the corrected mass flow rate. Each of the speed lines shows a shallow region of response where the changes in pressure ratio

are minor for a significant range of mass flow. The 100% speed line shows a sharp drop in pressure ratio for a short region of mass flow, indicating the choked flow region. This region is not seen at 90% or 70% speeds, but may still exist beyond the data shown. The dotted line shows the stability limit for the compressor stage. Figure 4.10 also shows that the stable operating region is largest for the 70% speed and decreases with increasing speed.

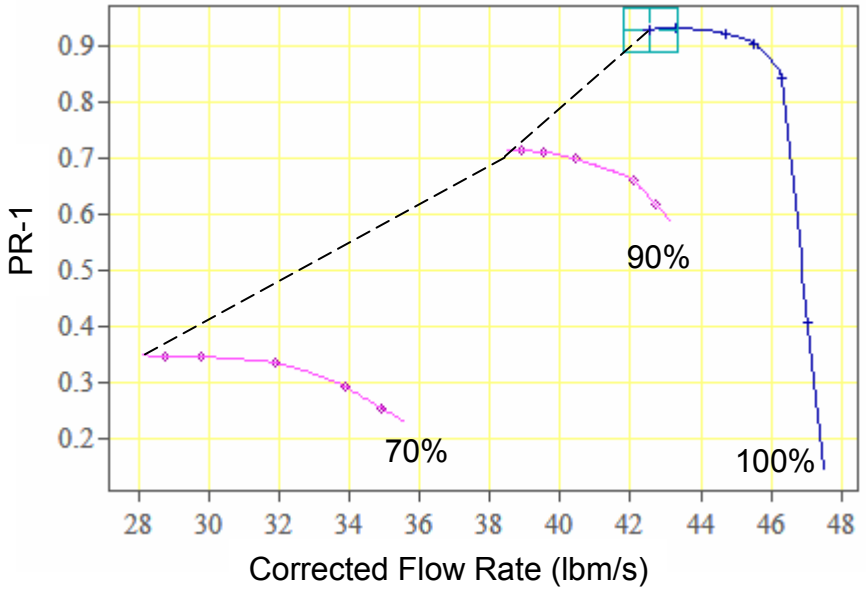

Figure 4.10 Stage 35 Compressor Map

In order to provide continuity between the inlet total pressure distortion data and the compression system model, the mass flow rate was normalized by the flow area and matched for the two cases. This matching occurs at the 70% speed line. The mass flow through the compressor changes as the operating points move along the speed line; however, these changes in mass flow rate (<10%) are believed to be small enough to not change the qualitative results from the simulation.

DYNTECC required several inputs for operation. The parallel compressor option was used to capture the effect of variations in inlet total pressure. The speed of the rotor was also required. For this application, the exit static pressure, or backpressure, of the compressor was specified. The code also allows exit conditions of Mach number or mass flow rate to be specified. The simulations in the current research were carried out with no change in static pressure, or a back pressure equal to the ambient total pressure. This represents a compressor rig test rather than an engine. In order to obtain the stability limits, the back pressure was ramped until instability occurred, or one of the parallel compressors reached the undistorted stability limit.

As noted earlier, the parallel compressor theory averages the operating points from the parallel compressors to arrive at the overall operating point. Therefore, the operating points were shown to move off the original speed line onto what is known as the distorted speed line. The compressor simulation begins at an operating point far from the stability line and reaches a steady state operating point for clean inlet flow. The distortion is then added to the parallel compressors through a linear ramp to the desired distortion over a time period of 0.03 seconds. The compressors then reach a steady state distorted operating point. These operating points are averaged to obtain the overall compressor operating point. The operating points for each of the parallel compressors are calculated through the conservation of mass, conservation of momentum and energy equations.

The stall points for each of the test cases were determined in a similar manner to the operating points. The clean inlet steady state condition was achieved after which the distortion pattern was linearly ramped to the desired distortion for each segment.

Following the distorted operating points, the exit static pressure was increased linearly until instability was reached in one of the parallel compressors. At this point the overall compressor was said to stall, and the model calculations stopped. The operating points for the four parallel compressors were averaged to obtain the stability limit for the overall compressor.

4.3. Summary

The total pressure data at the AIP will be evaluated in terms of circumferential distortion intensity and extent, multiple per revolution content, radial distortion intensity, harmonic content and stability margin. The distortion intensity and extent are directly related to the change in stability margin while the harmonic content is indicative of the cyclic fatigue on the compression system. The stability margin prediction is based on total pressure distortion alone through the use of a parallel compressor model formed with DYNTECC.

5.0 Results

The STRICT inlet duct was tested at three different simulated flight conditions: cruise condition, angle of attack, and asymmetric distortion. The angle of attack case matched a CFD predicted total pressure profile at the inlet throat. In this way, a realistic flight condition has been simulated. Each flight condition was tested with and without flow control at a throat Mach number of 0.55 to determine the effect of flow control on each test case. The flow control, in the form of mass injection through microjets, used 1% of the inlet mass flow rate. Wall static pressure measurements are presented for the baseline case with and without flow control in order to verify the expected flow development within the inlet duct.

Total pressure measurements were taken at the aerodynamic interface plane (AIP). From these detailed measurements, total pressure contours were generated which show pressure deficiencies in the flow. The total pressure measurements were also used to describe the flow through multiple descriptors including circumferential distortion, multiple per revolution (MPR) values, circumferential extent, radial distortion and harmonic coefficients. These distortion descriptors are used to evaluate the flow quality at the AIP.

Finally, a compression system model was used to evaluate the impact of the flow field on the stability margin of a compression system. The total pressure distortion was used to determine the change in stability margin based on variations in the total pressure recovery for the different flight conditions tested and the addition of flow control. In this way the impact of inlet total pressure distortion can be evaluated as it affects the stability of the gas turbine engine.

5.1. Flow Control Study

The flow control system was limited to a mass flow injection rate of 1% of the inlet mass flow rate. This limit was based on the total available bleed air balanced by the number of applications requiring bleed air. Studies have been performed to investigate the effects of bleed air percentages as well as bleed air locations. The current research included a brief study of the effect of bleed air as a percentage of inlet flow rate on total pressure recovery and circumferential distortion. The study involved a brief investigation of AIP flow field changes for different bleed rates at several throat Mach numbers. This investigation will be used to illustrate the effective design of the flow control system which was designed for 1% bleed.

Analytical studies have been performed in the past and are available in the literature regarding the effects of bleed air rate as well as location of bleed air. Wellborn (2000) performed system level studies to determine the effect of bleed air location and flow rate on engine performance. In his work, he divided the compression system into three components: fan, intermediate pressure compressor, and high pressure compressor. He examined bleed within individual components (bleed from the high pressure compressor delivered at the beginning of the high pressure compressor) and between components (bleed from the intermediate pressure compressor delivered within the fan stages). The study concluded that bleed within an engine component could be beneficial to the engine performance, but bleed between components was not effective. Therefore, bleed air delivered within the inlet could improve performance if the bleed came from the fan. Simple thermodynamic analysis of the effect of bleed air on a system level shows that with increasing bleed rate or decreasing bleed nozzle efficiency, the work required

for bleed increases. Therefore, limiting the bleed air also increases the efficiency of the bleed.

A preliminary study of the effectiveness of the Lockheed Martin flow control technique for various bleed rates and throat Mach numbers was conducted as a part of the current research. Figure 5.1a shows the reduction in circumferential distortion due to varying levels of flow control. The independent axis shows the percentage of inlet mass flow injected through the microjets for each case while the dependent axis shows the circumferential distortion value as a percentage of the maximum circumferential distortion. Figure 5.1a shows that the percentage of circumferential distortion is significantly reduced with the addition of flow control, but no significant distortion reduction occurs with flow control levels greater than 0.8%. Figure 5.1b shows the improvements in area-averaged pressure recovery due to varying levels of flow control effort. The pressure recovery does continue to improve with the addition of flow control; however, some of this improvement is simply due to the additional mass flow injected into the system at a higher total pressure. A diminishing return in pressure recovery is seen for flow control greater than 1% of the inlet mass flow rate. More data points in these two charts would be beneficial to discern the optimum flow control injection rate for this configuration. The current research employed the flow control at a mass injection rate of 1% of the inlet flow rate. This value was the design value for the flow control technique. However, this study shows that more testing should be conducted to determine if similar gains could be obtained with less mass flow injection.

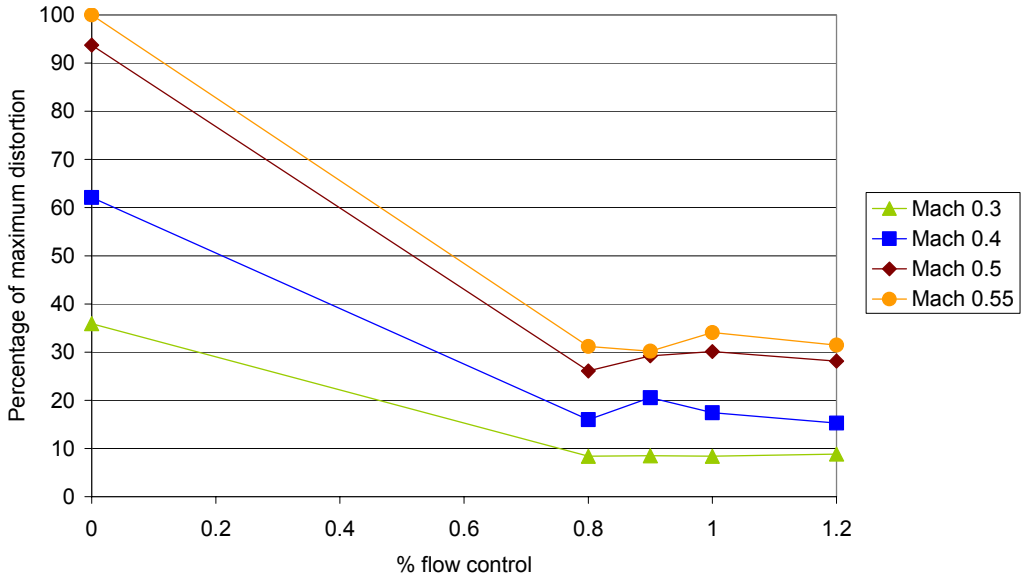

a). Effect of Flow Control Effort on Circumferential Distortion

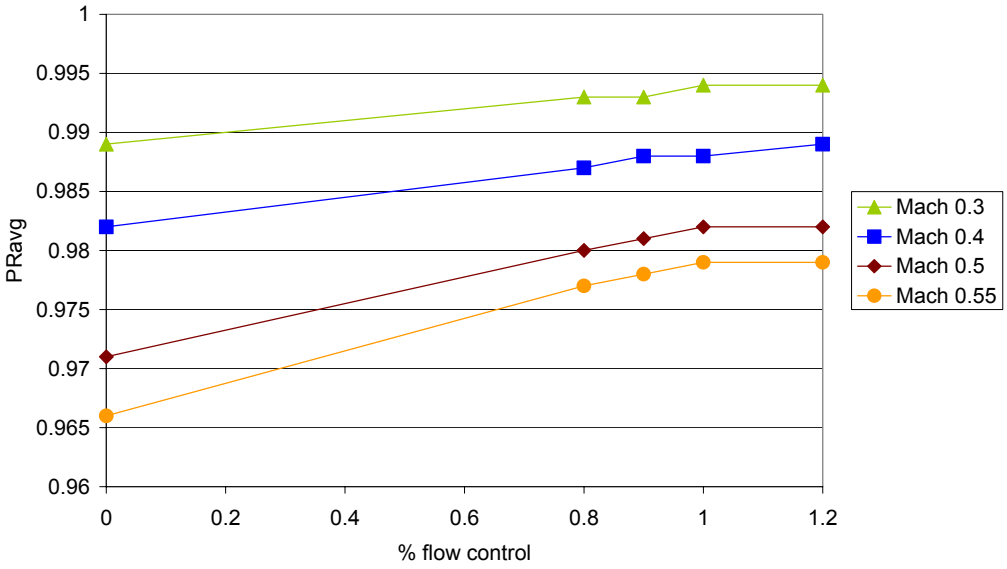

b). Effect of Flow Control on Area-Averaged Total Pressure Recovery

Figure 5.1 Effect of Flow Control Injection Rate on AIP Flow Profile

5.2. Verification of Angle of Attack Simulation

The angle of attack case was developed by reproducing CFD generated inlet throat total pressure fields in an experimental facility. The distortion generating grids are

shown in Figure 3.11. Throat total pressure measurements were obtained using the probes shown in Figure 3.12.

The results for the outer probe location from the two CFD generated angles of attack (Figure 3.10) and the experimental data (configuration in Figure 3.11) are shown in Figure 5.2. Figure 5.2 shows the pressure recovery (total pressure at a point normalized by ambient total pressure) versus the distance from the outside wall (see Figure 3.11b) normalized by total distance between the inside and outside wall. Near the outside wall (shown in Figure 3.11b), the agreement is very close between the experimental results and the predicted results. From the middle of the passage area to the inside wall, the experimental results lie in between the predicted profiles for 15 and 20 degrees angle of attack. Therefore, the flow generated in the experimental test hardware was consistent with expected flight conditions. It was felt that this would be able to determine how different realistic flight conditions such as angle of attack would affect the flow exiting the duct, and also, how the flow control scheme designed for steady state flight would be able to improve the flow produced at these off-design flight conditions of angle of attack and asymmetric distortion.

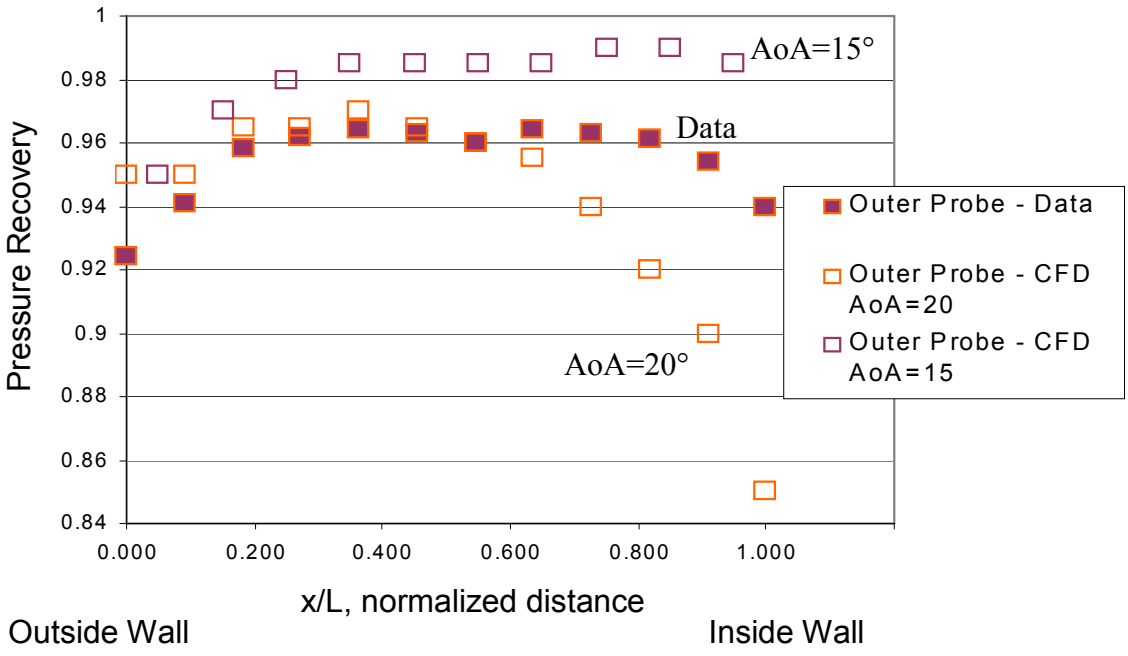

Figure 5.2 Angle of Attack Simulation Throat Total Pressure Profile

5.3. Wall Static Pressure Measurements

While the exact behavior of the flow within the inlet duct is not measured, the streamwise wall static pressure profiles provide insight into the duct flow including approximations of the region of separated vortices and the region of reattached flow. Figure 5.3 shows the wall static pressure distribution along the top and bottom of the inlet duct. The wall static pressure is normalized by the inlet total pressure, or the measured local atmospheric pressure, while the length along the duct is normalized by the overall length of the duct referenced to the entrance of the inlet duct. The constant area section of the duct is upstream of the entrance of the inlet duct and measurements within this section have a negative normalized distance.

The static pressure distribution along the top of the duct is shown in Figure 5.3 above a drawing of the STRICT inlet duct. The flow first experiences an adverse (positive) pressure gradient followed by a favorable (negative) pressure gradient. The source of this behavior is the position of the top of the duct at the outside of the first turn or on the pressure side of the turn. The favorable pressure gradient drops off sharply beginning at x/L=0.40 and continues to about x/L=0.50. At this point the flow along the top of the duct experiences an adverse pressure gradient within the second turn.

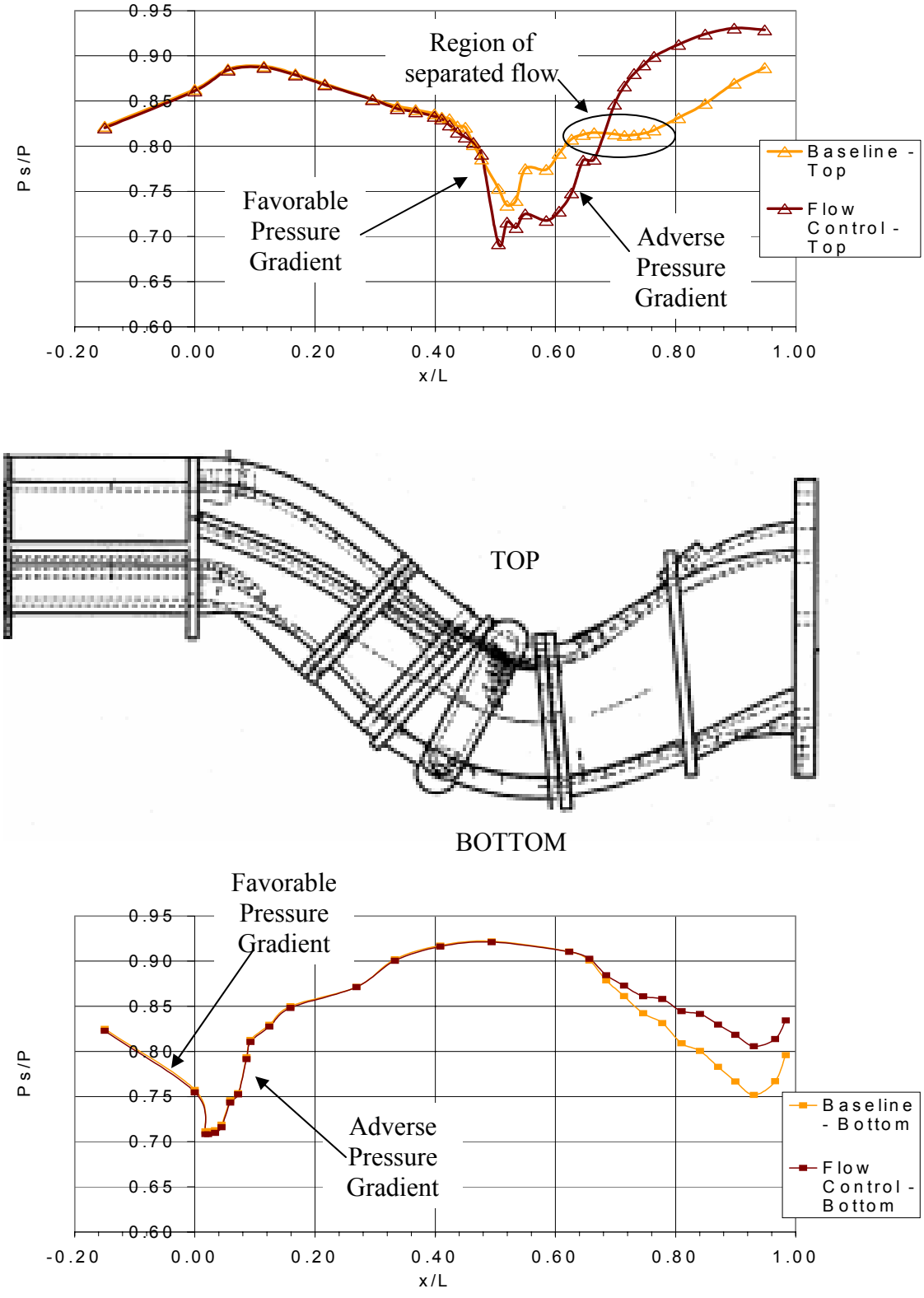

Figure 5.3 Streamwise Wall Static Pressure Measurements

In the second turn the top of the duct lies at the inside of the turn within a region of low momentum. At the second turn the static pressure profiles along the top of the duct with and without flow control deviate. From Figure 5.3, it can be seen that the static pressure for the flow control case is actually lower than the uncontrolled case along the surface of the second turn. The second turn represents the largest flow deficit and is therefore the location of the flow control microjets. The air jets are designed to cancel the vortices formed on the inside of the second turn, or the top of the duct, by creating opposing vortices. Therefore, the air jets are angled away from the wall of the duct in two directions, both radially and axially, and it would seem that the jets carry additional wall fluid with them, creating a lower wall static pressure along the top of the duct through the second turn for the flow control case. The uncontrolled case shows constant static pressure near the exit of the second turn from x/L=0.62 to 0.76. According to several sources (Reichert and Wendt, 1993; Wellborn et al, 1992; Vakili et al, 1985), a constant value of streamwise static pressure (surrounded by an adverse pressure gradient) is an indication of flow separation. Therefore, it can be argued that the vortices induce separated flow at the inside of the second turn in the uncontrolled case. The flow control case shows a continuous adverse static pressure gradient following the second turn, indicating attached flow throughout the region. This adverse pressure gradient reaches a constant value around x/L=0.85 due to the third turn in the duct where the top of the duct becomes the outside of the turn again. In the uncontrolled case, the adverse pressure gradient from the second turn continues following what is perceived as flow reattachment near x/L=0.76. The uncontrolled case does not show a leveling off of the static pressure

for the third turn. It could be that the flow separation delays the reaction to the third turn; however, more data points would be required to show this.

At the exit, the static pressure is higher for the flow control case. There are several possible explanations for this. Mass flow is added to the system for the flow control case allowing higher pressures to be present. In addition, the experimental results will show that the airflow is more uniform in the flow control case and has a higher area-averaged total pressure. For the same mass flow rate, this would require a higher static pressure for the flow control case.

The static pressure distribution along the bottom of the duct shows an immediate drop in static pressure followed by a rise in static pressure around x/L=0.07. This drop in static pressure indicates an acceleration of the flow, while the rise in static pressure signifies a strong adverse pressure gradient. This behavior indicates the flow response to the first turn of the duct. During the first turn, the bottom of the duct is the inside of the turn or the region where low momentum fluid exists. Since the profile indicates a constant presence of adverse pressure gradients in this region, the flow is assumed to remain attached. It will be shown later that the flow vortices from the first turn form in the corners of the cross-section; therefore, the flow should remain attached along the center of the bottom of the duct where the static pressure measurements are taken. Near x/L=0.16, the static pressure ratio returns to its value prior to the first turn indicating that the flow has recovered from the first turn. The adverse pressure gradient along the bottom of the duct continues until x/L=0.38 where the static pressure ratio levels off somewhat. This is in the region of the second turn where the bottom of the duct is on the outside or pressure side of the turn.

Following the second turn, the profiles for the baseline and flow control cases diverge but follow the same trend. The flow accelerates once more along the bottom of the wall until x/L=0.92 where another adverse pressure gradient begins. This adverse pressure gradient is due to the final turn in the duct and is not as extensive as the adverse pressure gradient due to the first turn because the third turn is not as sharp as the first two turns in the duct. The flow control case yields a higher static pressure while following the same trend as the uncontrolled case. This can be explained by the addition of mass flow at the top of the duct just prior to the divergence of the two profiles along the bottom of the duct at x/L=0.68.

The wall static pressure measurements agree with the flow development predictions presented in Chapter 2. For a more detailed description of the flow within the inlet duct, different measurements would be required. This work is focused on the challenge of inlet and engine integration; therefore, the focus is on the flow field at the AIP.

5.4. Aerodynamic Interface Plane Data

All of the experimental data were collected for a throat Mach number of 0.55. The flow control cases represent air injection through the microjets at 1% of the inlet mass flow rate. The total pressure ratio is given as the measured total pressure at a point normalized by the ambient total pressure. In this section the distortion descriptors outlined earlier will be presented in addition to the area-averaged total pressure recovery. Detailed total pressure recovery measurements will also be shown.

5.4.1. Cruise Condition

Figure 5.4 shows the data for the cruise condition case without flow control. For the total pressure contour, total pressure ratio is displayed by color variation with red indicating a high total pressure loss (15%) and blue representing minimal loss in total pressure (<1%). The total pressure contour for cruise condition without flow control is characterized by a large, circular total pressure deficit at the top center of Figure 5.4a. There are also regions of total pressure loss along the sides in two elliptical regions in a fairly symmetric distribution. The top central region is a result of the second bend in the duct while the two elliptical side regions originate from the corner regions of the first turn.

Also shown in Figure 5.4b-e are graphical depictions of the distortion parameters. The cruise condition case without flow control is characterized by circumferential distortion with the highest intensity in the hub region (Figure 5.4b). Again, the circumferential intensity is not a measure of total pressure deficit, but rather a measure of lower than average total pressure area over the extent of the low total pressure area. If the whole ring were to have low total pressure, this would result in a lower distortion. Therefore, it is also important to point out the area-averaged total pressure recovery. The parameter PR_{avg} is a measure of the total pressure losses in the duct while the circumferential distortion is a measure of the distribution of the losses. In the cruise condition case without flow control, the total pressure recovery is 95.6%. The circumferential extent of distortion is ~150 degrees for the cruise condition case without flow control (Figure 5.4c). Because the distortion occurs in one large block, the multiple per revolution content is 1 for each ring (Figure 5.4d). The radial distortion occurs

primarily in rings two and three (Figure 5.4e). This is a direct result of the large total pressure loss in the top center region (shown in yellow and red).

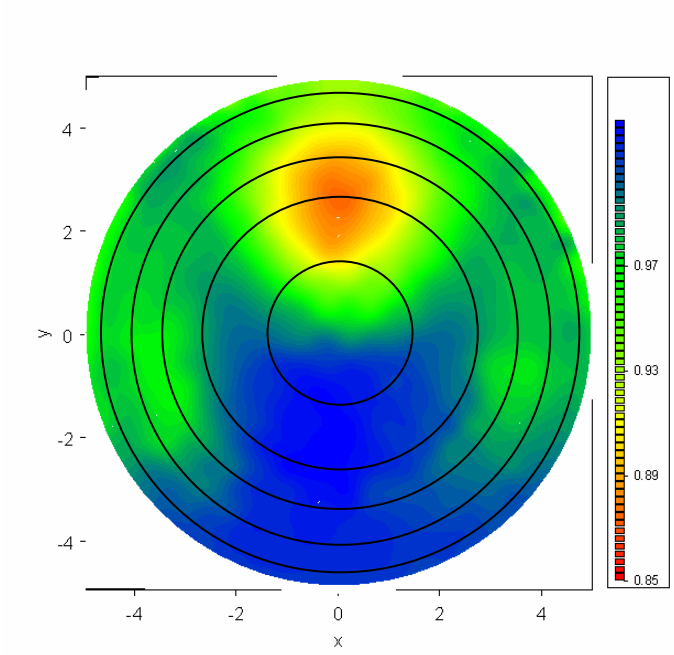

a) AIP Total Pressure Contour

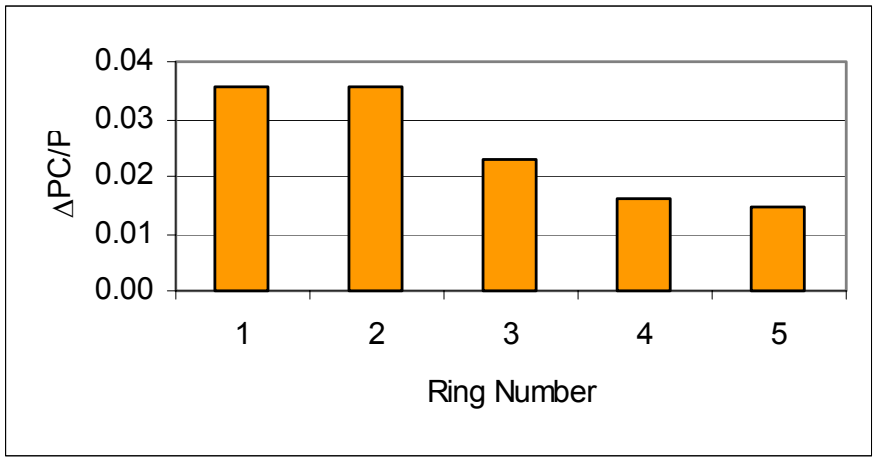

b) Circumferential Distortion

Figure 5.4 Cruise Condition Case without Flow Control - Total Pressure Contour and Distortion Descriptors

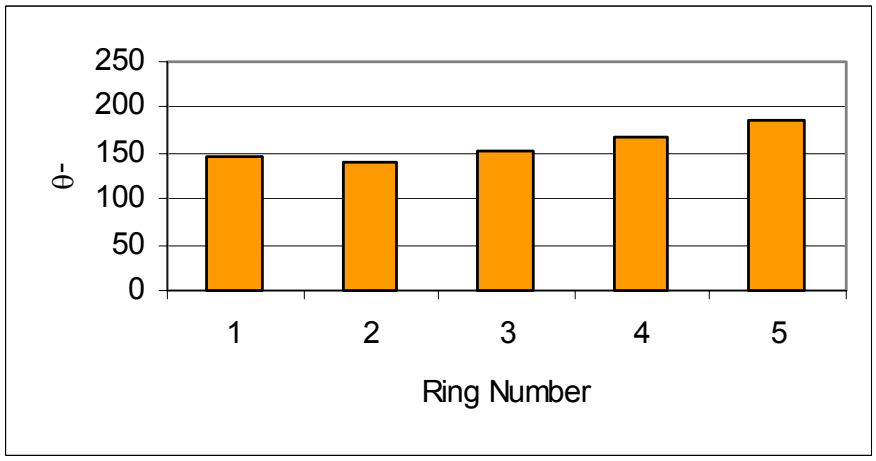

c) Extent of Circumferential Distortion

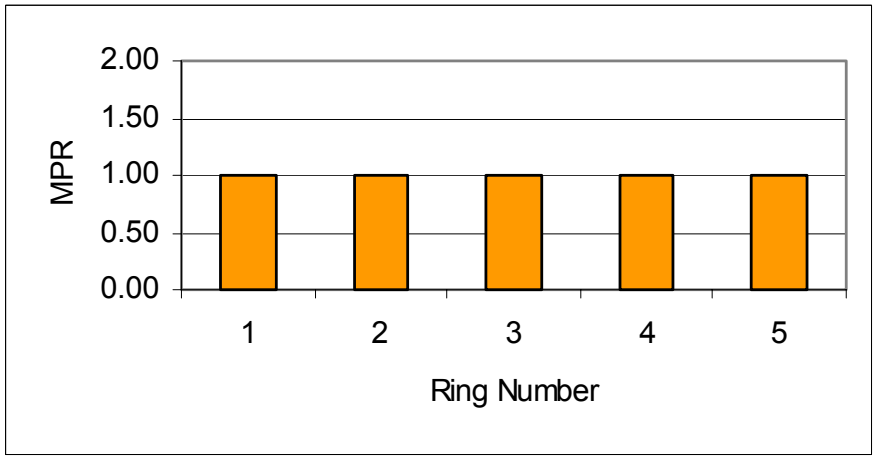

d) Multiple Per Revolution Distortion Descriptor

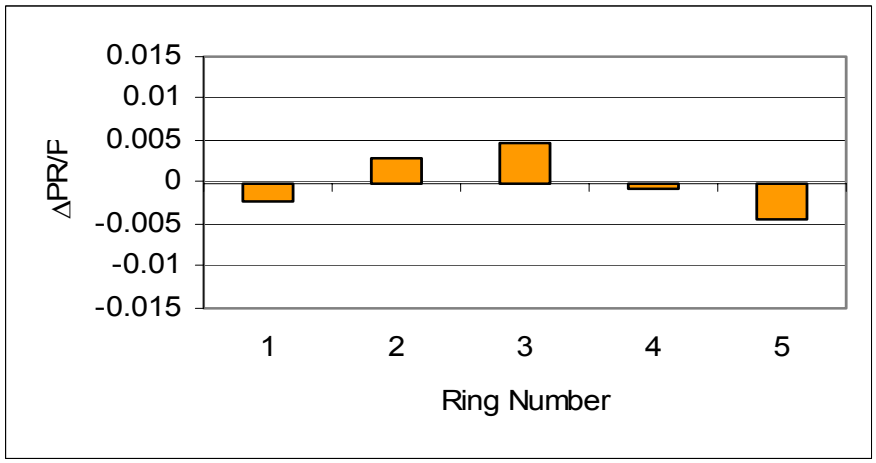

e) Radial Distortion Descriptor

Figure 5.4 Cruise Condition Case without Flow Control - Total Pressure Contour and Distortion Descriptors

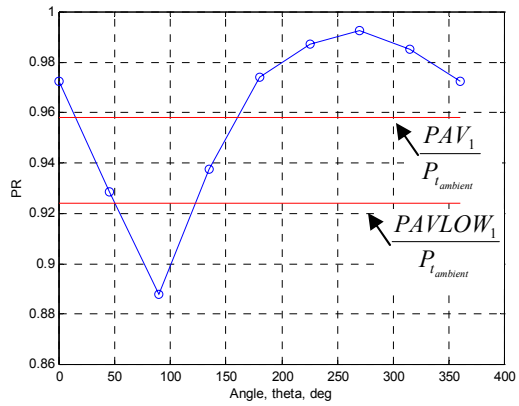

a) Ring 1

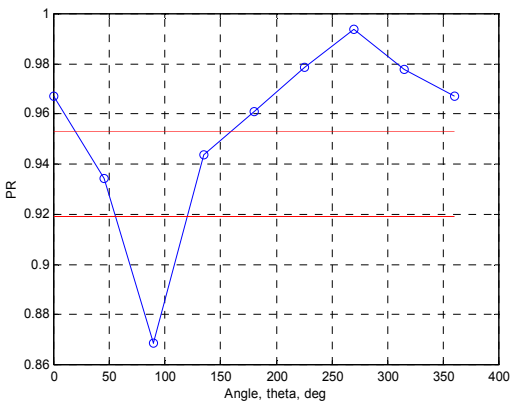

b) Ring 2

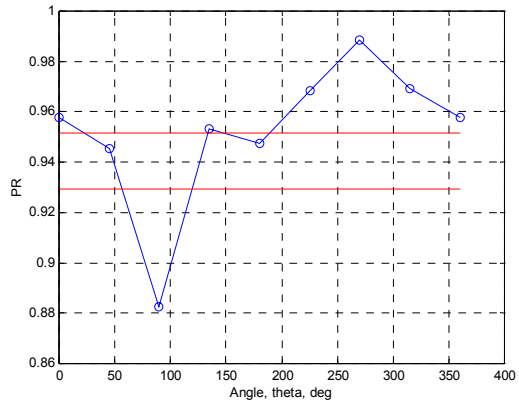

c) Ring 3

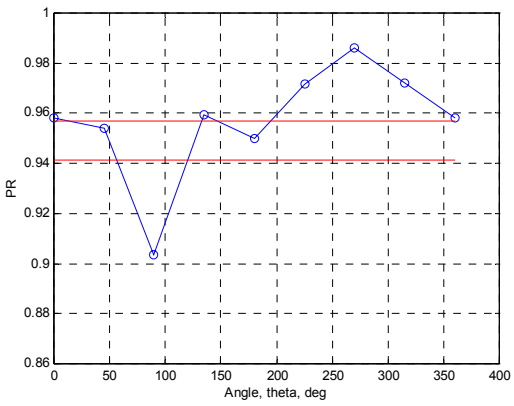

d) Ring 4

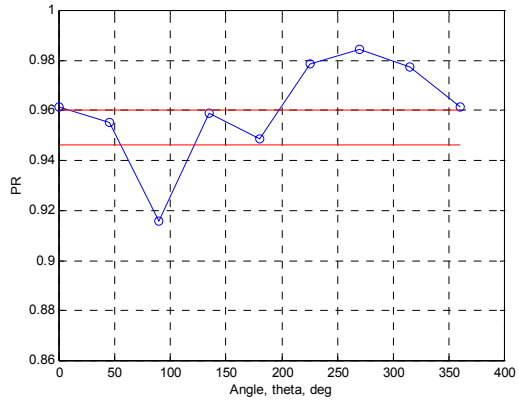

e) Ring 5

Figure 5.5 Cruise Condition Case without Flow Control – Total Pressure Recovery by Ring

Figure 5.5 shows the plots for the individual rings of total pressure ratio versus circumferential position. Also denoted on the plots are the ring average pressure

recovery (PAV), the upper red line, and the average low total pressure (PAVLOW), the lower red line. The low total pressure region is the area of the plot that lies below the average total pressure line and above the total pressure line. This is the region that determines the circumferential extent and distortion. In this case, each ring demonstrates a multiple per revolution value of one indicating there is only one region of low total pressure recovery. Rings three and four show a slight region of above average total pressure within the low total pressure region. This region of above average total pressure does not exceed the critical angle for the rotor considered in this test; therefore, the fan blades will not respond to the higher than average total pressure in this region. The extent of this region is so small that the time constant required for it to affect the fan blades is not realized; and during the regions of low total pressure, the fan blades will respond to one region of low total pressure.

Figure 5.6 shows the cruise condition case with flow control. The area-averaged pressure recovery increased to 97.5%. Examining the total pressure contour plot, the large total pressure deficiency in the top center has been dissipated (Figure 5.6a). In the cruise condition case with flow control, the total pressure deficiencies were limited to the two side regions with some additional distortion near the wall within 15-30 degrees on either side of top center. The intensity of the circumferential distortion has been reduced by ~75% at the hub rings and by ~35% at the tip (Figure 5.6b). The extent of the circumferential distortion has decreased by about 50 degrees (Figure 5.6c), and there is now multiple per revolution content ranging from 1.5 at the hub to 2 at the tip (Figure 5.6d). This indicates that the fan blades will respond to two different low pressure regions each revolution. The increase in MPR comes as a tradeoff with the overall

circumferential distortion intensity reduction of ~65%. The radial distortion is now tip radial distortion (Figure 5.6e). This is another indication of the low pressure regions near the wall.

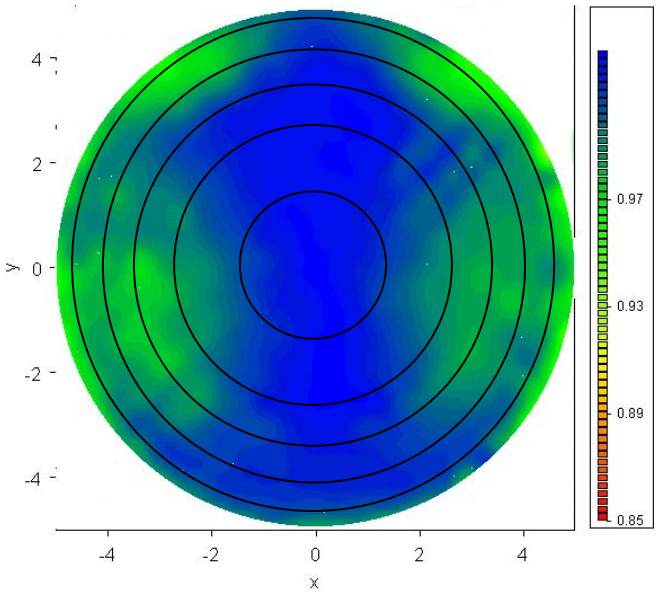

a) AIP Total Pressure Contour

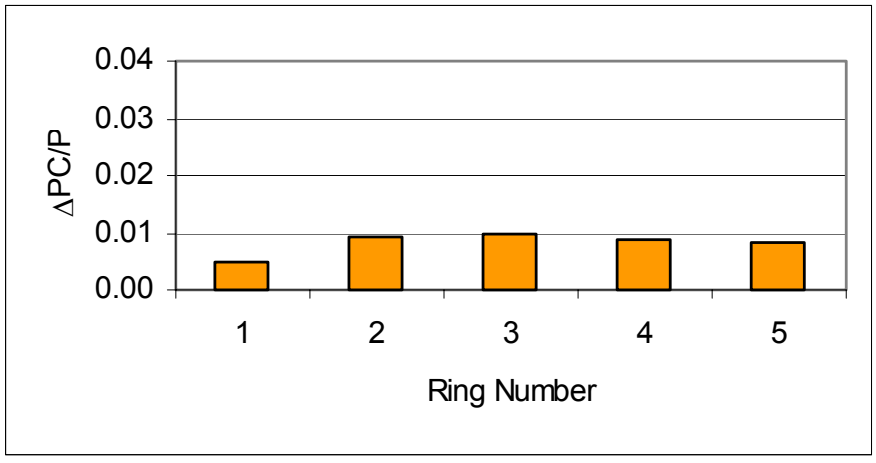

b) Circumferential Distortion

Figure 5.6 Cruise Condition Case with Flow Control – Total Pressure Contour and Distortion Descriptors

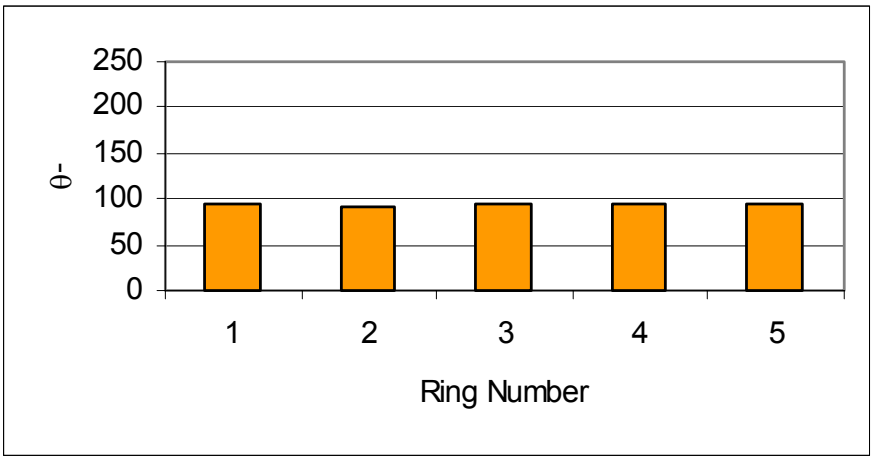

c) Extent of Circumferential Distortion

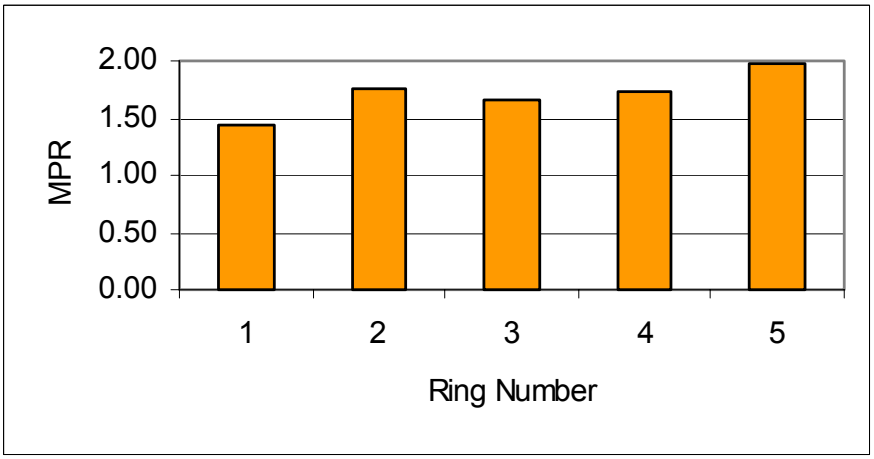

d) Multiple Per Revolution Distortion Descriptor

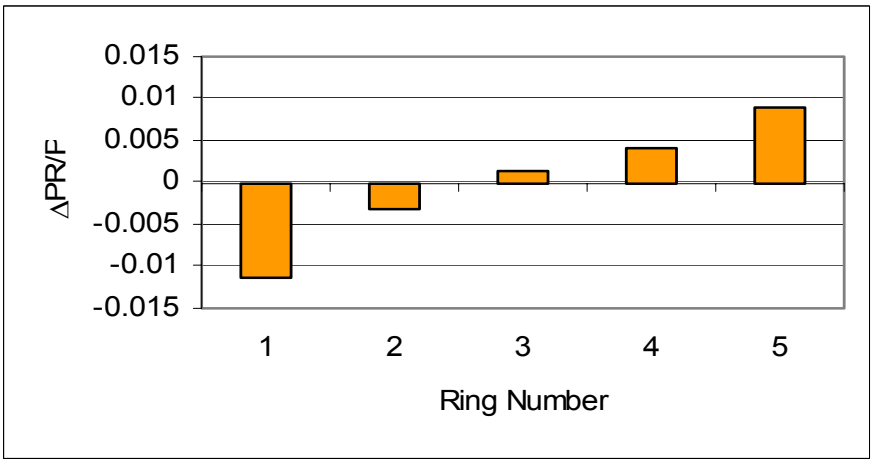

e) Radial Distortion Descriptor

Figure 5.6 Cruise Condition Case with Flow Control – Total Pressure Contour and Distortion Descriptors

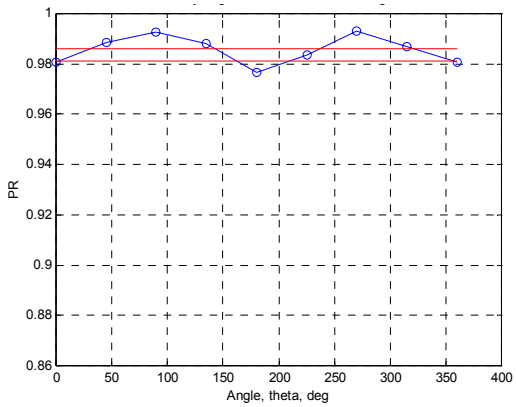

a) Ring 1

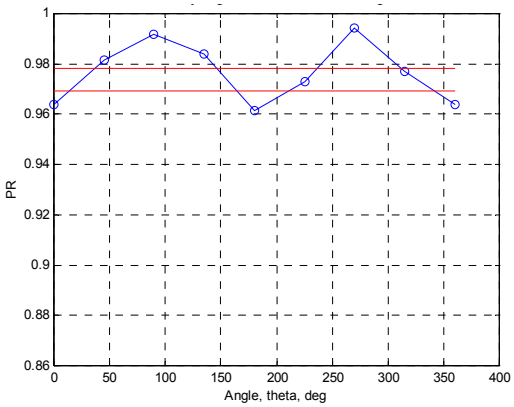

b) Ring 2

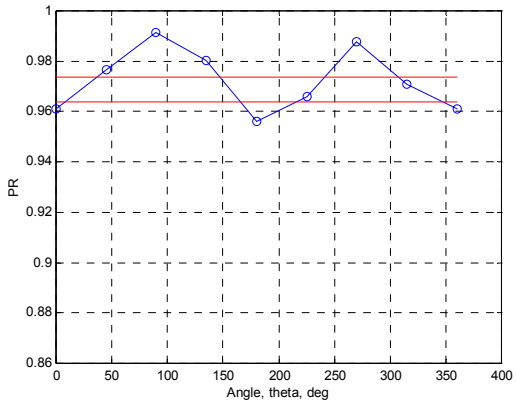

c) Ring 3

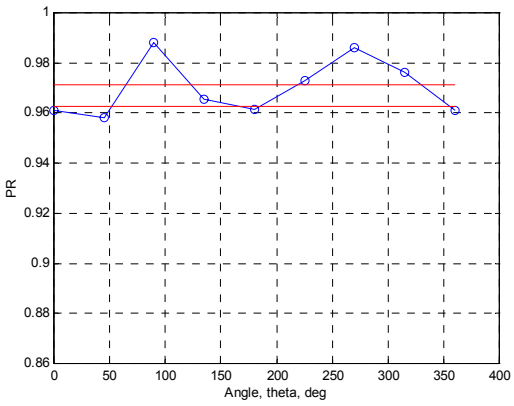

d) Ring 4

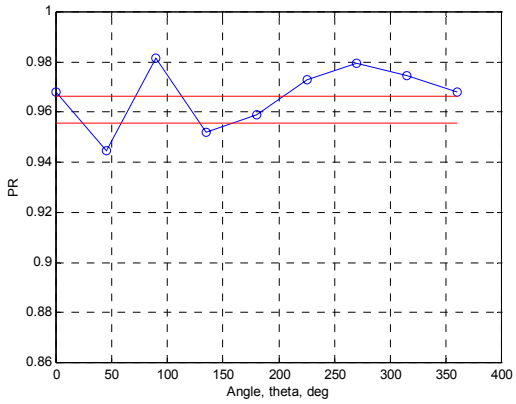

e) Ring 5

Figure 5.7 Cruise Condition Case with Flow Control – Total Pressure Recovery by Ring

Figure 5.7 shows the plots of total pressure recovery versus circumferential position of the individual rings for the cruise condition case with flow control. The upper red line is the ring average total pressure recovery (PAV), while the lower red line is PAVLOW. This case shows two regions of low total pressure for each ring, with enough high pressure recovery in between for the fan blades to respond to the high pressure region. Therefore, the fan blades now travel through 1.5 – 2 regions of low total pressure each revolution. The scale in these graphs is identical to that for the cruise condition case without flow control, so the level of increased total pressure ratio can be seen in the difference of the data range in the two sets of plots. For instance, ring one demonstrates almost uniform total pressure ratio around the circumference of the ring. All of the rings show a smaller amplitude range than the same plots for the uncontrolled case.

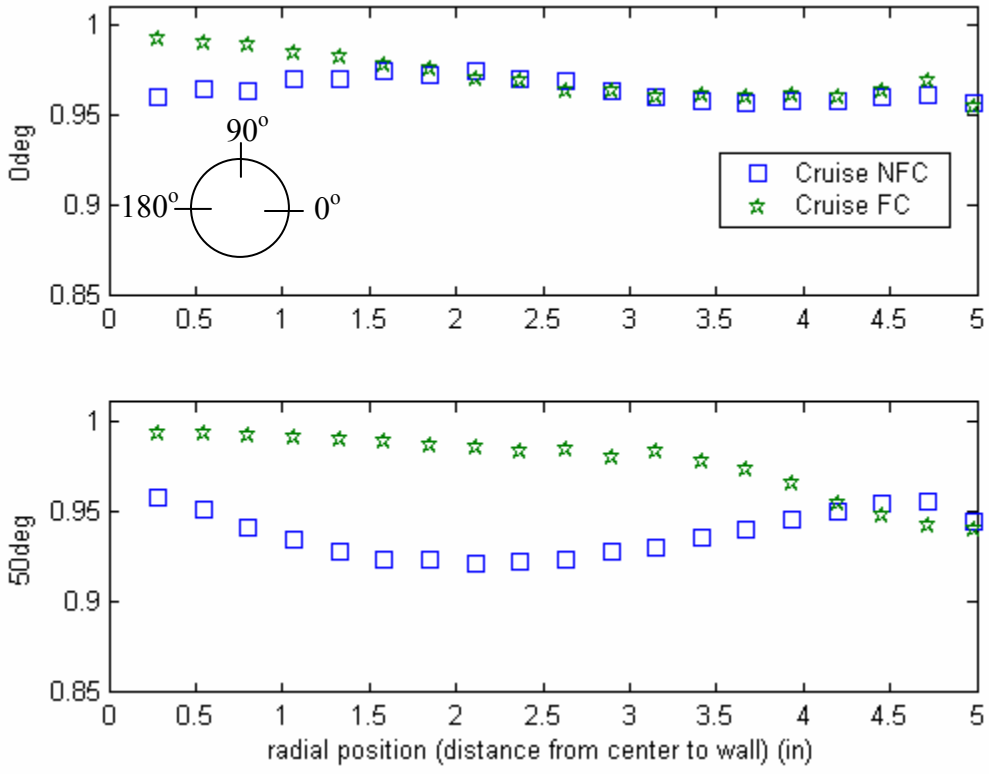

Figure 5.8 Cruise Condition Total Pressure Ratio Variation with Flow Control

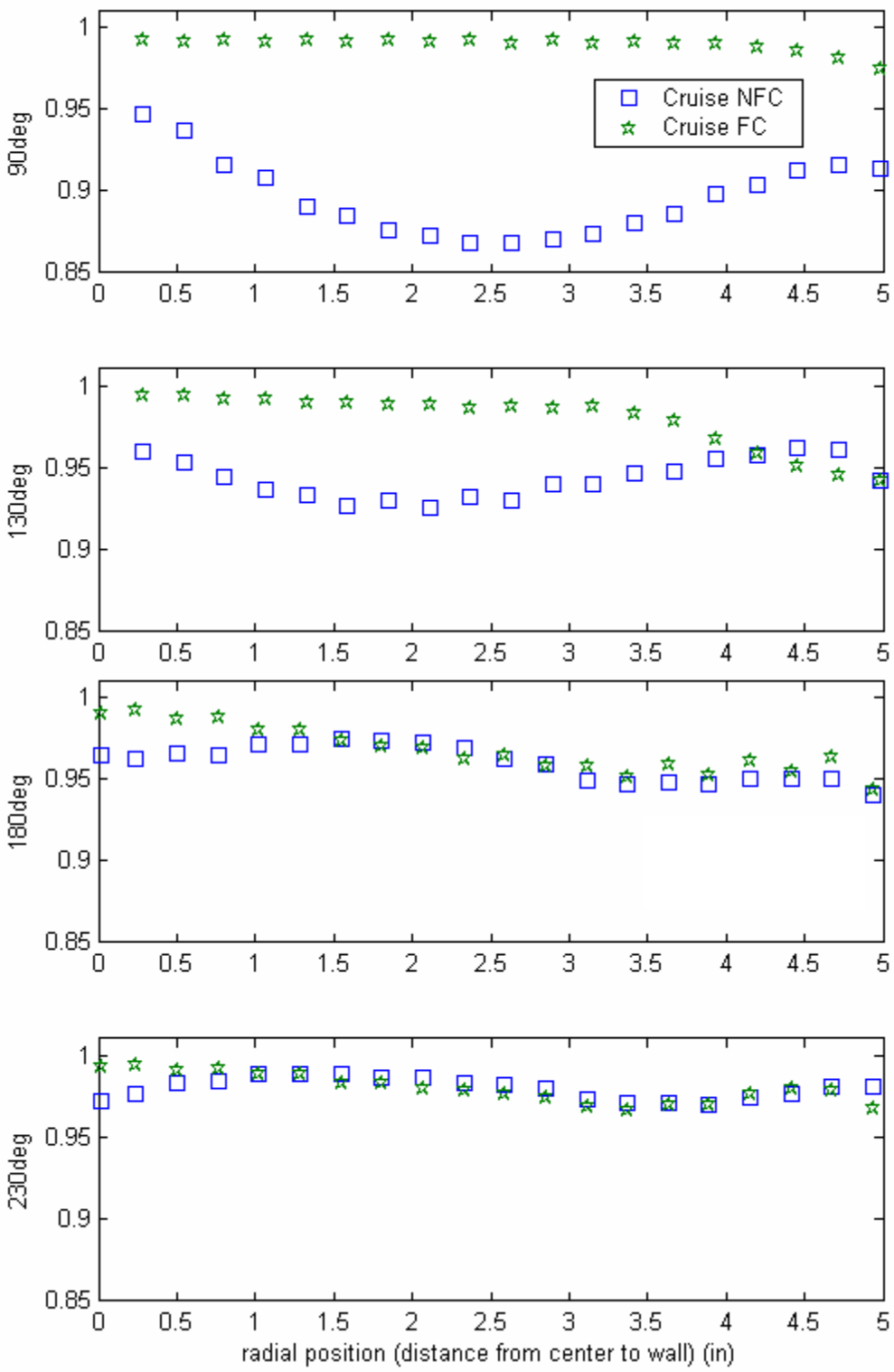

Figure 5.8 Cruise Condition Total Pressure Ratio Variation with Flow Control

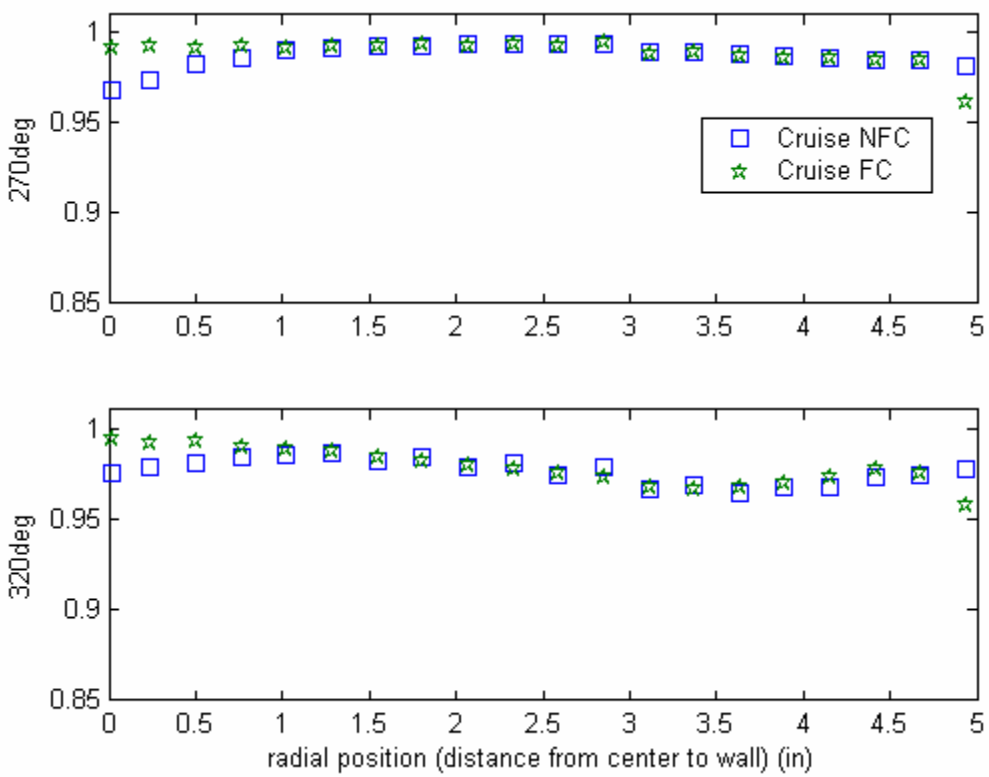

Figure 5.8 Cruise Condition Total Pressure Ratio Variation with Flow Control

The data points for the cruise condition cases with and without flow control are shown in Figure 5.8 for several circumferential locations. The circumferential positions are oriented so that 90 degrees is the top center of the total pressure contour plots from a forward position, looking aft. The zero degree position shows that the pressure recovery changes only in the central core region with the addition of flow control. At 50 degrees, the case without flow control shows significantly lower total pressure recovery than the flow control case with the exception of the last two data points in the tip region. This further illustrates the creation of tip radial distortion with the addition of flow control for the cruise condition case. The top central region, which is the most affected by the flow control, is shown in the 90 degree profile. As expected, the total pressure recovery is dramatically improved with the addition of flow control. Due to symmetry, the 130 and

180 degree profiles are similar to the 50 and 0 degree profiles, respectively. The pressure recovery profiles at 230, 270 and 320 degrees are all similar showing slightly higher pressure recovery in the central core region with the addition of flow control, but no effect over most of the radial range. There is a slight decrease in total pressure recovery in the tip region again illustrating the formation of tip radial distortion for the cruise condition case with flow control.

The harmonic content has been calculated for each of the experimental cases. The highest value of each n/rev harmonic coefficient over the five rings is presented as the value for that case. This is the maximum over the area of the duct and represents the worst case of harmonic content in the fluid distribution seen by the fan stage. Figure 5.9 shows the effect of flow control on harmonic content for the cruise condition case. In the cruise condition case, the flow control is very effective in reducing the 1/rev and 2/rev harmonic content. The 3/rev harmonic content actually increases with flow control; however, the 3/rev content is less than ¼ the uncontrolled 1/rev content. Therefore, the flow control was effective, overall, for the cruise condition case in reducing the harmonic content. This will in turn reduce the potential for high cycle fatigue, relative to the same inlet duct without flow control, for any compression system coupled with this inlet duct.

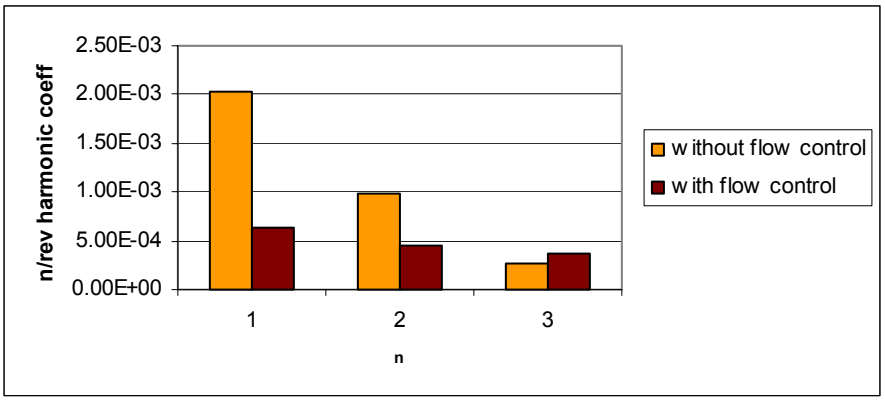

Figure 5.9 Effect of Flow Control on Harmonic Content for the Cruise Condition Case

5.4.2. Angle of Attack

Figure 5.10 shows the data for the simulated angle of attack without flow control. The area-averaged pressure recovery is only 94.2%. By comparing the total pressure contours without flow control for the angle of attack case (Figure 5.10a) and the cruise condition case (Figure 5.4a), the angle of attack case shows a greater overall region of total pressure loss. The side regions no longer appear as separate losses, apart from the central loss region. In fact, the side regions of distortion are large enough in this case to blend together with the central total pressure loss region. This is due to the angle of attack effect which accentuates the total pressure loss due to the first turn, increasing the area of the side elliptical regions of total pressure loss at the AIP. Looking at the circumferential distortion intensity (Figure 5.10b), the angle of attack case without flow control actually has lower hub distortion, but increased tip distortion, as compared to the cruise condition case without flow control. This is due to the location of the increased total pressure losses as shown in the total pressure contour map in Figure 5.10a. The circumferential extent of the distortion (Figure 5.10c) is actually higher than for either of the cruise condition cases. As with the cruise condition case without flow control, the

multiple per revolution content (Figure 5.10d) is one and the radial distortion (Figure 5.10e) is concentrated in rings two and three. This is again due to the large circular total pressure deficit at top center.

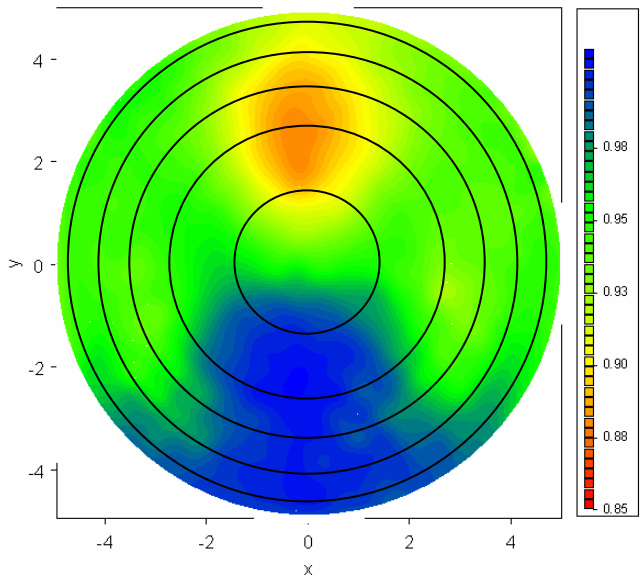

a) AIP Total Pressure Contour

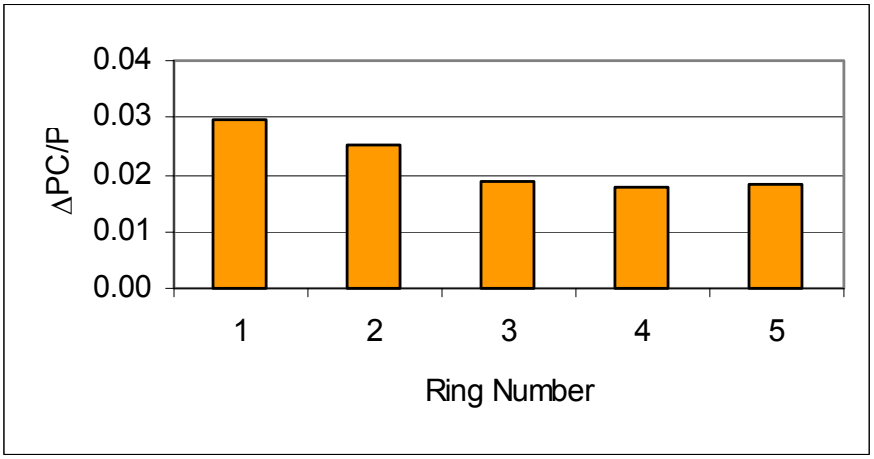

b) Circumferential Distortion

Figure 5.10 Angle of Attack without Flow Control – Total Pressure Contours and Distortion Descriptors

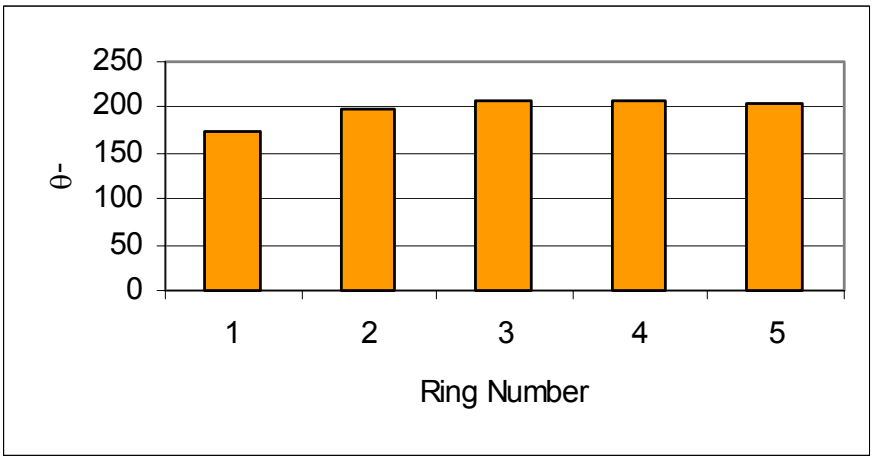

c) Extent of Circumferential Distortion

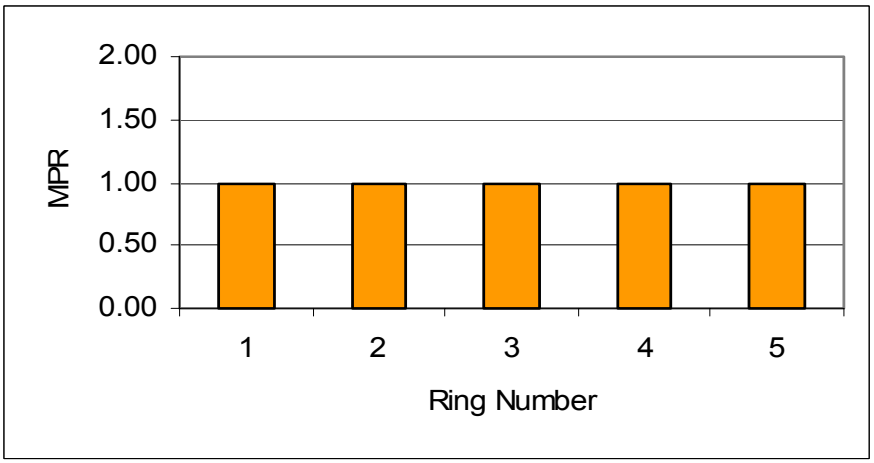

d) Multiple Per Revolution Distortion Descriptor

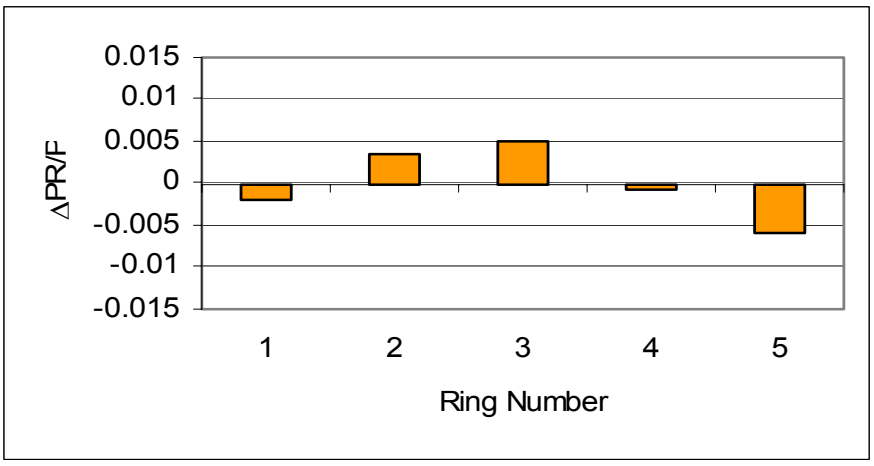

e) Radial Distortion Descriptor

Figure 5.10 Angle of Attack without Flow Control – Total Pressure Contours and Distortion Descriptors

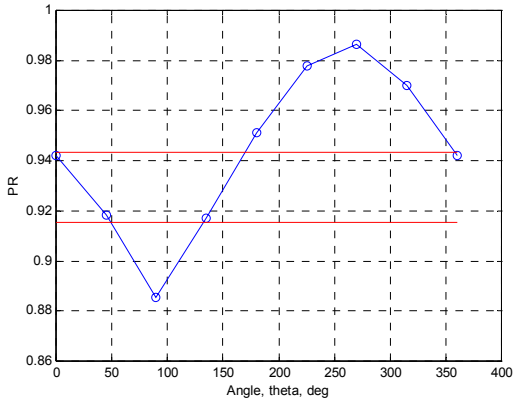

a) Ring 1

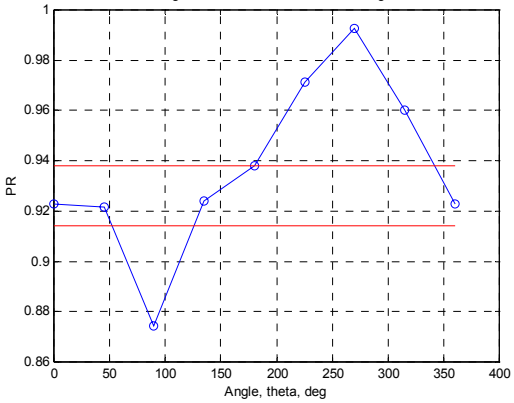

b) Ring 2

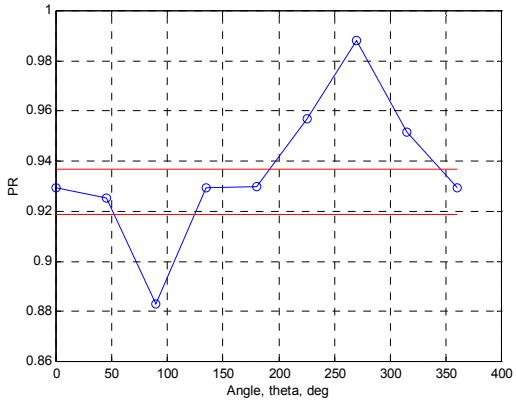

c) Ring 3

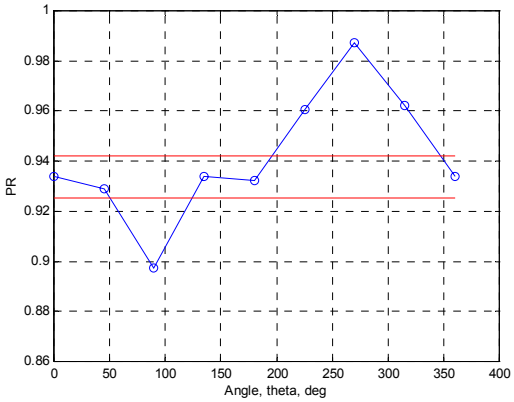

d) Ring 4

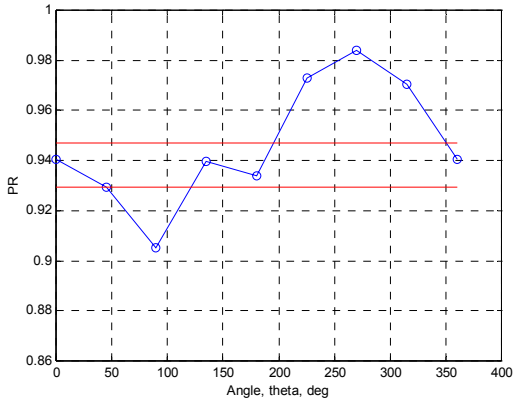

e) Ring 5

Figure 5.11 Angle of Attack without Flow Control – Total Pressure Recovery by Ring

Figure 5.11 shows the individual plots of total pressure recovery versus circumferential location for the angle of attack case without flow control. Similar to the cruise condition case, there is one region of low total pressure recovery. However, by comparing the two sets of graphs, it can be seen that the extent of the distortion is larger for the angle of attack case. This is another way of describing the additional flow distortion from the corner vortices out of the first turn of the duct. It is also important to notice that the additional distortion due to the corner vortices lowers the average total pressure recovery, changing what constitutes lower than average total pressure. Therefore, the circumferential distortion is actually decreasing. This is the trend mentioned earlier where, by having a lower average total pressure, the flow is more uniform, but with less pressure recovery. This reduces the distortion level, but there is still additional strain on the engine by providing less total pressure at the AIP.

The area-averaged total pressure recovery increases to 95.7% for the angle of attack case with the addition of flow control. The total pressure contour in Figure 5.12a shows that while the large region of total pressure distortion at the top center of the angle of attack case without flow control has been eliminated, the side regions of low total pressure are significantly larger (in both area and intensity) than in the cruise condition cases. The angle of attack condition intensifies the side regions of distortion which are due to the flow separation in the corners of the first turn in the duct. The flow control technique does not reduce these side regions of distortion, but leaves them untouched. The circumferential distortion intensity (Figure 5.12b) was still reduced in the angle of attack case through the use of flow control, but not as significantly as the cruise condition case. The extent of the circumferential distortion (Figure 5.12c) has been significantly

reduced to ~100 degrees for each ring. The multiple per revolution content (Figure 5.12d), as expected, increased to ~2 for the outer rings (3-5). Radial distortion for angle of attack with flow control (Figure 5.12e) is concentrated in rings two and three.

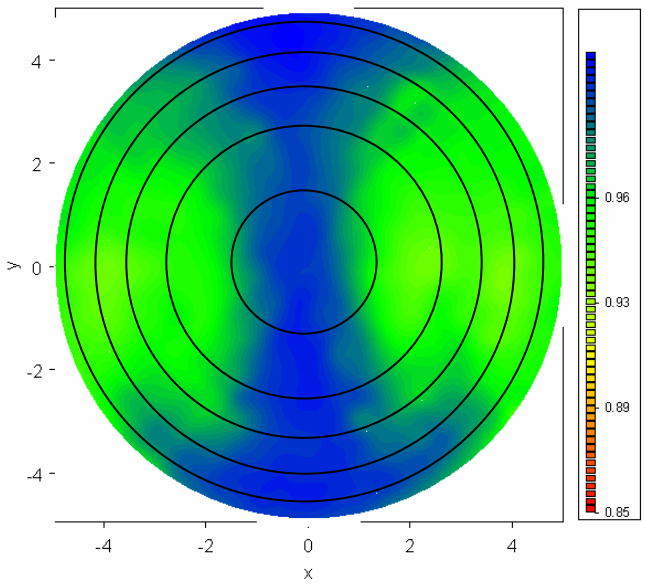

a) AIP Total Pressure Contour

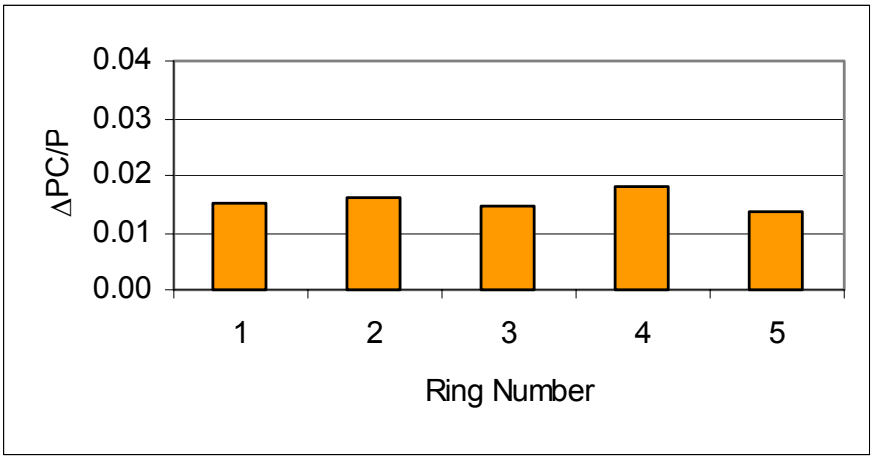

b) Circumferential Distortion

Figure 5.12 Angle of Attack with Flow Control – Total Pressure Contour and Distortion Descriptors

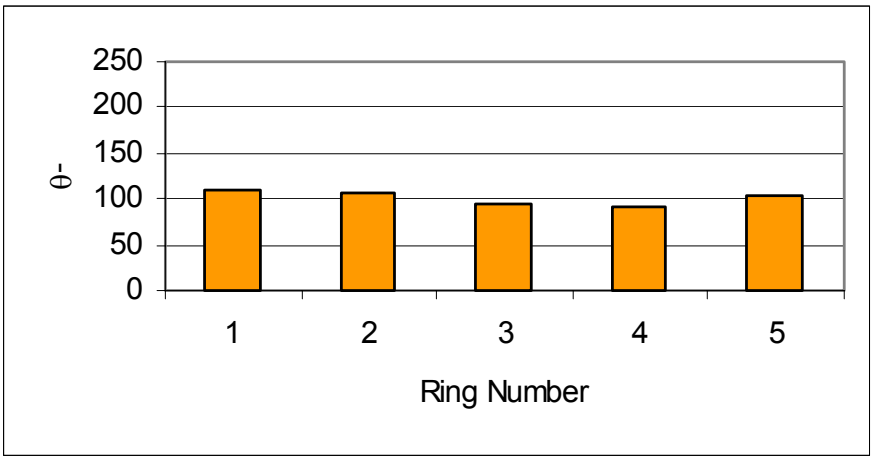

c) Extent of Circumferential Distortion

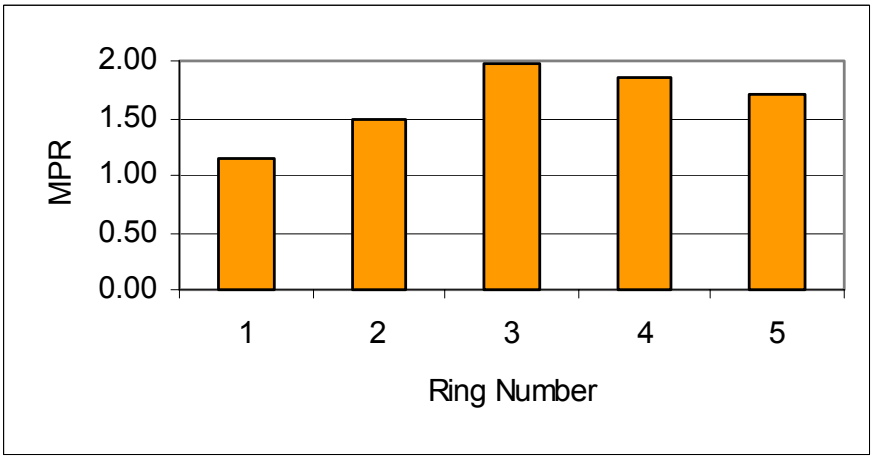

d) Multiple Per Revolution Distortion Descriptor

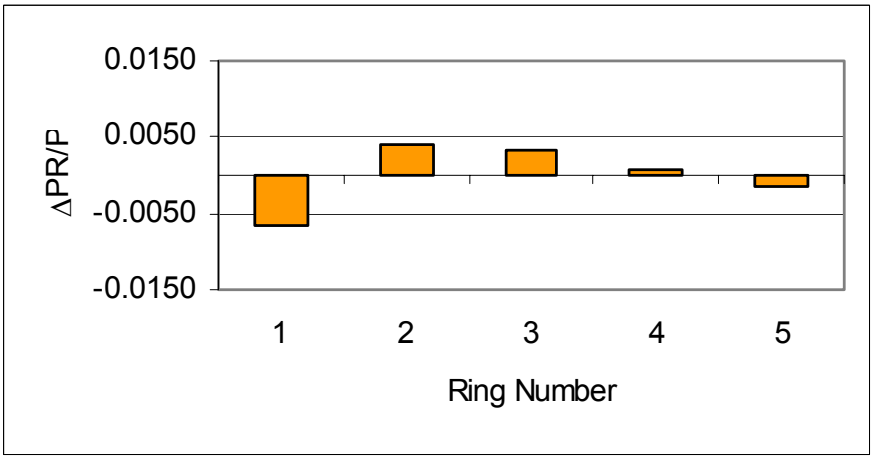

e) Radial Distortion Descriptor

Figure 5.12 Angle of Attack with Flow Control – Total Pressure Contour and Distortion Descriptors

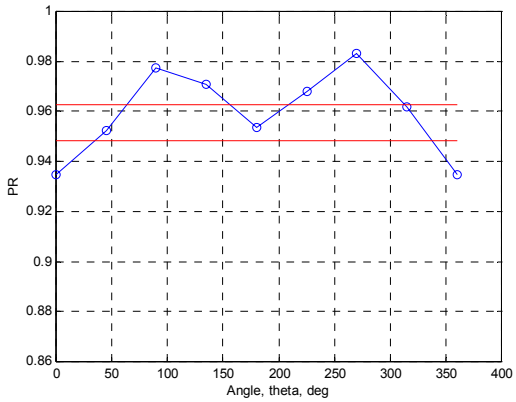

a) Ring 1

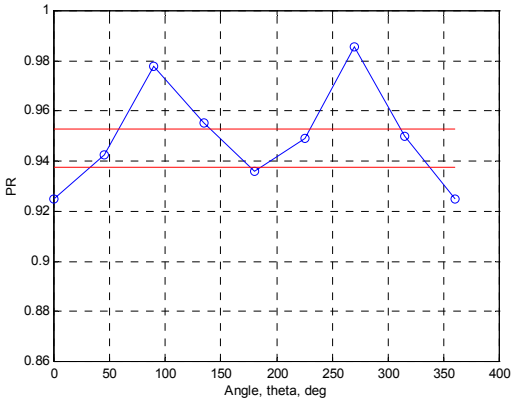

b) Ring 2

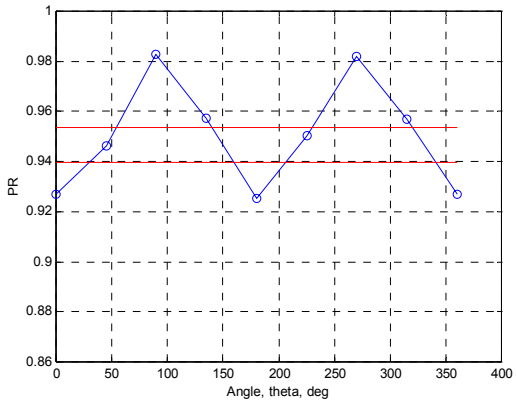

c) Ring 3

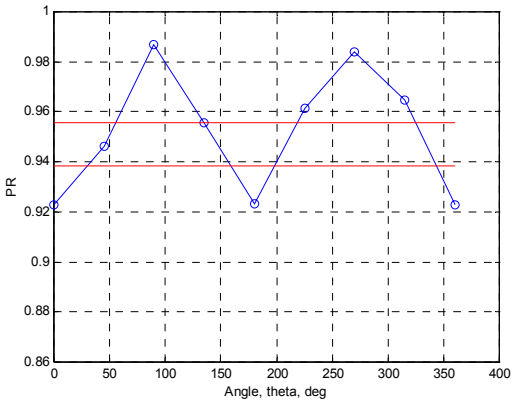

d) Ring 4

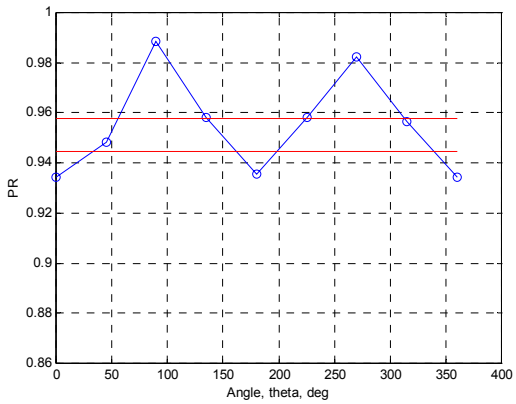

e) Ring 5

Figure 5.13 Angle of Attack with Flow Control – Total Pressure Recovery by Ring

The ring-by-ring plots for total pressure recovery versus circumferential position for the angle of attack case with flow control are shown in Figure 5.13. The plots show that the two low total pressure regions become equal in area at the outer rings while there is some asymmetry in the angle of attack data at the inner rings. The same overall trend is realized in the angle of attack case and the cruise condition case where the distortion is broken into two separate regions with the addition of flow control. By the tip rings these two regions are equal and produce an MPR of two. Comparing these plots to the respective plots for cruise condition, the increased pressure loss can be seen. This is another indication of the increased intensity of the corner vortices in the angle of attack case.

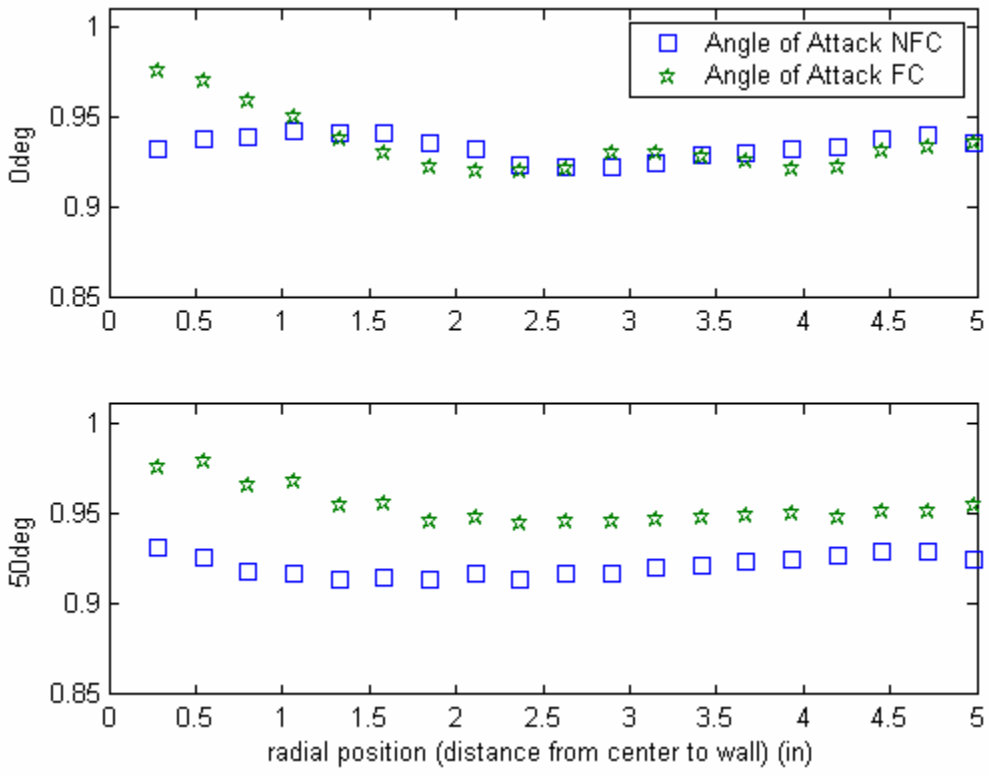

Figure 5.14 Angle of Attack Total Pressure Ratio Variation with Flow Control

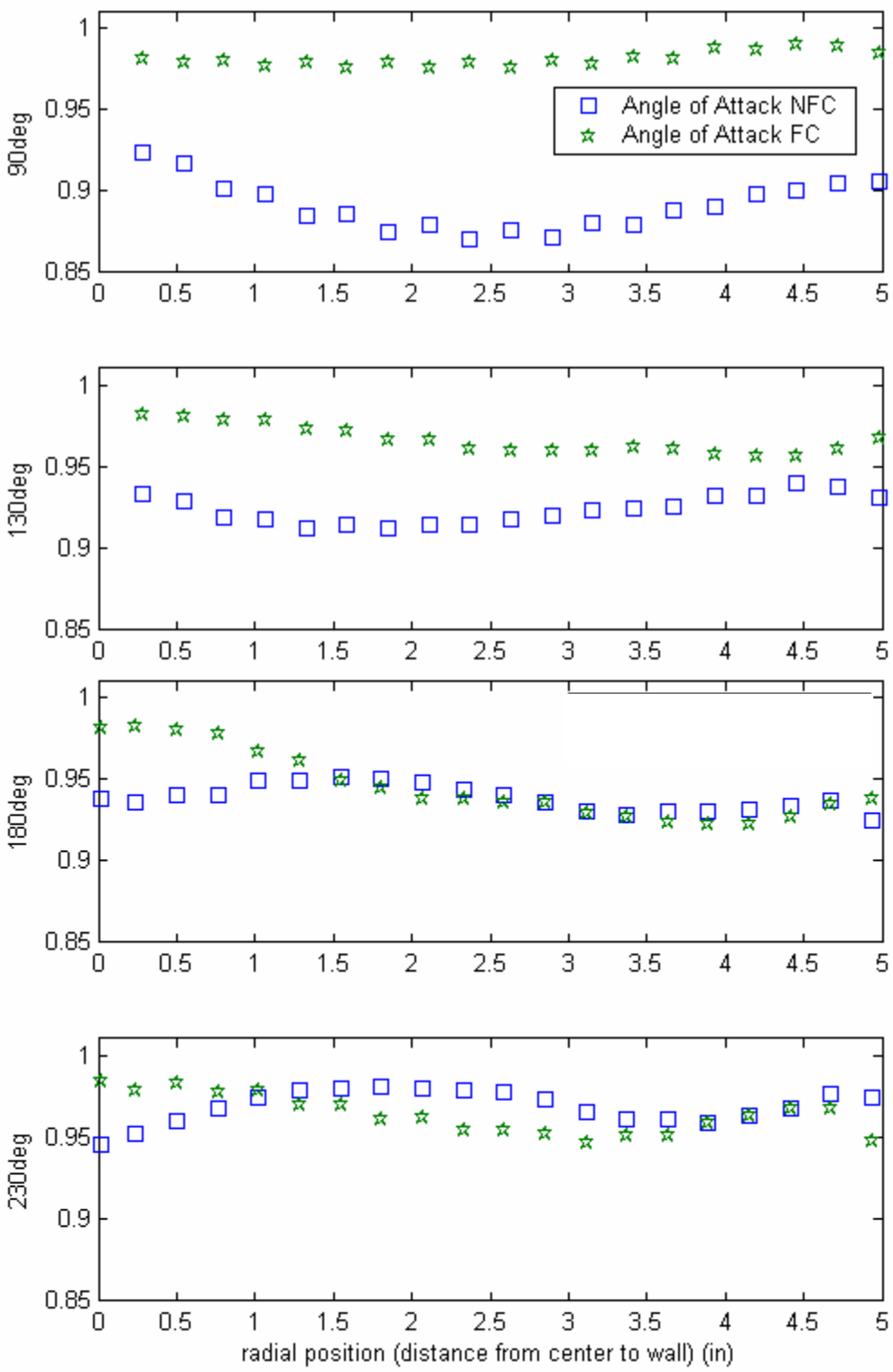

Figure 5.14 Angle of Attack Total Pressure Ratio Variation with Flow Control

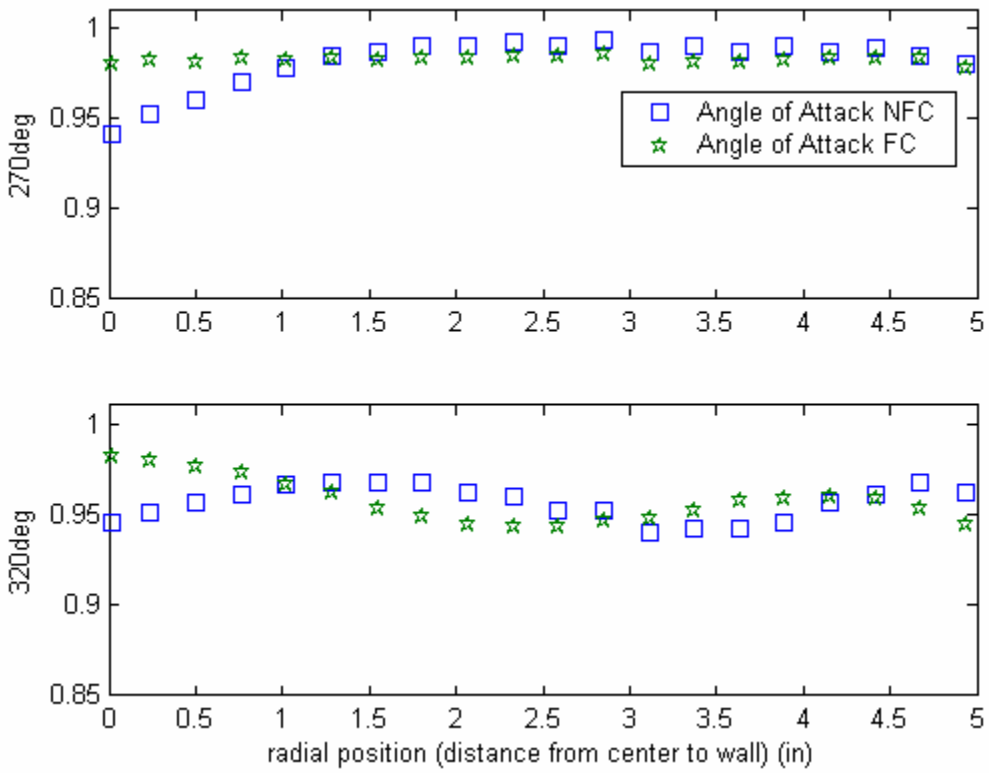

Figure 5.14 Angle of Attack Total Pressure Ratio Variation with Flow Control

Figure 5.14 shows the total pressure recovery radial data points for several circumferential locations. By examining several circumferential locations, the trends revealed in a comparison of the total pressure contours for the angle of attack condition with and without flow control are seen in more detail. At zero degrees, the flow control is effective in improving the total pressure recovery in the central core region. Moving away from the core, the angle of attack case without flow control shows better pressure recovery for a segment, followed by decreased pressure recovery (relative to the angle of attack case with flow control) and finally, improved pressure recovery in the tip region. This is due to the interference in the no flow control case between the two sets of vortices. This trend was not realized in the cruise condition case where the two sets of vortices are separate. Since in the angle of attack case the side vortices are significantly

enlarged from the cruise condition case, they are interacting with the top central vortices. In the uncontrolled case, the vortex pairs are able to cancel each other out to some degree where the vortices overlap. This causes higher pressure recovery for the no flow control case in these regions. With the addition of flow control, one set of vortices is removed, and the remaining pair is stronger because it is not opposed in any way. For the 50, 90 and 130 degree profiles, the flow control produces significantly higher total pressure recovery, as expected from the total pressure contours. The bottom half of the duct also exhibits the vortex canceling effect indicating that the effect is global. The profiles at 180, 230, 270 and 320 degrees exhibit behavior similar to that at 0 degrees.

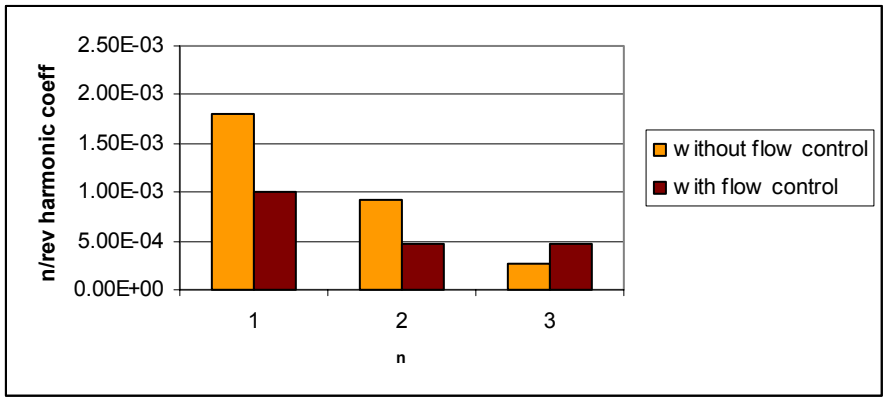

Figure 5.15 Effect of Flow Control on Harmonic Content for Angle of Attack Case

Figure 5.15 shows the change in harmonic content with flow control for the angle of attack case. The trend is similar to that shown in the cruise condition case. There is a reduction in the 1/rev and 2/rev harmonic content of ~40% with the introduction of flow control, while the 3/rev harmonic content increases by ~40% with the addition of flow control. Overall the harmonic content has been decreased with the addition of flow control, resulting in less potential for high cycle fatigue for a compression system coupled to this inlet duct.

5.4.3. Asymmetric Distortion

The data for the asymmetric distortion case without flow control are found in Figure 5.16. The area-averaged total pressure recovery is 94.4% which is marginally higher than the angle of attack case, but lower than the cruise condition case without flow control. The total pressure contour (Figure 5.16a) shows that while the top central distortion region is still present, the left side resembles that of the angle of attack case while the right side is more similar to the cruise condition case. The right side is more intense than the cruise condition case, while maintaining a distinction between the top central distortion block and the side region of distortion. The circumferential distortion intensity (Figure 5.16b) is similar to the other cases without flow control, stronger near the inner rings, with significant intensity in all rings. The extent of the circumferential distortion (Figure 5.16c) is between 150 and 200 degrees, again similar to the other cases without flow control. The multiple per revolution content is one (Figure 5.16d), as expected, and the radial distortion (Figure 5.16e) is concentrated in rings two and three as before.

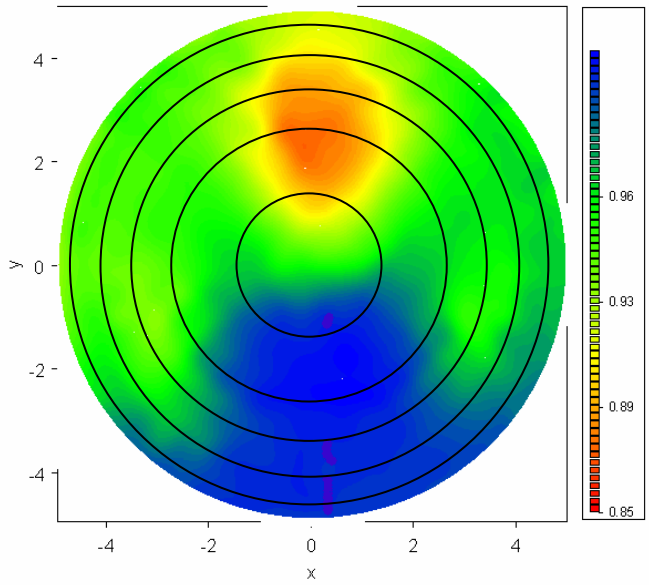

a) AIP Total Pressure Contour

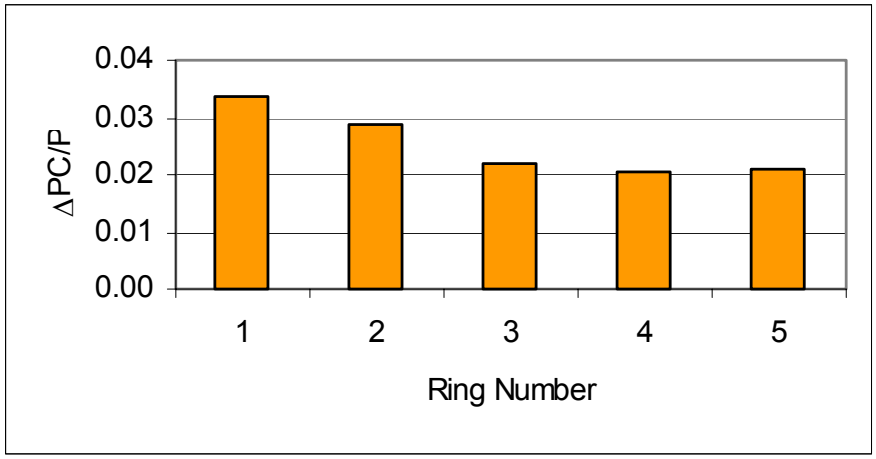

b) Circumferential Distortion

Figure 5.16 Asymmetric Distortion without Flow Control – Total Pressure Contour and Distortion Descriptors

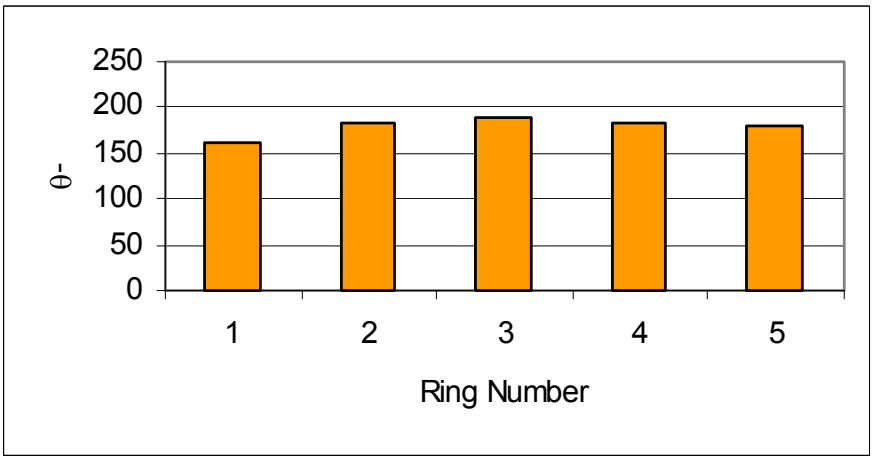

c) Extent of Circumferential Distortion

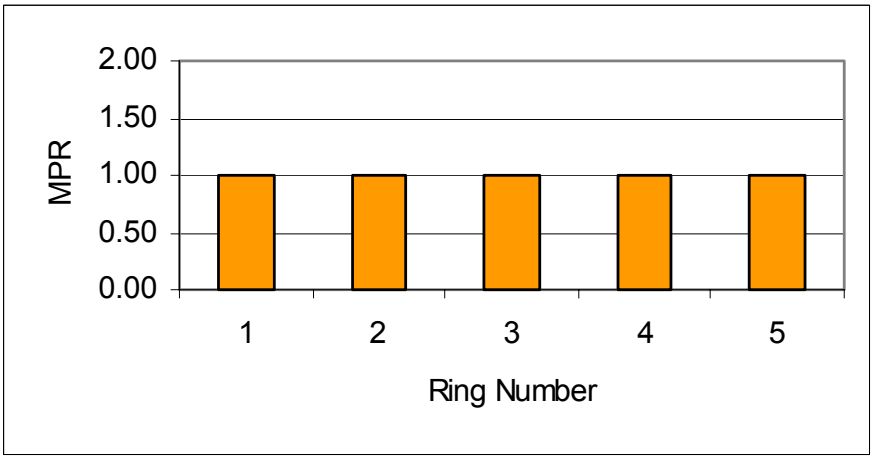

d) Multiple Per Revolution Distortion Descriptor

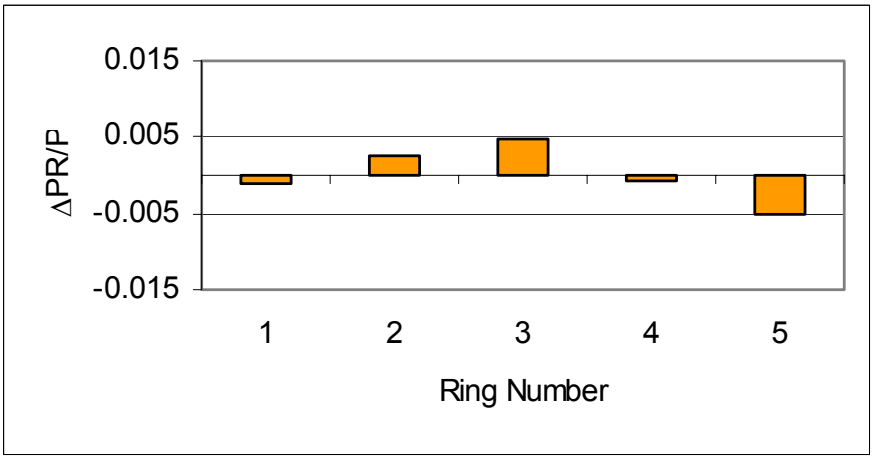

e) Radial Distortion Descriptor

Figure 5.16 Asymmetric Distortion without Flow Control – Total Pressure Contour and Distortion Descriptors

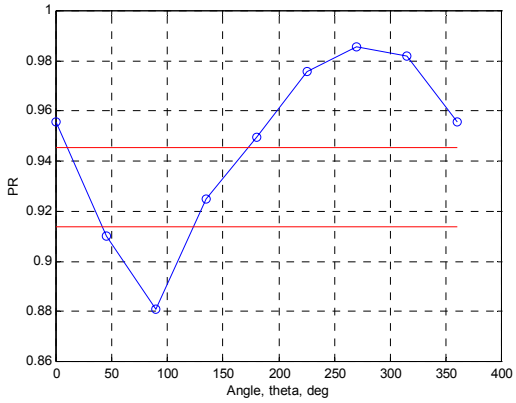

a) Ring 1

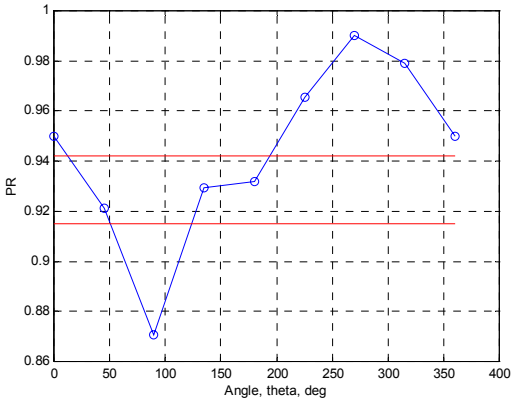

b) Ring 2

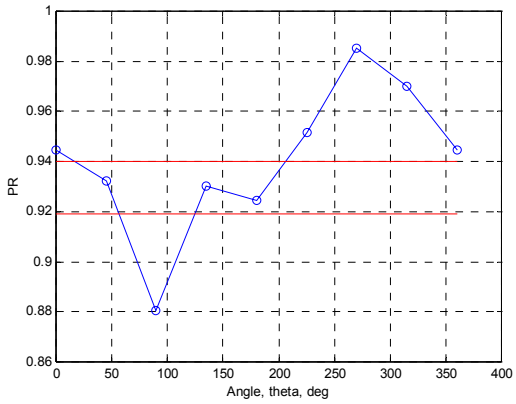

c) Ring 3

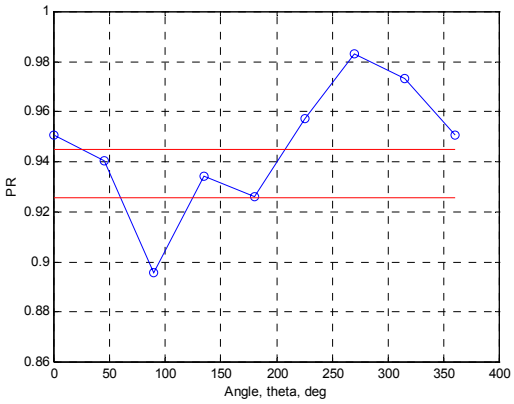

d) Ring 4

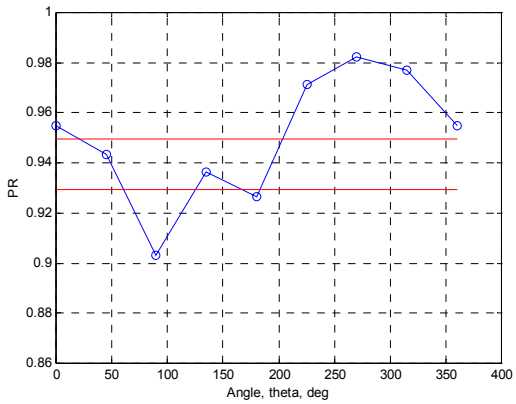

e) Ring 5

Figure 5.17 Asymmetric Distortion without Flow Control – Total Pressure Recovery by Ring

Figure 5.17 shows the individual plots of total pressure recovery versus circumferential position for the asymmetric distortion case without flow control. Similar to the other cases without flow control, the distortion is concentrated in one region of low total pressure. However, in the asymmetric distortion case, as expected, this distortion is not symmetric. The region from θ=90-200 degrees is more similar to the same region in the angle of attack case while the region from θ=25-90 is more similar to the cruise condition case. The region from ~135 to 200 degrees shows the angle of attack trend of increased extent with less pressure loss than the main distortion region. This represents the increased area of moderate total pressure loss due to the strengthened corner vortex.

The asymmetric distortion case with flow control produces an area-averaged total pressure recovery of 96.2%. The total pressure contour shown in Figure 5.18a demonstrates the same trends realized in the cruise condition and angle of attack cases with flow control. However, the asymmetric distortion data are not symmetric. The left hand side, where the distortion element was present, agrees well with the angle of attack case. The right hand side is somewhere in between the angle of attack case and the cruise condition case. The circumferential distortion intensity (Figure 5.18b) is concentrated more in ring four, but overall the distortion is more uniform than previous cases. The extent of the circumferential distortion (Figure 5.18c) is also unique among the experimental cases, ranging only from 100-120 degrees. The multiple per revolution content (Figure 5.18d) is only around 1.2, also differing from the other cases. The decrease in MPR is due to the difference in severity of the distortion on one side of the exit plane as compared to the other side of the exit plane. The radial distortion (Figure

5.18e), the only parameter to closely resemble previous cases, is higher in the middle three rings.

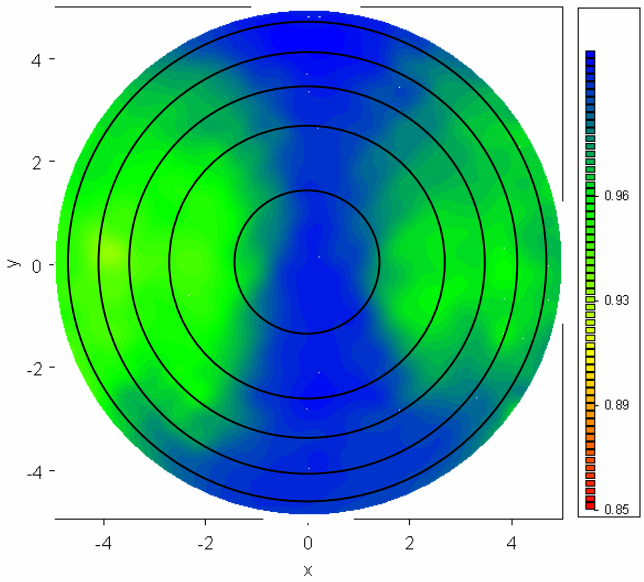

a) AIP Total Pressure Contour

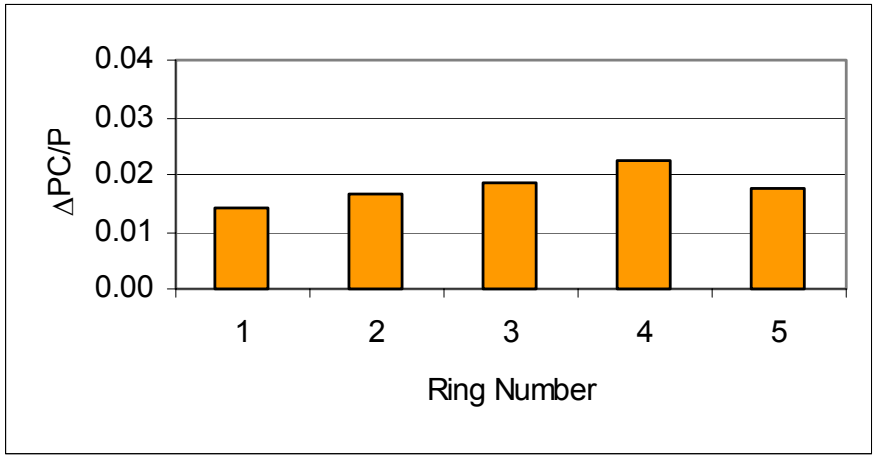

b) Circumferential Distortion

Figure 5.18 Asymmetric Distortion with Flow Control – Total Pressure Contours and Distortion Descriptors

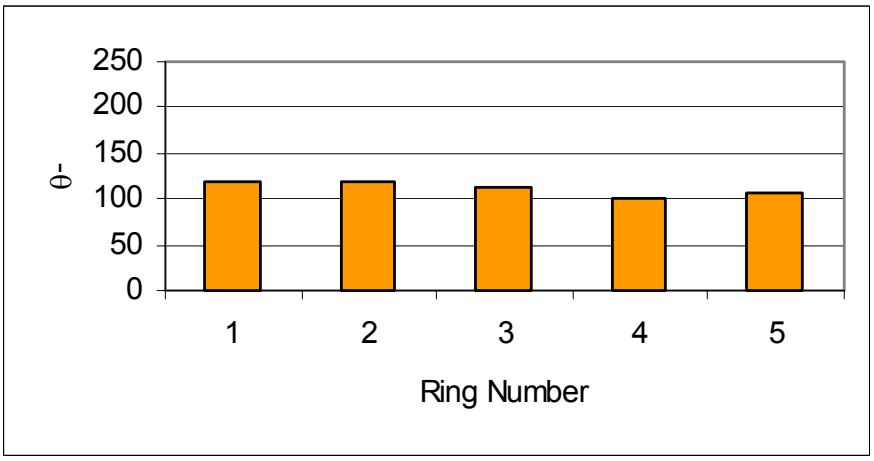

c) Extent of Circumferential Distortion

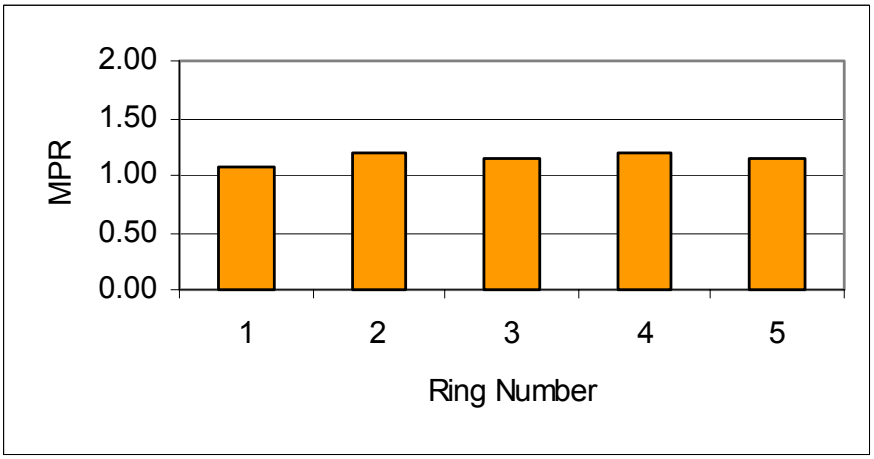

d) Multiple Per Revolution Distortion Descriptor

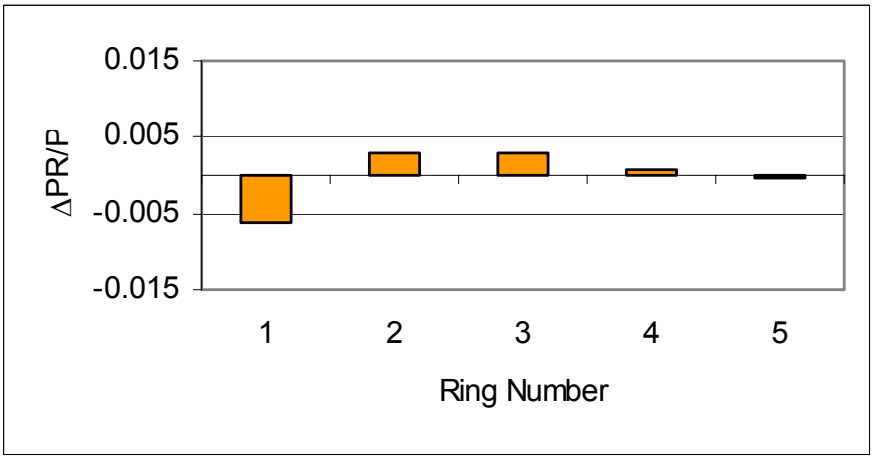

e) Radial Distortion Descriptor

Figure 5.18 Asymmetric Distortion with Flow Control – Total Pressure Contours and Distortion Descriptors

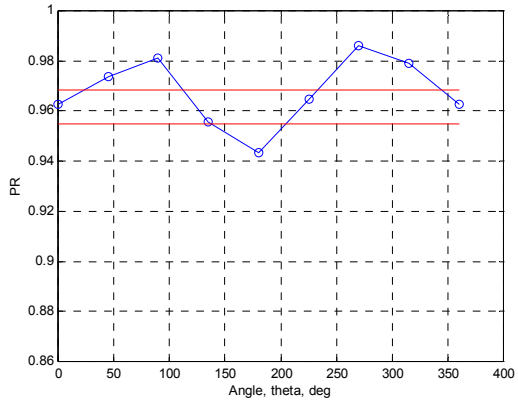

a) Ring 1

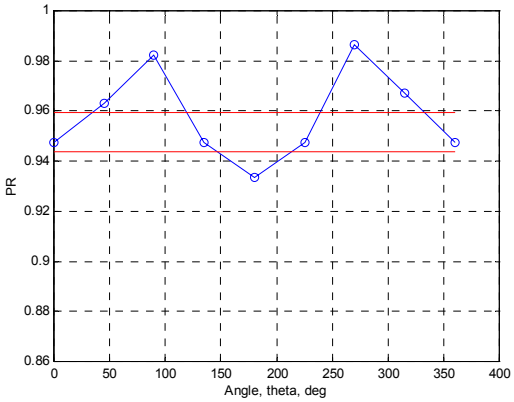

b) Ring 2

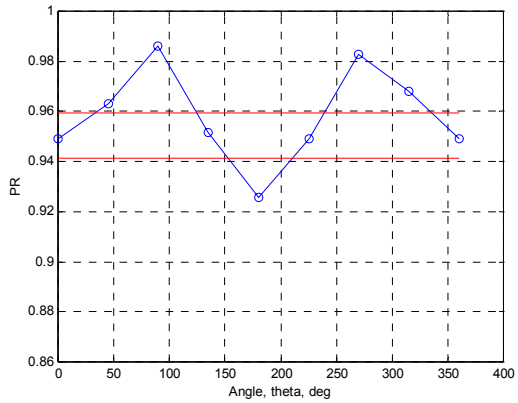

c) Ring 3

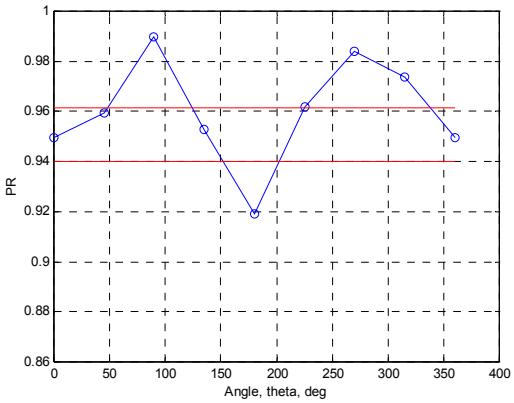

d) Ring 4

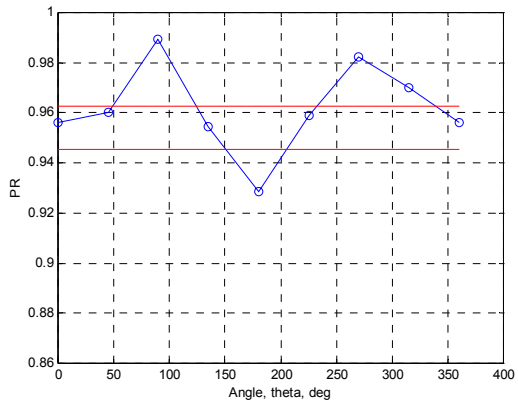

e) Ring 5

Figure 5.19 Asymmetric Distortion with Flow Control – Total Pressure Recovery by Ring

The plots showing the total pressure recovery versus circumferential location for the individual rings are shown in Figure 5.19 for the asymmetric distortion case with flow control. Once again, the asymmetry of the flow at the AIP can be seen. The distortion is now concentrated in the region of θ=125-225 degrees. The second region of low total pressure has a smaller area of low pressure leading to the smaller MPR values. As discussed earlier, MPR is weighted by area so that if there are two regions of low total pressure, and one has twice the area of the other, the MPR will be 1.5. In this case the smaller area is less than ¼ the value of the larger area. This results in the MPR values of 1.2 or less. Again, this is caused by the asymmetry of inlet flow in the duct.

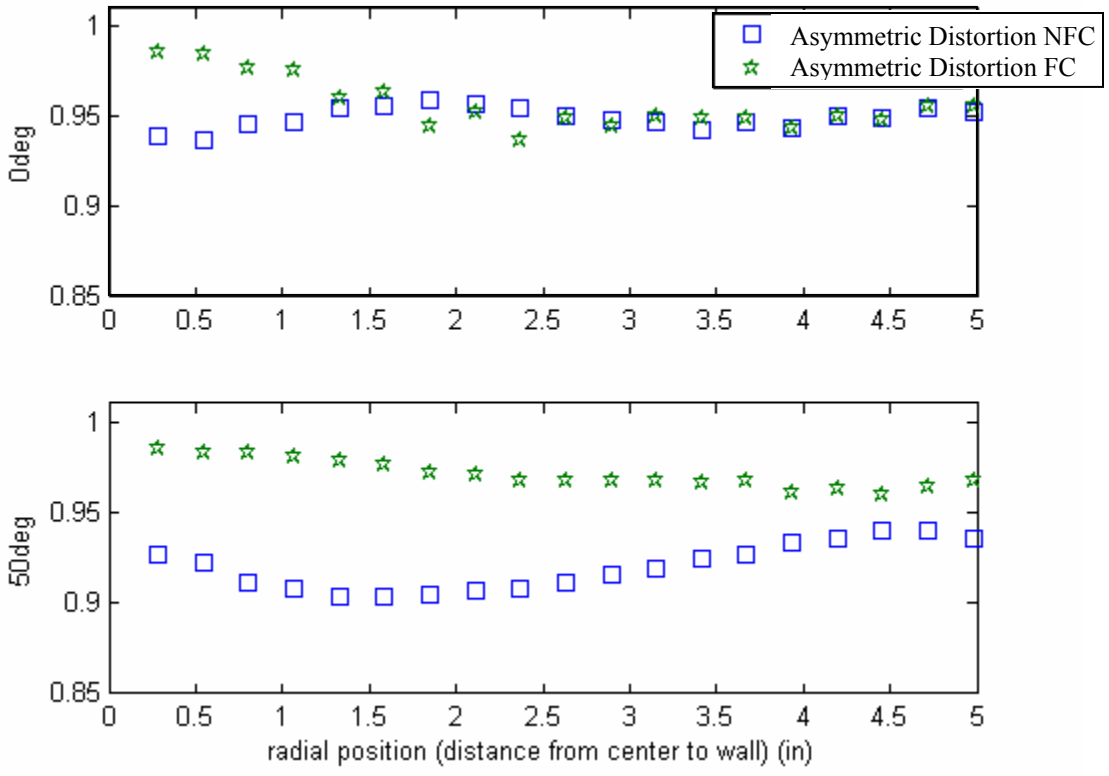

Figure 5.20 Asymmetric Distortion Case Total Pressure Ratio Variation with Flow Control

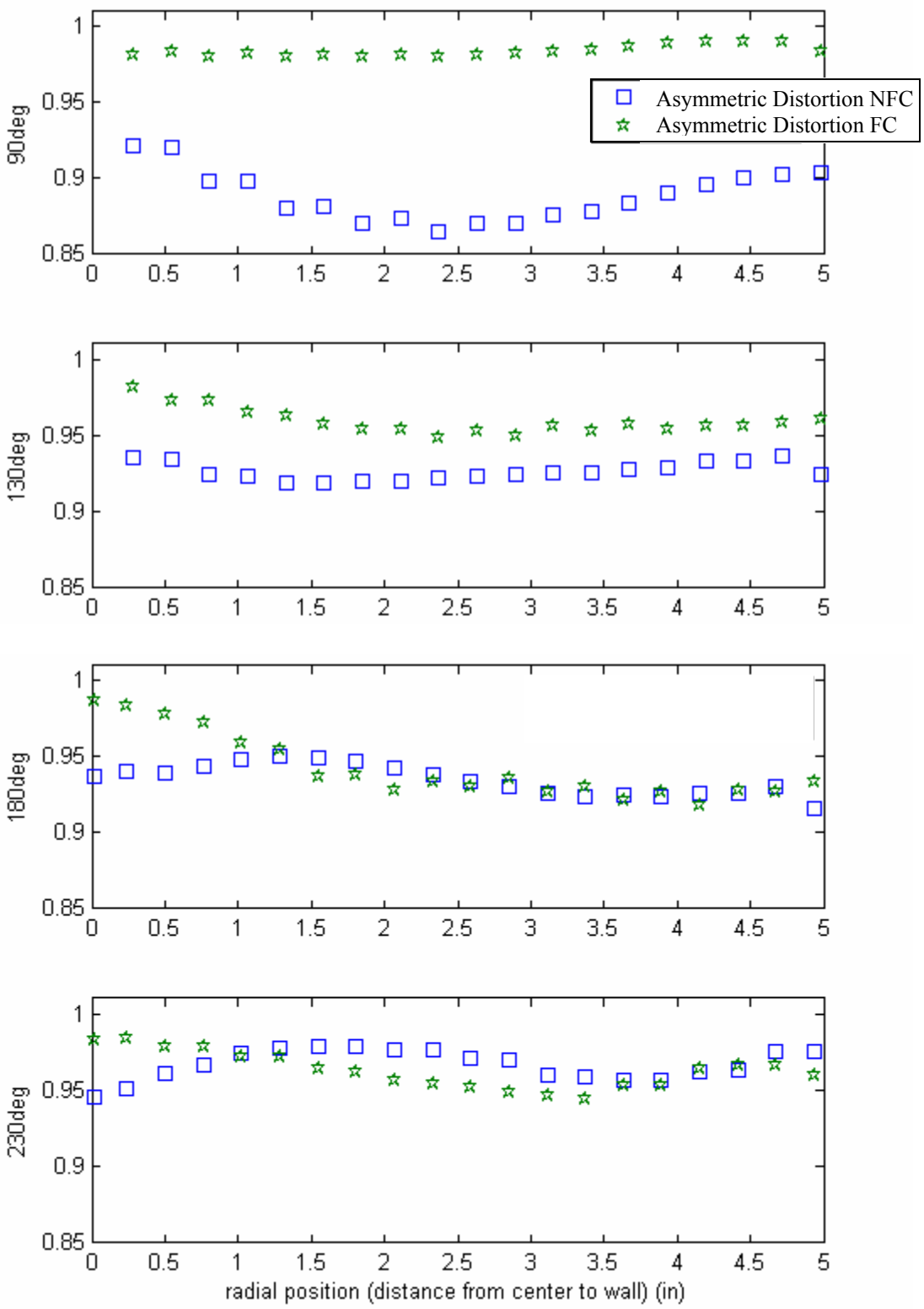

Figure 5.20 Asymmetric Distortion Case Total Pressure Ratio Variation with Flow Control

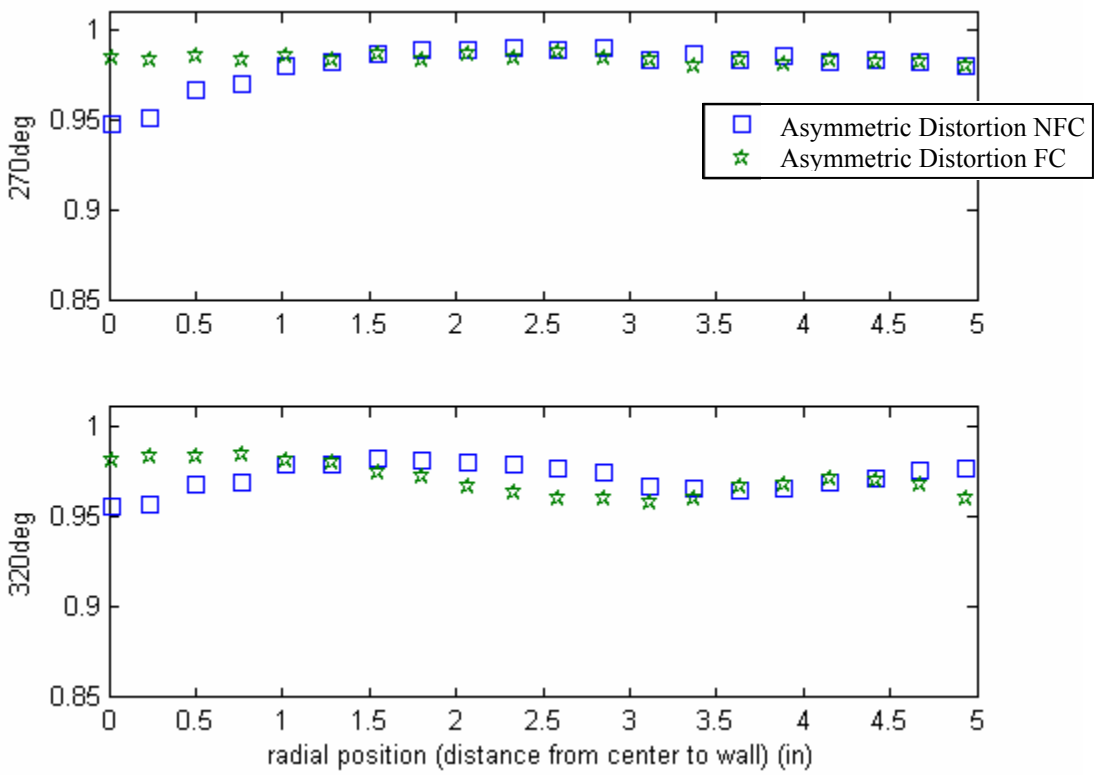

Figure 5.20 Asymmetric Distortion Case Total Pressure Ratio Variation with Flow Control

Figure 5.20 shows the total pressure ratio data points for the asymmetric distortion case with and without flow control at several circumferential locations. The data points at zero degrees show almost no change due to flow control outside of the central core region. At 50, 90 and 130 degrees, the flow control significantly improved the total pressure recovery across the entire radius. The 180 degree profile shows that while the flow control improved the pressure recovery in the core region, there was actually a loss in pressure recovery with flow control for radial positions ~1.25 inches from the core to 2.25 inches from the core. This is similar to the trend shown in the angle of attack case, and it occurs for the same reason. The side region of low total pressure is large enough to interfere with the central region of total pressure loss in the case without

flow control. The profiles for 230 and 320 degrees show the same trend more convincingly. At 270 degrees the flow is unchanged outside of the central core region.

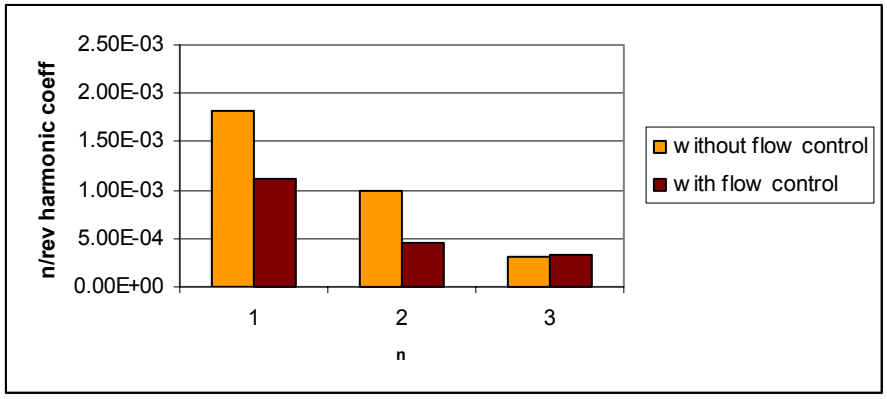

Figure 5.21 Effect of Flow Control on Harmonic Content for the Asymmetric Distortion Case

The effect of flow control on harmonic content for the asymmetric distortion case is shown in Figure 5.21. The trend is identical to the other flight condition cases where the 1/rev and 2/rev harmonic content is significantly reduced with the aid of flow control while the 3/rev harmonic content realizes an increase. Again, the overall effect is a decrease in harmonic content leading to a decrease in potential for high cycle fatigue relative to the same inlet duct without flow control.

5.4.4. Comparisons for Different Flight Conditions

So far, each of the experimental cases studied have been presented in terms of the effectiveness of the flow control technique for each case. In this section, comparisons will be made between the flight conditions to determine the affect of the off-design flight conditions and the effectiveness of the flow control technique at these conditions. The area-averaged pressure recovery, the distortion descriptors and the harmonic coefficients

will be re-examined in order to determine the changes in the flow field for the various flight conditions.

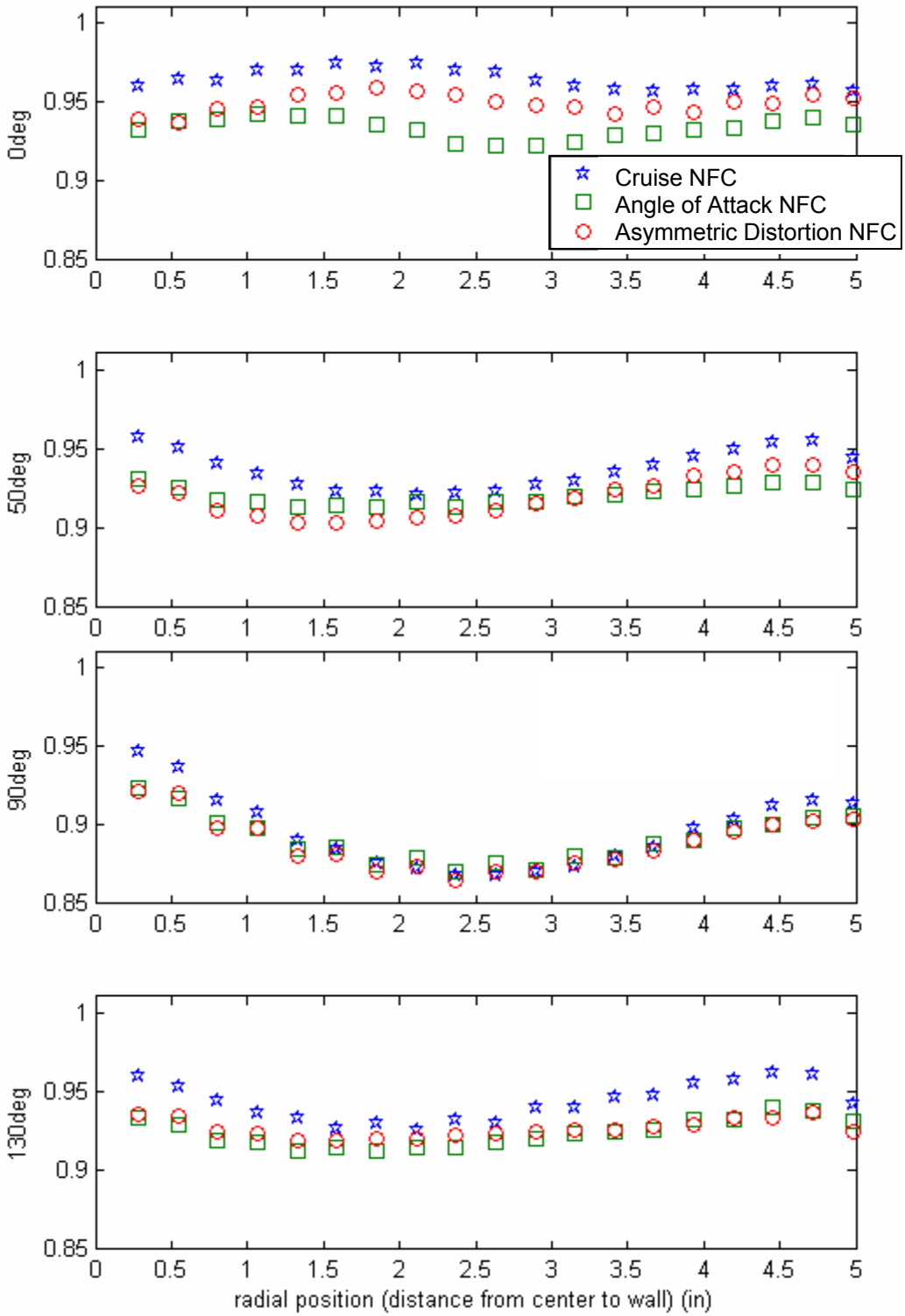

Figure 5.22 Total Pressure Ratio Variation for Different Flight Conditions without Flow Control

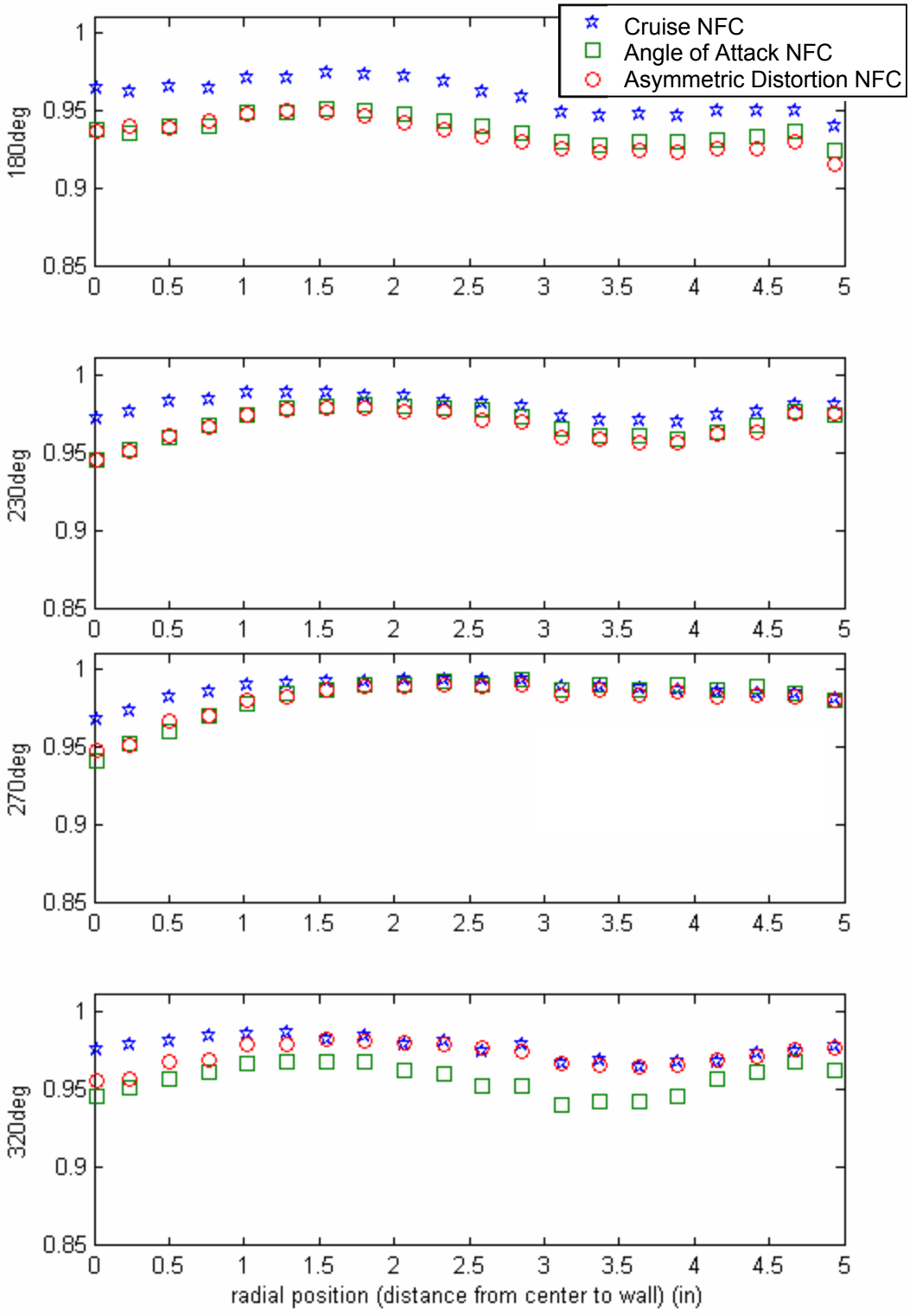

Figure 5.22 Total Pressure Ratio Variation for Different Flight Conditions without Flow Control

Figure 5.22 shows the radial data points for the three flight conditions without flow control. The cruise condition case is represented by blue stars, the angle of attack case is shown as green squares and the asymmetric distortion case is presented as red circles. The zero degree profile shows that in the side region, without flow control, the cruise condition case has the highest pressure recovery, followed by the asymmetric distortion case, with the angle of attack case showing the lowest total pressure recovery on that side. Zero degrees is located in the side region of the asymmetric distortion case which has the better pressure recovery. The 50 degree profile still shows the cruise condition case having the highest total pressure recovery, but now the angle of attack and asymmetric distortion cases show a similar response. The two profiles start out identical at the core region with the angle of attack case showing higher pressure recovery from ~0.5 inches from the center of the duct to ~2.5 inches. The asymmetric distortion case then shows better pressure recovery in the tip region. At 90 degrees, in the center of the large total pressure deficit, all three cases show similar pressure recovery with the cruise condition case showing higher pressure recovery in both the hub and tip regions. For the total pressure recovery profiles at 130, 180, and 230 degrees, the cruise condition case exhibits higher total pressure recovery while the angle of attack and asymmetric distortion cases show nearly identical lower total pressure recovery. At 270 degrees, the cruise condition case still shows better pressure recovery in the central core region; however, all three cases show the same total pressure recovery away from the core region. The final profile, at 320 degrees, illustrates the similarity between the cruise condition case and the asymmetric distortion case on the right hand side of the duct. The cruise condition case has a slightly higher pressure recovery in the core region following

which the cruise condition and asymmetric distortion cases achieve higher pressure recovery than the angle of attack case.

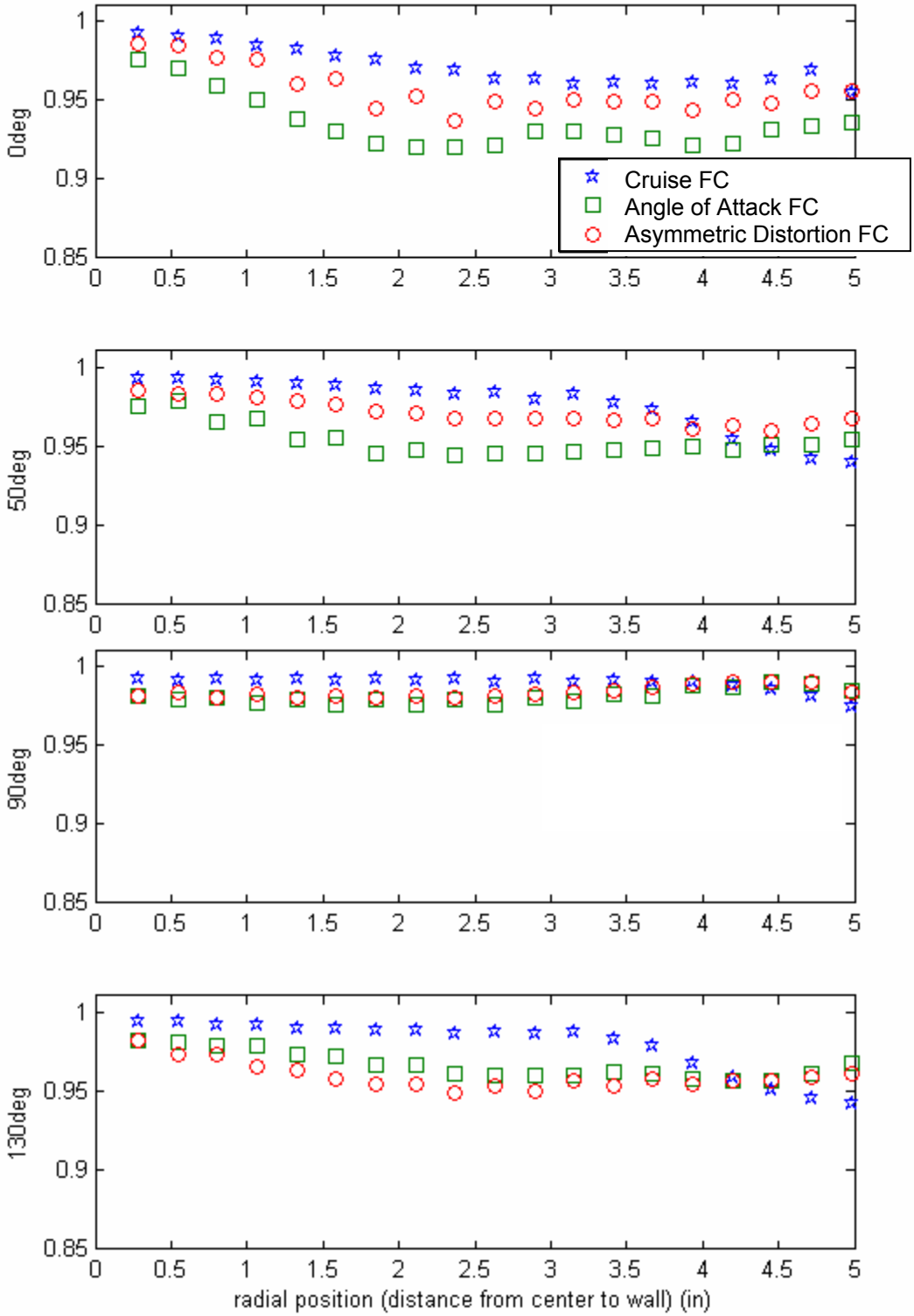

Figure 5.23 Total Pressure Ratio Variation with Flow Control for Different Flight Conditions

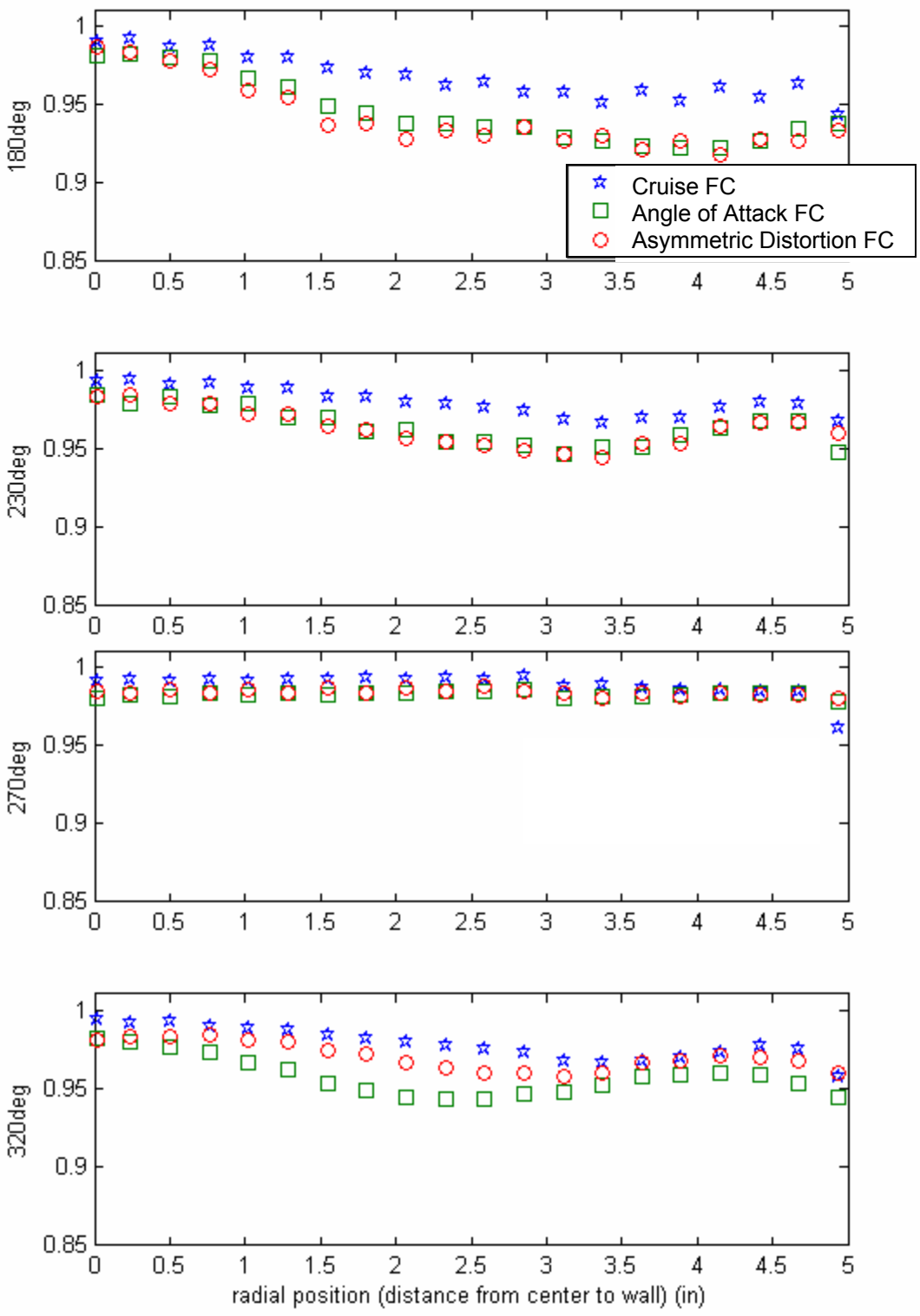

Figure 5.23 Total Pressure Ratio Variation with Flow Control for Different Flight Conditions

The total pressure ratio data points versus radial position for each flight condition with flow control are shown in Figure 5.23. The zero degree profile shows the cruise condition case with the highest total pressure recovery, followed by the asymmetric distortion case, with the angle of attack case showing the lowest total pressure recovery. The same trend is seen in the 50 degree profile from the core region up to the tip region. In the tip region, the tip radial distortion in the cruise condition case yields a lower total pressure for the cruise condition case. The highest total pressure ratio in the tip region is shown by the asymmetric distortion case. At 90 degrees the three cases exhibit similar behaviors with the cruise condition case showing slightly higher total pressure recovery from the core region to the tip region and slightly lower total pressure recovery in the tip region. The symmetry of the cruise condition and angle of attack cases can be seen through the similarity in the 130 degree and 50 degree profiles. The asymmetric distortion case demonstrates asymmetry and falls closer to the angle of attack case at 130 degrees. At 180 and 230 degrees the angle of attack and asymmetric distortion cases are nearly identical in their low total pressure recovery while the cruise condition case shows better pressure recovery over the entire radius. The 270 degree profile shows nearly uniform total pressure recovery for all three cases with the cruise condition case showing marginally better pressure recovery from the core region out to the tip region and slightly lower pressure recovery in the tip region. At 320 degrees the cruise condition case shows higher pressure recovery followed by the asymmetric distortion case. The lowest pressure recovery in this region is found in the angle of attack case.

Figure 5.24 shows the circumferential distortion intensity versus ring number for each of the experimental cases. From this figure it is easy to see that the bulk of the

reduction in circumferential distortion intensity occurs in the inner rings. The core flow region grows with the addition of flow control creating a larger region of clean flow in the center of the duct. The outermost ring sees significantly less reduction in circumferential distortion intensity than the innermost ring. For the angle of attack and asymmetric distortion cases, the fourth ring (which lies in the tip region) actually sees an increase in circumferential distortion with the addition of flow control.

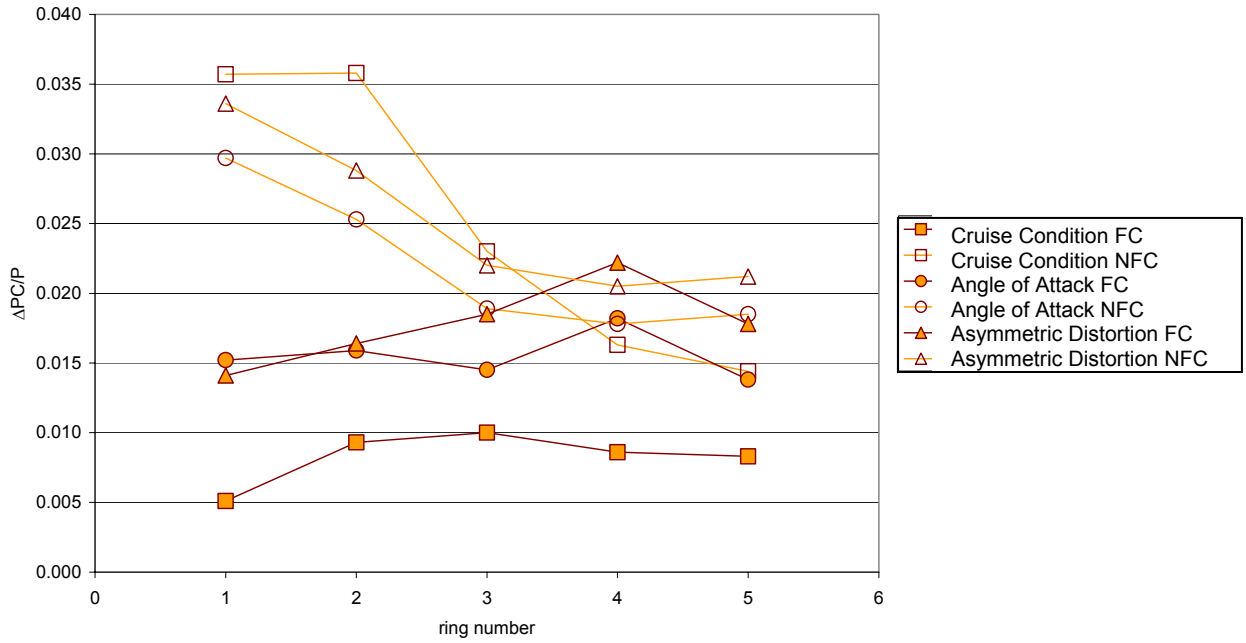

Figure 5.24 Effect of Flight Condition on Circumferential Distortion

Figure 5.25 shows the circumferential extent function for each flight condition with and without flow control. In each case the extent of the distortion has been reduced with the addition of flow control. Looking back at the total pressure contours for the flight conditions with and without flow control, this trend is easily recognized. Since the area of distortion in the top central region of the duct is eliminated with flow control, that extent is also eliminated from the extent of distortion for each case. This is the main

reduction in extent since the side regions roughly maintain their circumferential extent of distortion with and without flow control. In terms of the flow entering the engine, the fan blades now spend much less time in a region of distorted flow over one revolution. The reduction in the extent of circumferential distortion actually increases with increasing ring number. The tip rings, which start with a larger extent of distortion, end with about the same extent of distortion present in the other rings. The asymmetric distortion case undergoes less of a reduction in extent of distortion than the other two cases. In the uncontrolled cases the angle of attack case produces the highest extent of circumferential distortion followed by the asymmetric distortion case and then cruise condition. This can also be seen graphically in the total pressure contour plots for each case. For the flight conditions without flow control, the angle of attack case has one large region of solid total pressure loss whereas the cruise condition and one side of the asymmetric distortion case have some high pressure recovery flow in between the vortices from the second turn and the corner vortices from the first turn. With the addition of flow control, the asymmetric distortion case yields the highest extent of distortion; however, all three cases lie fairly close together.

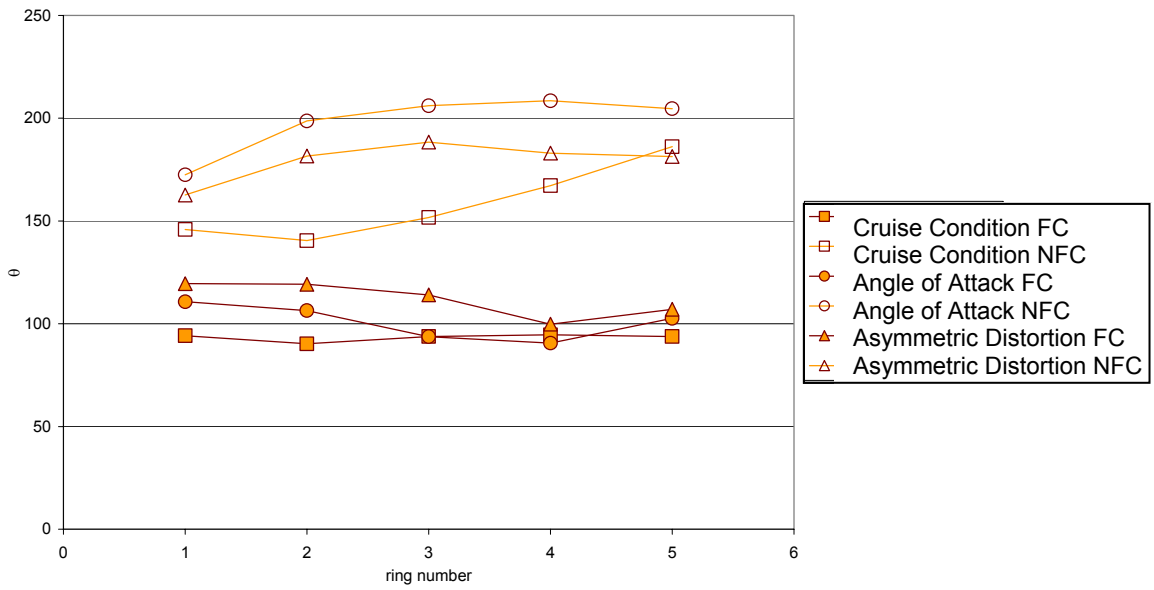

Figure 5.25 Effect of Flight Condition on Extent Function

The circumferential multiple per revolution content is shown in Figure 5.26. The multiple per revolution content is one for each of the uncontrolled cases. This can be seen in the individual plots of circumferential position versus total pressure recovery which show a low total pressure recovery for one large region in the uncontrolled cases. In the cases with flow control, there are two regions of low total pressure recovery. Based on the definition of multiple per revolution content as an area weighting of the regions of low total pressure, the MPR content with flow control varies between one and two. Figure 5.26 shows the asymmetry present in the cruise condition and angle of attack cases. For rings with fairly even total pressure recovery, very little asymmetry is required to affect the MPR values. In addition, there is some asymmetry regarding the inner rings, especially in the angle of attack case. This could be due to some small difference in the distortion generating grids or some dust or dirt along the duct which causes one corner vortex to grow more than the other.

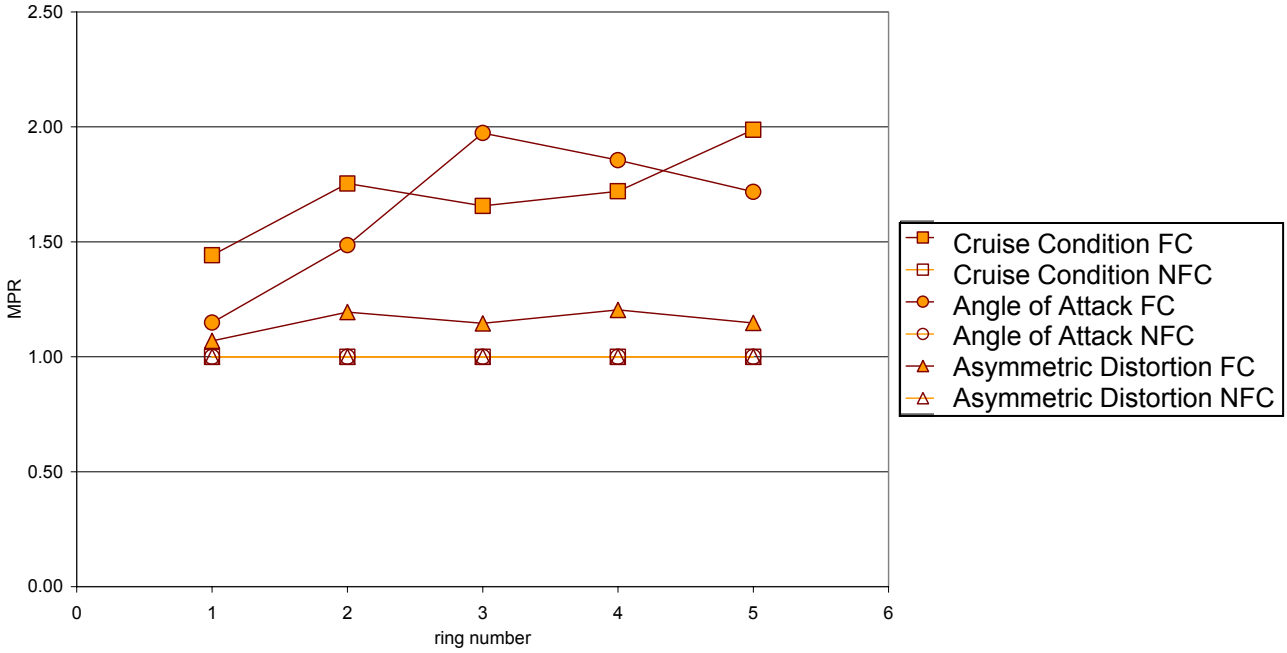

Figure 5.26 Effect of Flow Control on Multiple per Revolution Function

The radial distortion results shown in Figure 5.27 are very similar for all cases without flow control. All three lines lie close to one another showing the distortion concentrated in rings two and three with the highest pressure recovery in ring five. For the angle of attack and asymmetric distortion cases with the addition of flow control, the hub region shows improved flow while the radial distortion remains concentrated in rings two and three. Ring four shows some radial distortion while ring five shows higher than average pressure recovery. The cruise condition case with flow control is the exception, demonstrating tip radial distortion. Looking back at the pressure contour shown in Figure 5.6, the extra distortion in the tip region is the source of this tip radial distortion. In Figure 5.7 the first region of low total pressure in rings four and five now covers an extent of 70 degrees as opposed to the ~40 degree extent shown in rings 1-3. This same trend is not realized in the angle of attack and asymmetric distortion cases.

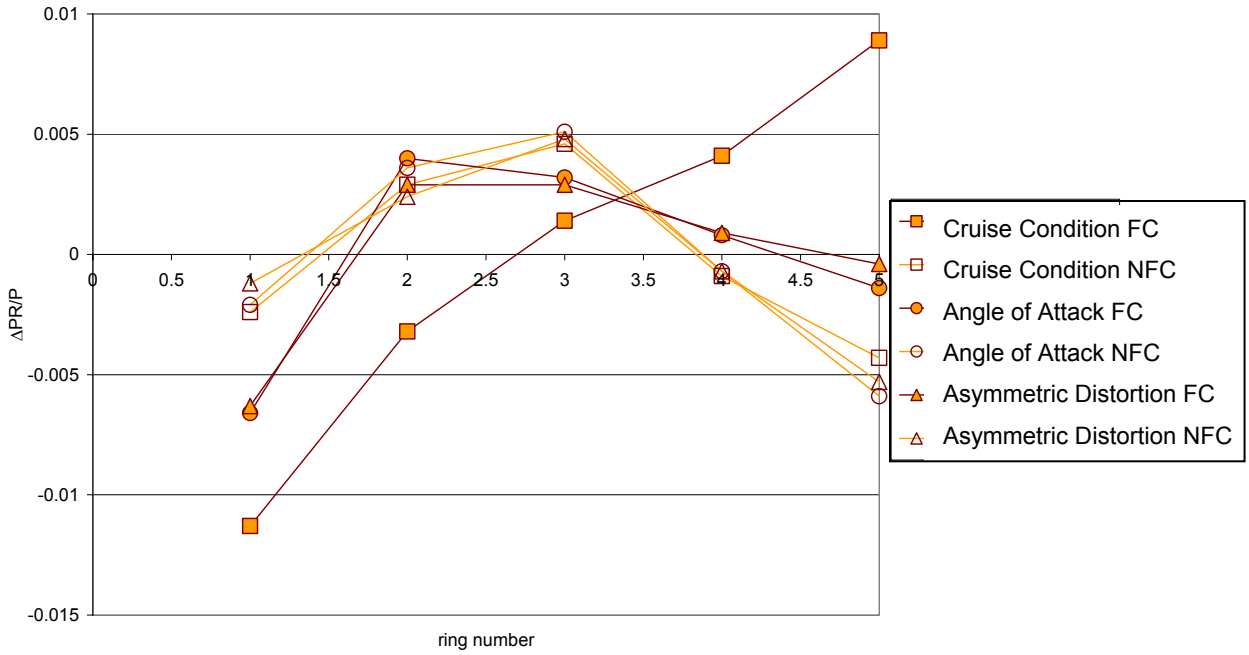

Figure 5.27 Effect of Flow Control on Radial Distortion

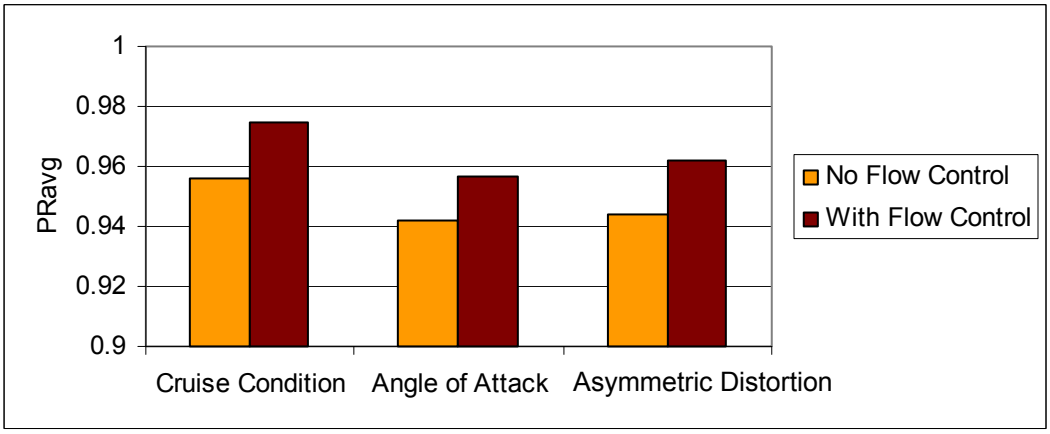

Figure 5.28 Effect of Flow Control on Average Pressure Recovery for Different Flight Conditions

Figure 5.28 shows the improvement in pressure recovery with the addition of flow control. The orange bars show the average pressure recovery without flow control while the maroon bars show the results with the addition of flow control. The cruise condition case has the highest pressure recovery for the cases with flow control and also without

flow control. The relative improvement in pressure recovery with the addition of flow control is similar for each flight condition, but the angle of attack and asymmetric distortion cases have lower total pressure recovery both with and without flow control. This is due to the extra losses in these cases designed to represent different flight conditions.

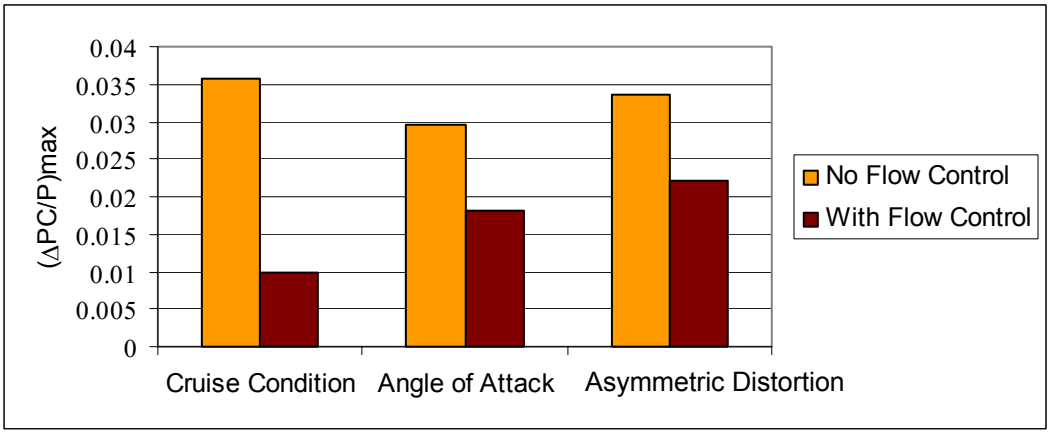

Figure 5.29 Effect of Flow Control on Circumferential Distortion for Different Flight Conditions

Figure 5.29 shows the reduction in circumferential distortion with the addition of flow control. The cruise condition case without flow control has the highest circumferential distortion, followed by the asymmetric distortion case and finally the angle of attack case. This trend differs from that for total pressure recovery because the circumferential distortion term relies on the average total pressure recovery and the area of low pressure regions (regions below the average pressure recovery) weighted by the extent of the region of low total pressure. The circumferential distortion will be low even if the total pressure recovery is low as long as the total pressure loss is uniform throughout the AIP. This is the effect seen here.

The addition of flow control reduces the circumferential distortion for all three cases with the largest reduction occurring for the cruise condition case. The cruise condition distortion is reduced by ~70% with the addition of flow control. This significant reduction occurs because the cruise condition case represents the design point for the flow control system. There is still a reduction in circumferential distortion for the off-design conditions represented by the angle of attack and asymmetric distortion cases, but the effect is not as substantial. The reason for this is the additional distortion in the off-design cases in the form of stronger corner vortices from the first turn of the duct which are unaffected by the flow control technique. Therefore, the flow control is still effective in reducing the circumferential distortion at off-design conditions but to a lesser degree than for the design point, as expected.

The multiple per revolution data are shown again in Figure 5.30. The MPR content for all three cases without flow control is one. In the uncontrolled case, each flight condition produces one large segment of low total pressure flow. In the cases with flow control, cruise condition and angle of attack produce an MPR of up to two where the two regions of low total pressure are of equal area. The MPR descriptor is an area weighting of the low total pressure. For this reason, the asymmetric distortion case with flow control, where the two regions of low total pressure are of different intensity or area, yields an MPR which does not exceed 1.2. This says that the maximum MPR shows that one region of low total pressure is five times larger in area than the other. This is a significant asymmetry represented in the asymmetric distortion case.

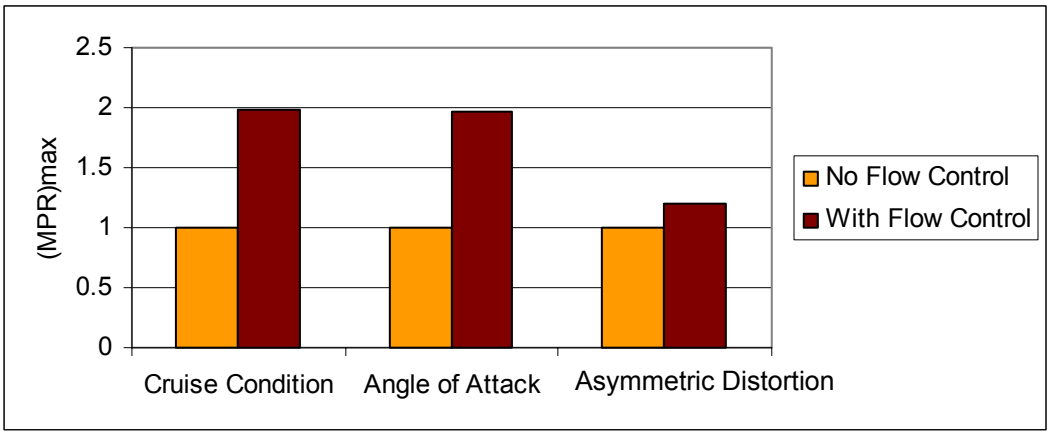

Figure 5.30 Effect of Flow Control on MPR for Different Flight Conditions

The maximum radial distortion is shown in Figure 5.31. Radial distortion is a measure of the distribution of pressure loss between the five rings. If the pressure loss in each ring is similar, the radial distortion will remain small. The radial distortion increases with a concentration of total pressure loss within one or two rings. The information in the figure shows that the pressure losses are more uniformly distributed in the cruise condition case without flow control than with the addition of flow control. In the earlier depiction of radial distortion, it was shown that the cruise condition case showed convincing tip radial distortion with the addition of flow control. This trend is again recorded in Figure 5.31. In the angle of attack and asymmetric distortion cases the distribution of total pressure losses throughout the rings is actually becoming more uniform. Looking back at the total pressure contours for the various cases, these trends can be seen. The cruise condition case shows significantly more total pressure loss in the tip region as opposed to the inner rings; whereas, the angle of attack and asymmetric distortion cases show more uniform total pressure loss throughout the rings.

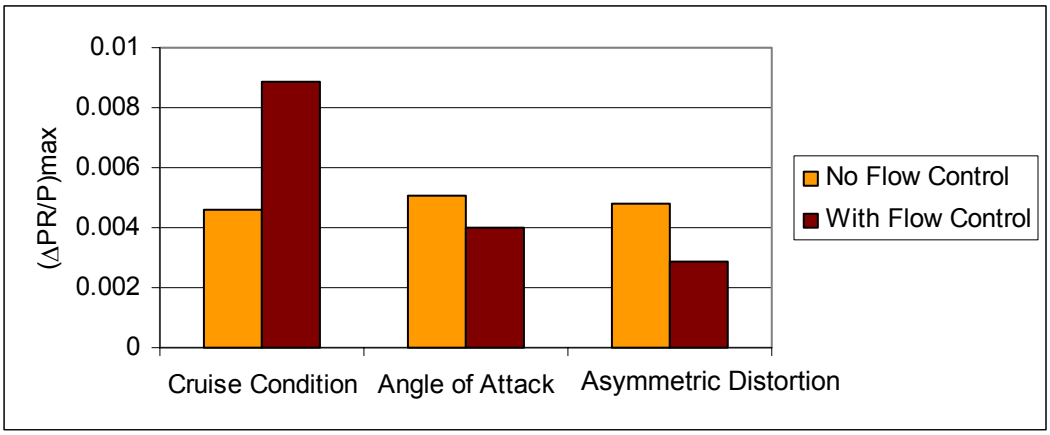

Figure 5.31 Effect of Flow Control on Radial Distortion for Different Flight Conditions

In comparing Figure 5.9, Figure 5.15, and Figure 5.21 the highest 1/rev harmonic content occurs in the cruise condition case without flow control, but the lowest 1/rev harmonic content is found in the cruise condition case with flow control. Therefore, the largest reduction in harmonic content can be found in the cruise condition case where the initial distortion produces more harmonic content than the other two cases, but the flow control is significantly more effective. The data for the 2/rev harmonic content is similar in all three cases, showing a significant reduction with flow control. In each case the 3/rev harmonic content increases with the addition of flow control, but to varying degrees. In the asymmetric distortion case, the 3/rev content is nearly unchanged with flow control; whereas, in the angle of attack case the 3/rev content is almost doubled with flow control. The increase in 3/rev content for the cruise condition case lies in between the response of the other two cases. In each case, though, the 3/rev content is only a fraction of the initial 1/rev harmonic content. Since the 1/rev and 2/rev harmonic content realizes significant reduction with the introduction of flow control, and the 3/rev harmonic content is significantly smaller to begin with, the flow control was found to be

successful in reducing harmonic content of the flow field entering the fan stage. This will in turn reduce the high cycle fatigue in the fan stage.

5.4.5. Summary

The experimental results have been presented showing large total pressure distortions for each of the flight conditions without flow control. The most severe total pressure losses are regained with the addition of flow control while the moderate regions of total pressure loss remain. The off-design flight conditions increased pressure losses along the sides of the AIP but maintained pressure losses similar to the cruise condition case along the top and bottom of the AIP. With the addition of flow control, the increased pressure loss in the side regions is unaffected, but the large pressure loss along the top of the AIP is improved, similar to the cruise condition case.

In terms of the standard distortion descriptors, the circumferential distortion in the uncontrolled cases is actually lower for the off-design flight conditions due to the more uniform total pressure loss. The pressure recovery is lower for the off-design flight conditions than for the design or cruise condition. The circumferential extent of distortion is larger for the off-design flight conditions. Both the multiple per revolution content and the radial distortion are similar for all three flight conditions without flow control. The harmonic content is lower for the off-design conditions in terms of the 1/rev harmonic coefficient and similar to the cruise condition for the 2/rev and 3/rev coefficients. This is likely caused by the more uniform pressure loss throughout the AIP in the off-design cases.

With the addition of flow control, the pressure recovery is improved for all flight conditions and the circumferential intensity and extent are decreased. The effect is

greater for the design condition of cruise flight. The multiple per revolution content is increased in all cases, but more so for the angle of attack and cruise condition cases due to the symmetry of total pressure losses at the AIP. For the cruise condition case the 1/rev harmonic coefficient is reduced by almost 70% while the off-design conditions see reductions closer to 40%. For the 2/rev coefficient, all three cases see reductions of near 50%. The 3/rev coefficient actually increases with flow control for all three cases. The asymmetric distortion case shows a minor increase, while the 3/rev harmonic coefficient for the angle of attack case doubles. The increase in 3/rev harmonic coefficient for the cruise condition falls in between the other two with an increase of about 1.5 times the uncontrolled 3/rev harmonic coefficient. The radial distortion decreases for the off-design flight conditions due to the increased flow uniformity while the cruise condition yields an increase in radial distortion. The increase is due to remaining total pressure losses in the tip region, but it is not clear how this will affect a compression system.

5.5. CFD Comparison

The CFD predictions at the AIP were presented in Chapter 2 for the baseline case. This profile will be compared to the experimental results for the same case to highlight the differences between the CFD predictions and the experimental results. The angle of attack simulation was based on the total pressure profile at the inlet throat cross section based on the inaccuracy of the CFD results at the AIP. CFD codes still lack an accurate representation of vortex dissipation.

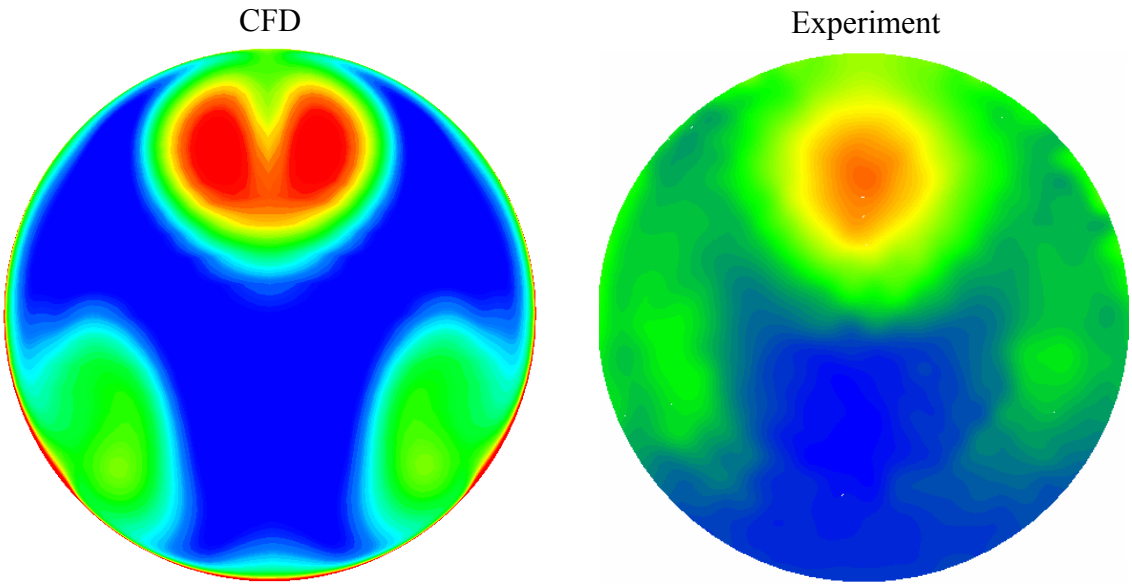

Figure 5.32 CFD and Experimental AIP Total Pressure Contours for Cruise Condition Case without Flow Control

Figure 5.32 repeats the CFD and experimental AIP profiles for the cruise condition case without flow control in order to compare the results. The CFD generated contour shows tighter vortices. The top vortices, which initiate from the second turn show a more distinct area of low total pressure with very little outward spreading of the vortices. The region of greater total pressure loss, shown in red, is greater for the CFD generated profile. In addition, the red region is clearly separated showing two separate vortices. The experimental profile shows a smaller region of concentrated total pressure loss. The overall area of total pressure loss is larger for the experimental case. The vortices from the first turn of the duct appear along the sides of the duct. In the CFD generated contour these vortices are more concentrated but cover approximately the same overall area as the side vortices in the experimental case. Additionally, the side vortices for the CFD case are positioned lower along the sides at the AIP. The experimental case shows the center of these vortices at about 0 and 180 degrees; whereas, the CFD contour

shows the center of these vortices at about 225 and 315 degrees. These differences in positioning, strength, and overall area of total pressure loss are largely due to the vortex dissipation modeling. The qualitative trends shown in the CFD contour at the AIP provide reasonable predictive capabilities; however, the comparison of the CFD and experimental results shows that experimental verification of CFD predictions is still necessary. For this reason, the angle of attack simulation relied on the data at the inlet throat where vortex dissipation is not a factor.

5.6. DYNTECC Predictions

The experimental results in this research show predominately circumferential distortion; however, additional distortion in the form of tip radial distortion is demonstrated in the cruise condition case with flow control. The literature shows mixed results due to radial distortion, particularly tip radial distortion, with some cases increasing the compressor stability margin and other cases decreasing the compressor stability margin (AIR 1419, 1983). Circumferential distortion, on the other hand, has been shown to cause a loss in stability margin directly proportional to the intensity and extent of the circumferential distortion. This result was examined in the DYNTECC simulations.

The six test cases outlined in the experimental work were input into DYNTECC to determine the effect of varying inlet total pressure distortion on the operation and stability margin of a compressor stage. The AIP total pressure profiles were broken into four segments as seen in Figure 5.33, and the average pressure recovery for each segment was the inlet condition for each parallel compressor. These values can be found in Table 5.1.

Table 5.1 Total Pressure Losses Input to DYNTECC for the Parallel Compressors for Each Case

	Cruise Condition NFC	Cruise Condition FC	Angle of Attack NFC	Angle of Attack FC	Asymmetric Distortion NFC	Asymmetric Distortion FC
1	-4.2	-3.9	-7.7	-7.7	-5.5	-5.2
2	-13.1	-1.9	-12.5	-2.2	-12.9	-1.9
3	-5.2	-4.4	-7.0	-7.7	-7.5	-8.1
4	-1.6	-2.1	-1.8	-1.8	-1.8	-1.8

The parallel compressor divisions for the cruise condition cases are shown in Figure 5.33. The cruise condition case without flow control clearly has one parallel compressor operating with severe total pressure loss (top quadrant), two with moderate loss (side quadrants) and the fourth parallel compressor with minimal total pressure distortion (bottom quadrant). With the addition of flow control, there are three parallel compressors with moderate total pressure loss and one with minimal total pressure loss (bottom quadrant).

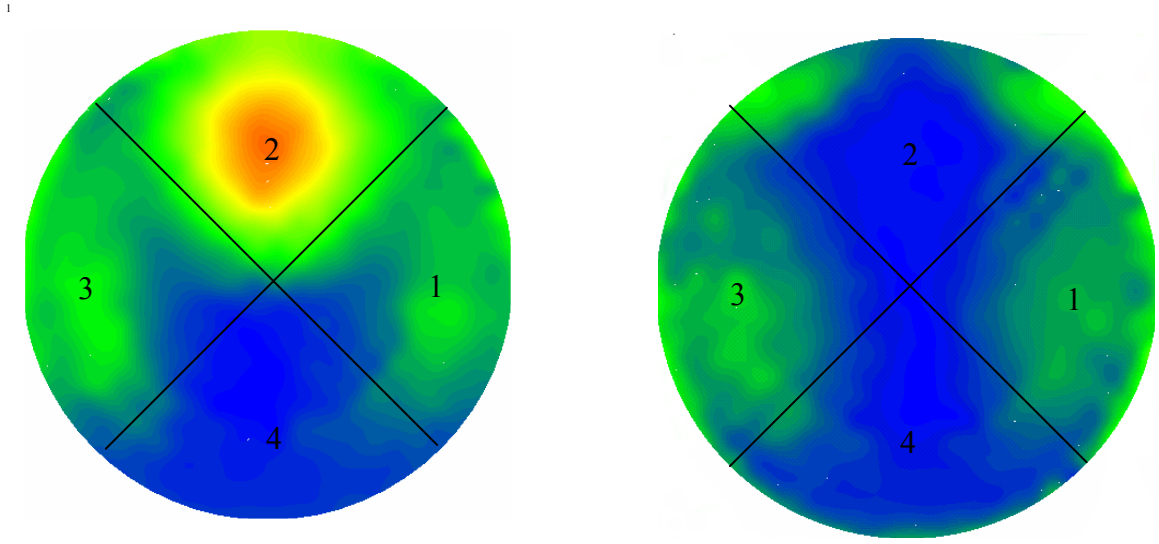

a). No Flow Control **b). Flow Control**

Figure 5.33 Parallel Compressor Divisions for Cruise Flight Case

At the 70% speed line the corrected mass flow normalized by the flow area is matched between the inlet tested and the rotor (stage 35) modeled. The operating points were calculated as described in Section 4.2 for each of the six cases run on the 70% speed line as seen in Figure 5.34. The total pressure losses for the four quadrants were specified as shown in Table 5.1. Additionally, the exit static pressure was used to define the exit flow and was set as the ambient total pressure. In this way, the stage is dumping to atmospheric conditions, similar to a compressor rig. The undistorted speed line and undistorted operating point are shown in Figure 5.34. The undistorted line shows where the compressor would operate if there were no total pressure losses at the entrance. An additional point is shown for a classical 180 degree distortion pattern which includes a 10% total pressure loss over half of the inlet area (AIR 1419, 1983). The 180 degree distortion shows a distorted operating point similar to the experimental distortion cases without flow control.

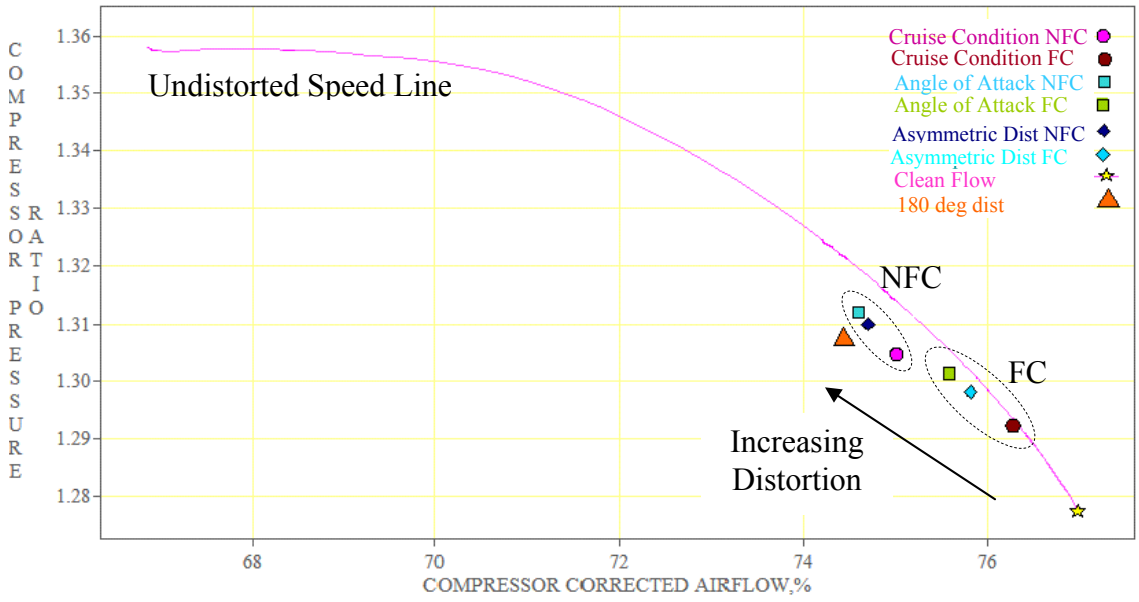

Figure 5.34 DYNTECC Stage 35 Increase in Operating Points with Distortion for 70% Corrected Rotor Speed

The operating points are seen to drop off the undistorted speed line and move up along the distorted speed line. The operating points move up along the speed line based on the reduction in flow. The distortion reduces the average axial velocity through the AIP. This reduction in axial velocity will result in a reduced mass flow through the stage, increasing the pressure ratio as the operating point moves up along the speed line. This occurs because the simulation is run as a rig test. In a compressor rig test, the ambient pressure at the exit allows the operating line to change based on the inlet conditions. In an engine environment, the downstream stages would pull on the initial stages, in an effort to keep the operating point constant with additional distortion and could actually result in the operating point moving downward on the speed line.

The reduction in stability limit with increasing distortion is shown in Figure 5.35. For the calculation of the stability limit, each case began at the operating points shown in Figure 5.34 and the back pressure was ramped until one of the parallel compressors reached the clean flow stability limit. The symbols for each case are identical to those in Figure 5.34. Now the stability limit for each case is seen to decrease depending on the amount of distortion. For instance, the baseline or cruise condition case shows instability at a higher mass flow, but the same pressure ratio as clean flow. The stability limit is decreasing because the distortion in the parallel compressor with the largest total pressure loss forces the operating point to the clean flow distortion limit. This point is then averaged with the operating points for the other parallel compressors and the overall stability limit decreases. The distorted parallel compressors reach the clean flow stability limit first because as the back pressure is increased, the operating point continues to

move up along the speed line. The model calculations stop when one of the parallel compressors reaches the clean flow stability limit.

The 180 degree distortion with 10% loss over half of the entrance area is shown again as the orange triangle. For the decrease in stability line, the 180 degree distortion is not as severe as the experimental data without flow control. Therefore, the engine testing for this airframe will require more severe distortion testing than a 180 degree screen producing a 10% pressure drop.

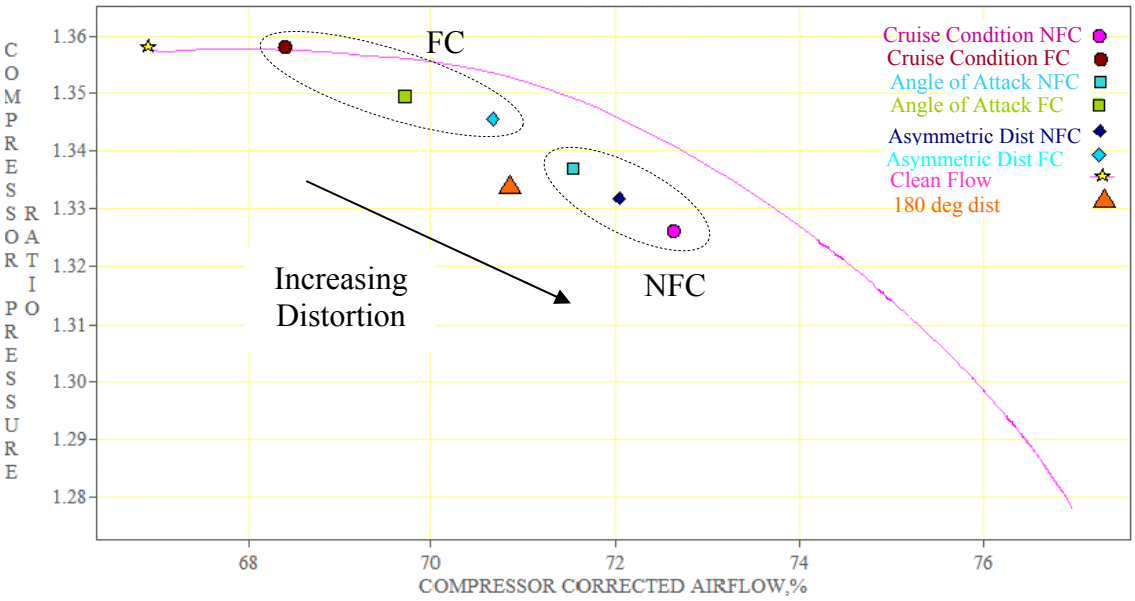

Figure 5.35 DYNTECC Stage 35 Decrease in Stability Limit Points with Distortion at 70% Corrected Rotor Speed

Figure 5.34 and Figure 5.35 are combined in Figure 5.36 to show the combined effects of the increased operating points and decreased stability limits. The stability margin, as previously defined on page 19, will use the pressure ratio difference between the operating point at a given condition and the stall point normalized by the operating point pressure ratio. This value is multiplied by 100 to obtain a percent difference based

on the overall pressure ratio of the stage. The clean flow stability margin is represented by the difference in pressure ratio between the two yellow stars. This is the maximum available stability margin of 6.4%. The cruise condition case without flow control is shown in pink circles. The proximity of the two circles shows the reduction in stability margin for the STRICT inlet duct configured with NASA Stage 35. If no flow control technique was implemented or if the flow control failed during flight, this would be the stability region available at the 70% speed line. The 180 degree distortion, shown in orange triangles illustrates a larger stability region. The stability margins are given in Figure **5.37** corresponding to the points shown in Figure 5.36.

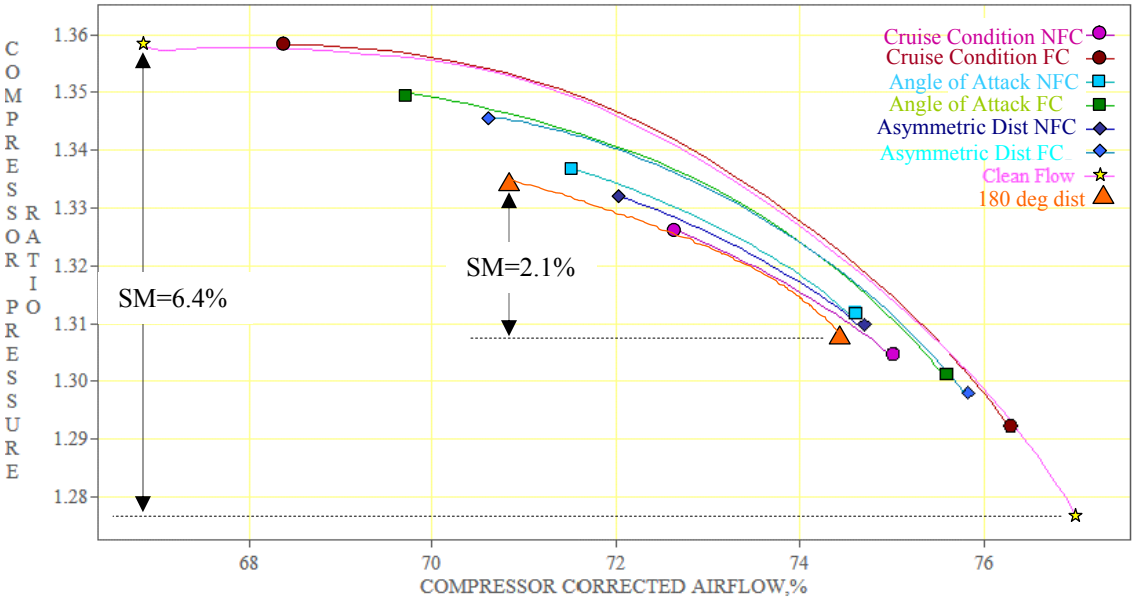

Figure 5.36 DYNTECC Stage 35 Decrease in Stability Margin with Distortion at 70% Corrected Rotor Speed

Figure **5.37** shows that the stability margin decreases slightly for the cruise condition case with flow control. The angle of attack and asymmetric distortion cases with flow control show a larger decrease in stability margin, but still have a reasonable stability margin.

The 180 degree distortion falls in between the experimental cases with flow control and the experimental cases without flow control indicating that more extreme distortion testing will be required for the engine. The cruise condition case without flow control has the smallest stability margin at just over 1.5% with the angle of attack and asymmetric distortion cases without flow control showing slightly higher stability margins, still less than 2%. The loss of stability margin for the STRICT inlet duct without flow control is greater than 70%.

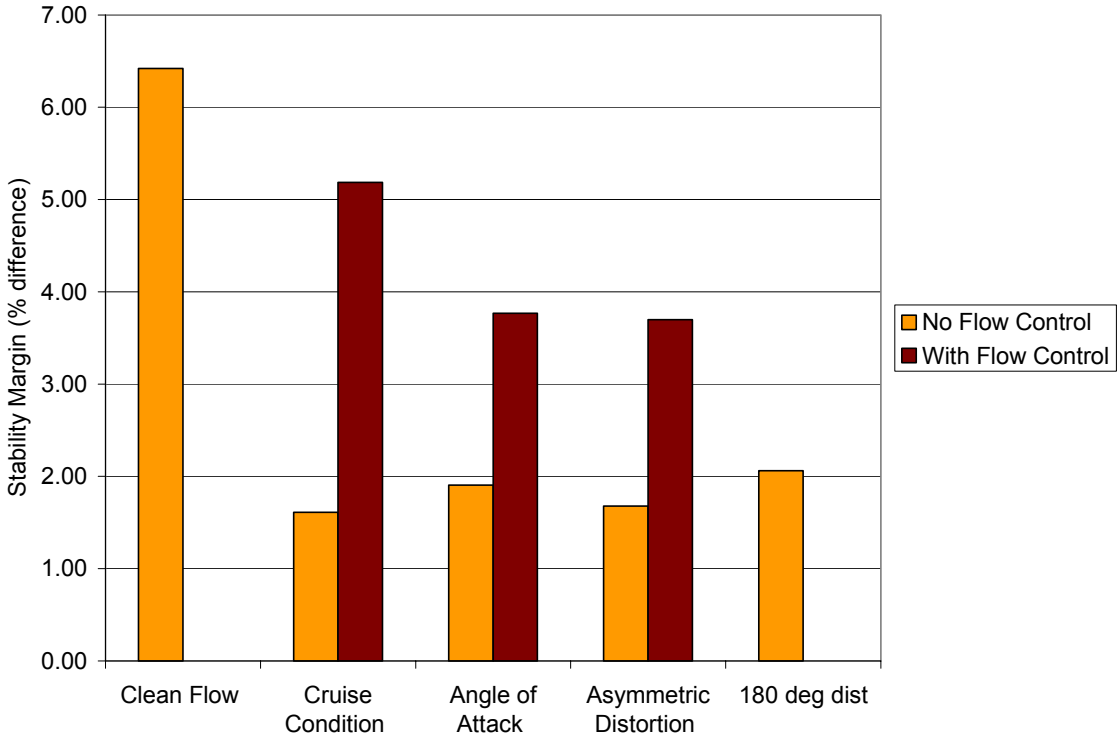

Figure 5.37 Stability Margin Comparison

The percentage loss in stability margin is displayed in Figure 5.38. The experimental cases without flow control all show losses in stability margin of greater than 70%. With the addition of flow control the cruise condition case recovers more than 50%

of the stability margin, resulting in a loss of less than 20% of the clean flow stability margin. The angle of attack and asymmetric distortion cases experienced a loss in stability margin of over 30% with the addition of flow control. For comparison, the 180 degree distortion revealed loss in stability margin of almost 70%.

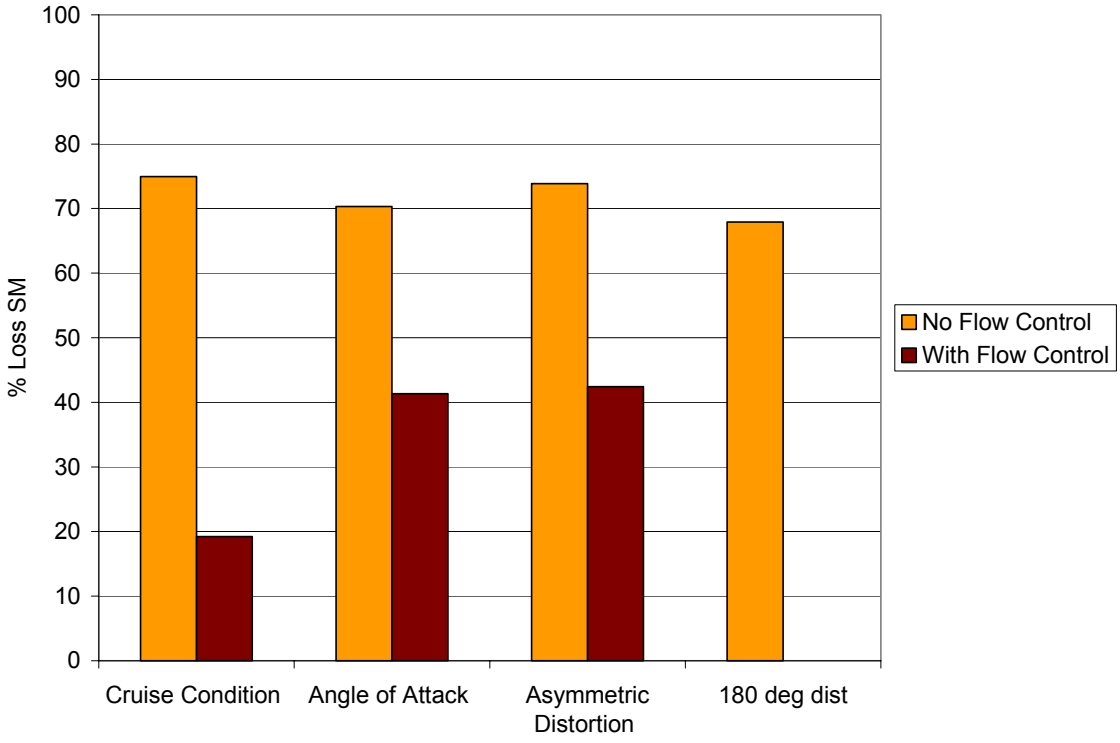

Figure 5.38 Loss in Stability Margin at Different Corrected Rotor Speeds

The experimental cases have revealed a significant loss in stability margin due to the total pressure losses within the inlet duct. A significant portion of these losses is recovered with the implementation of a successful flow control technique. Although the circumferential redistribution portion of DYNTECC was enabled, the flow angularity from the counter-rotating vortices is not captured in the input data. Therefore, all

changes in stability margin found through the simulations are based on changes in inlet total pressure.

The stability margin decreased with increasing distortion but was recovered to a large extent with the addition of flow control. These trends will likely occur for any corrected rotor speed. The magnitude of the variations will be affected by changes in rotor speed or changes in compression system, but the same trends will be seen. The classical distortion pattern of a ten percent total pressure loss over 180 degrees of the inlet fell in between the experimental cases with flow control and the experimental cases without flow control. This indicates that a stronger distortion will need to be utilized in engine distortion testing for an engine to match this inlet duct flow field without flow control.

5.7. Summary

The experimental investigation showed the changes in the AIP flow field for different flight conditions with and without flow control. For the cruise condition case, the total pressure recovery was improved by 2% with the addition of flow control. The angle of attack and asymmetric distortion cases saw increases of 1.5% and 2% respectively. The off-design conditions of angle of attack and asymmetric distortion without flow control had a 1.5% loss in total pressure recovery as compared to the cruise condition case. All flight conditions tested showed a reduction in circumferential intensity with flow control. The cruise condition case reduced maximum circumferential distortion by 70% with the addition of flow control. A reduction in maximum circumferential distortion of 40% occurred for the angle of attack case with flow control, and 30% for the asymmetric distortion case with flow control. The 1/rev and 2/rev

harmonic coefficients were decreased by 40% for all flight conditions with the addition of flow control. The flow quality at the AIP was significantly improved with the addition of flow control.

Finally, the total pressure distributions were used to predict the changes in stability margin due to off-design flight conditions and the improvement of the stability margin with the addition of flow control. Without flow control, all three cases show similar reduced stability margins on the order of 30% of the original stability margin for Stage 35 at 70% corrected rotor speed. With the addition of flow control, the cruise condition improves the stability margin to 80% of the original value while the off-design conditions only recover to 60% of the original margin. Overall, the flow control has been found to be extremely beneficial in improving the operating range of a compression system for the same inlet duct without flow control.

6.0 Conclusions and Recommendations

6.1. Summary and Conclusions

A serpentine inlet duct was tested experimentally at three different simulated flight conditions to determine the flow quality produced at the AIP. The three flight conditions consisted of a cruise or baseline condition, angle of attack, and asymmetric distortion. The angle of attack case was produced by matching CFD predictions of the total pressure field at the throat of the inlet duct. Both the angle of attack and asymmetric distortion cases represent off-design flight conditions that may be encountered in a flight mission. The inlet duct was tested with and without a flow control technique at each flight condition to determine the effectiveness of the flow control technique at both design and off-design conditions. Finally, these data were used to predict the resulting stability margin in a compression system and the gain in stability margin with the addition of flow control.

The experimental testing for the three flight conditions without flow control revealed large total pressure losses at the top center of the AIP and moderate total pressure losses in the side regions of the AIP. These losses were predicted both through CFD studies and examination of the literature available. The total pressure loss is in the form of secondary flow created at each turn in the serpentine duct. Flow separation occurs in the uncontrolled case in the form of counter-rotating vortices which appear as total pressure losses at the AIP. The first turn in the duct produces flow separation in the uncontrolled case, but some dissipation occurs prior to the AIP. This results in the moderate total pressure loss in the side regions of the AIP. Flow separation also occurs

in the second turn of the serpentine duct producing additional secondary flow. There is very little dissipation of the secondary flow from the second turn of the inlet duct. This flow distortion is seen in the large total pressure deficit at the top center of the AIP in the uncontrolled cases.

The flow control technique used throughout this work targets the secondary flow created within the second turn of the serpentine duct. Microjets are used to create vortices in opposition to the vortices formed naturally within the duct. This flow control technique, developed by Lockheed Martin, was found to be successful, for all flight conditions tested, in eliminating the large total pressure deficit at the AIP created by the flow separation in the second turn. The off-design flight conditions resulted in larger regions of moderate total pressure loss. These losses are from the first turn of the inlet duct and are not affected by the addition of flow control. Therefore, the off-design flight conditions with flow control show large areas of moderate total pressure loss, but no region of large total pressure loss.

In comparing the off-design flight conditions with the design case, the off-design conditions result in lower total pressure recovery due to additional distortion. Because of the lower area-averaged total pressure recovery, the off-design conditions without flow control actually show more uniform flow, or less circumferential distortion. With flow control, the off-design conditions yield higher circumferential distortion than the design case but lower circumferential distortion than the same case without flow control. The extent of the circumferential distortion follows the same trend as the circumferential distortion intensity. Both circumferential distortion intensity and extent are directly proportional to loss in stability margin.

The radial distortion was decreased for the off-design cases but increased for the design case with the addition of flow control. The design case, with flow control, produces tip radial distortion. The MPR content increased with flow control, but the 1/rev and 2/rev harmonic coefficients were reduced. Therefore, the high cycle fatigue of the compression system will be reduced.

A parallel compressor model within DYNTECC was used to predict the change in stability margin for a compression system subjected to the experimentally determined total pressure losses at the AIP. The flight conditions without flow control showed a smaller stability range than the standard 180 degree 10% total pressure loss. Therefore, engine testing will need to include more severe distortion to determine compatibility with the inlet tested in this work. With the addition of flow control, the stability margin was improved and yielded a larger stable range than the 180 degree distortion case. This shows that additional engine testing and development will be necessary to ensure operation in a case where the flow control fails.

Finally, this research has provided the ability to simulate off-design flight conditions at an earlier design stage than was previously available. In addition, the conclusions regarding the gains in stability margin due to flow control emphasize the importance of a successful flow control technique. In the case studied throughout this research the flow control improves the flow to an acceptable level and allows the serpentine inlet duct to be used without compromising the flow quality at the engine fan face. These results encourage additional use of flow control as 1% of the inlet mass flow rate was used to realize a 55% improvement in stability margin for the design case.

6.2. Recommendations

As with any research, various directions for future research have been realized throughout this work. The effectiveness of the flow control technique in eliminating the distortion produced in the second turn of the inlet duct suggests that an attempt to correct the secondary flow which develops at the first turn of the inlet duct may prove successful. This work is in fact already underway at Lockheed Martin.

Wind tunnel testing will reveal more detailed information about the flow field at the off-design conditions simulated in this work. Flight testing will provide a more accurate description of this flow. These results, when available, should be used to verify the CFD predictions of this flow field and further validate the predictions used for the simulations in this work. This will help to improve early determination of inlet/engine compatibility.

As in any component testing, the results are incomplete until flight testing occurs. In many cases, it is desirable to directly connect adjacent components in an additional ground test setup. Direct coupling of the inlet duct and the gas turbine engine will allow a more complete understanding of the reduction in stability range for the compression system due to the serpentine inlet duct.

Questions are developing concerning the effect of swirl at the exit of a serpentine inlet duct and certainly research in this area will continue over the next several years. Swirl measurements can be taken at the AIP for various inlet ducts and flow control techniques. Similar to this research, off-design conditions may also be examined. In addition, engine testing will be required to determine how the swirl effects the gas turbine engine operation. Depending on the nature of the swirl, it may have very little impact on

the engine. However, the swirl could affect the stability range of the compression system and/or the life of the engine through cyclic fatigue. These concerns should be studied in more detail.

As ultra-compact, highly-offset, serpentine inlet ducts find their way onto tactical fighter aircraft, the off-design flight conditions will include higher angles of attack and sideslip. The inlet/engine system will need to be able to respond to such demands. Some possibilities include a more complex flow control technique which could adapt to changing flight conditions as well as to asymmetric flow. A circumferential variation in flow control level could feasibly correct the flow while using a minimal amount of bleed air. It is possible that alternative flow control techniques would be required to correct the flow.

7.0 References

Aeronautical Research Council, 1944, "Air Resistance of a Flat Plate of Very Porous Material," Reports and Memoranda of the Aeronautical Research Council, Number 2236.

Anderson, B.H., and Gibb, J., 1992, "Study on Vortex Generator Flow Control for the Management of Inlet Distortion," AIAA/SAE/ASME/ASEE 28th Joint Propulsion Conference and Exhibit, AIAA-92-3177.

Anderson, B.H., Huang, P.S., Paschal, W.A., and Cavatorta, E., 1992, "A Study on Vortex Flow Control of Inlet Distortion in the Re-Engined 727-100 Center Inlet Duct Using Computational Fluid Dynamics," AIAA 30th Aerospace Sciences Meeting and Exhibit, AIAA-92-0152.

Anderson, B.H., and Keller, D., 2002, "A Robust Design Methodology for Optimal Micro-Scale Secondary Flow Control in Compact Inlet Diffusers," 40th Aerospace Sciences Meeting and Exhibit, AIAA 2002-0541.

Anderson, R.E., 1983, "Aircraft Engine Inlet Pressure Distortion Testing in a Ground Test Facility," AIAA.

Baines, W.D. and Peteron, E.G., 1951, "An Investigation of Flow Through Screens," Transactions of the ASME, pp. 467-480.

Bansod, P., and Bradshaw, P., 1972, "The Flow in S-shaped Ducts," The Aeronautical Quarterly, Volume 23.

Beale, D.K., 2001, "Improving Information Productivity and Quality in Turbine Engine Ground Testing," 39th AIAA Aerospace Sciences Meeting and Exhibit, AIAA 2001-0163.

Campbell, Annette, 1981, "An Investigation of Distortion Indices for Prediction of Stalling Behavior in Aircraft Gas Turbine Engines," Master's Thesis, Virginia Tech.

Cousins, William, 2002, "Technique for the Development of Mechanical Limits," Internal Correspondence, Pratt & Whitney.

Cousins, W.T., Georges, M.J., and Rezaei, H, 2003, "Inlet Distortion Testing and Analysis of a High-Bypass Ratio Turbofan Engine," 16th International Symposium on Air-Breathing Engines (XVI ISABE), ISABE-2003-1110.

Dancy, Billy B., 1976, "Performance and Stalling Behavior of an Axial Flow Compressor with Circumferential Inlet Flow Distortion," Master's Thesis, Virginia Tech.

Davis, M., 1991, "Parametric Investigation into the Combined Effects of Pressure and Temperature Distortion on Compression System Stability," AIAA/SAE/ASME/ASEE 27th Joint Propulsion Conference, AIAA-91-1895.

Davis, M., Baker, W., Power, G., and Beale, D., 2002, "A Proposal for Integration of Wind Tunnel and Engine Test Programs for the Evaluation of Airframe-Propulsion Compatibility Using Numerical Simulations," Journal of Engineering for Gas Turbines and Power, Volume 124.

Davis, M., Baker, W., Power, G., and Beale, D., 1999 "A Proposal for Integration of Wind Tunnel and Engine Test Programs for the Evaluation of Airframe-Propulsion Compatibility Using Numerical Simulations," ASME International Gas Turbine and Aeroengine Congress and Exhibition, ASME 99-GT-345.

Davis, M., Hale, A., and Beale, D., 2001, "An Argument for Enhancement of the Current Inlet Distortion Ground Test Practice for Aircraft Gas Turbine Engines," 46th ASME International Gas Turbine and Aeroengine Technical Congress, ASME 2001-GT-0507.

Davis, M.W., Hale, A.A., Shahrokhi, K.A., and Garrard, G.D., 1995, "Euler Modeling Techniques for the Investigation of Unsteady Dynamic Compression System Behavior," 85th Meeting of the Propulsion and Energetics Panel of AGARD.

Doerffer, P.P, and Bohning, R., 2000, "Modelling of Perforated Plate Aerodynamic Performance," Aerospace Science Technologies 4, pp. 525-534.

Engineering Sciences Group, 1981, "Pressure Losses Across Orifice Plates, Perforated Plates and Thick Orifice Plates in Ducts," Engineering Sciences Data Item No. 81039.

Goldsmith, E.L., and Seddon, J., 1993, Practical Intake Aerodynamic Design, AIAA Education Series.

Guo, R.W., and Seddon, J., 1983, "The Swirl in an S-Duct Inlet of Typical Air Intake Proportions," Aeronautical Quarterly.

Hale, A., Chalk, J., Klepper, J., and Kneile, K., 1999, "Turbine Engine Analysis Compressor Code: TEACC – Part II: Multi-Stage Compressors and Inlet Distortion," 17th AIAA Applied Aerodynamics Conference, AIAA-99-3214.

Hale, A., and O'Brien, W., 1998, "A Three-Dimensional Turbine Engine Analysis Compressor Code (TEACC) for Steady-State Inlet Distortion," Journal of Turbomachinery, Volume 120, Number 3, pp. 422-430.

Hah, C., Rabe, D.C., Sullivan, T.J., and Wadia, A.R., 1996, "Effects of Inlet Distortion on the Flow Field in a Transonic Compressor Rotor," International Gas Turbine and Aeroengine Congress and Exhibition, ASME-96-GT-547.

Hamstra, J.W., Miller, D.N., Truax, P.P., Anderson, B.A., and Wendt, B.J., 2000, "Active Inlet Flow Control Technology Demonstration," 22nd International Council of the Aeronautical Sciences, ICA-6112.

Harper, D.K., 2000, "Boundary Layer Control and Wall-Pressure Fluctuations in a Serpentine Inlet," Master's Thesis, Virginia Polytechnic Institute and State University.

Jaw, L.C., Cousins, W.T., Wu, D.N., and Bryg, D.J., 2001, "Design and Test of a Semi-Passive Flow Control Device for Inlet Distortion Suppression," Journal of Turbomachinery, Volume 123, pp. 9-13.

Kramer, J., and Stanitz, J.D., 1952, "Two-Dimensional Shear Flow in a 90° Elbow," NACA Technical Note 2736, Lewis Flight Propulsion Laboratory.

Longley, J.P., Shin, H.W., Plumley, R.E., Silkowski, P.D., Day, I.J., Greitzer, E.M., Tan, C.S., and Wisler, D.C., 1994, "Effects of Rotating Inlet Distortion on Multistage Compressor Stability," ASME International Gas Turbine and Aeroengine Congress and Exposition, ASME 94-GT-220.

Mazzawy, R.S., 1977, "Multiple Segment Parallel Compressor Model for Circumferential Flow Distortion," Journal of Engineering for Power, pp. 288-296.

Oates, G.C., 1989, Aircraft Propulsion Systems Technology and Design, AIAA Education Series.

Odendaal, J.W., and Grygier, D., 2000, "RCS Measurements and Results of an Engine-Inlet System Design Optimization," IEEE Antennas and Propagation Magazine, Volume 42, Number 6, pp. 16-23.

Povinelli, L.A., and Towne, C.E., 1986, "Viscous Analyses for Flow Through Subsonic and Supersonic Intakes," AGARD Propulsion and Energetics Panel Meeting on Engine Response to Distorted Inflow Conditions.

Reichert, B.A., Hingst, W.R., and Okiishi, T.H., 1991, "An Experimental Comparison of Nonswirling and Swirling Flow in a Circular-to-Rectangular Transition Duct," 29th Aerospace Sciences Meeting, AIAA-91-0342.

Reichert, B.A., and Wendt, B.J., 1994, "Improving Diffusing S-Duct Performance by Secondary Flow Control," AIAA 32nd Aerospace Sciences Meeting and Exhibit.

Reichert, B.A., and Wendt, B.J., 1993, "An Experimental Investigation of S-Duct Flow Control Using Arrays of Low-Profile Vortex Generators," AIAA 31st Aerospace Sciences Meeting and Exhibit.

Reid, L. and Moore, R.D., 1978, "Performance of Single-Stage Axial-Flow Transonic Compressor With Rotor and Stator Aspect Ratios of 1.19 and 1.26, Respectively, and

With Design Pressure Ratio of 1.82," NASA Technical Paper 1338, Lewis Research Center.

Roach, P.E., 1986, "The Generation of Nearly Isotropic Turbulence Downstream of Streamwise Tube Bundles," International Journal of Heat and Fluid Flow, pp. 117-125.

Rowe, M., 1970, "Measurements and Computations of Flow in Pipe Bends," Journal of Fluid Mechanics, Volume 43 Part 4, pp.771-783.

SAE S-16 Committee, 1983, AIR 1419, "Inlet Total-Pressure-Distortion Considerations for Gas-Turbine Engines," Society of Automotive Engineers.

SAE S-16 Committee, 1978, ARP 1420, "Gas Turbine Engine Inlet Flow Distortion Guidelines," Society of Automotive Engineers.

SAE S-16 Committee, 2000, "Inlet Flow Angularity: A Current Assessment of the Inlet/Engine Swirl Distortion Problem," Society of Automotive Engineers.

SAE S-16 Committee, 1991, ARD50015, "A Current Assessment if Inlet/Engine Temperature Distortion," Society of Automotive Engineers.

SAE S-16 Committee, 1995, ARD50026, "A Current Assessment of Planar Waves," Society of Automotive Engineers.

Schetz, J.A., Pelletier, D., and Mallory, D.A., 1988, "Experimental and Numerical Investigation of a Propeller with Three-Dimensional Inflow," Journal of Propulsion and Power, Volume 4, Number 4, pp. 341-349.

Schlichting, H., 1955, Boundary-Layer Theory, McGraw Hill Book Company.

Schmid, N.R., Leinhos, D.C., and Fottner, L., 2001, "Steady Performance Measurements of a Turbofan Engine with Inlet Distortions Containing Co- and Counterrotating Swirl for an Intake Diffuser for Hypersonic Flight," Journal of Turbomachinery, Volume 123, pp. 379-385.

Seddon, J. and Goldsmith, E.L., 1999, Intake Aerodynamics Second Edition, AIAA Education Series.

Shahrokhi, K.A., 1995, "Application of a Modified Dynamic Compression System Model to a Low-Aspect Ratio Fan: Effects of Inlet Distortion," Master's Thesis, Vanderbilt University.

Sullerey, R.K., Mishra, S., and Pradeep, A.M., 2002, "Application of Boundary Layer Fences and Vortex Generators in Improving Performance of S-Duct Diffusers," Journal of Fluids Engineering, Volume 124.

Sullivan, J.P., Murthy, S.N.B., Davis, R., and Hong, S., 1982, "S-Shaped Duct Flows," Office of Naval Research Contract Number N-78-C-0710.

Taylor, A.M.K.P., Whitelaw, J.H., and Yianneskis, M., 1984, "Developing Flow in S-Shaped Ducts II – Circular Cross-Section Duct," NASA Contractor Report 3759.

Towne, C.E., 1984, "Computation of Viscous Flow in Curved Ducts and Comparison with Experimental Data," AIAA 22nd Aerospace Sciences Meeting, AIAA-84-0531.

Vahdati, M., Sayma, A.I., Breard, C., and Imregun, M., 2002, "Computational Study of Intake Duct Effects on Fan Flutter Stability," AIAA Journal, Volume 40, Number 3, pp. 408-418.

Vakili, A., Wu, J.M., Hingst, W.R., and Towne, C.E., 1984, "Comparison of Experimental and Computational Compressible Flow in a S-Duct," AIAA 22nd Aerospace Sciences Meeting, AIAA-84-0033.

Vakili, A.D., Wu, J.M., Liver, P., and Bhat, M.K., 1985, "Flow Control in a Diffusing S-Duct," AIAA Shear Flow Control Conference, AIAA-85-0524.

Vakili, A., Wu, J.M., Liver, P., and Bhat, M.K., 1983, "An Experimental Investigation of Secondary Flows in a S-Shaped Circular Duct," NASA Final Report NAG3-233.

Vakili, A., Wu, J.M., Liver, P., and Bhat, M.K., 1983, "Measurements of Compressible Secondary Flow in a Circular S-Duct," AIAA 83-1739.

Wellborn, S.R., 2000, "Active Control of Compressor Bleed Flows," NASA Contract NAS3-98003, Task Order #7, Monthly Technical Progress Report No. 4.

Wellborn, S.R., Reichert, B.A., and Okiishi, T.H., 1992, "An Experimental Investigation of the Flow in a Diffusing S-Duct," AIAA/SAE/ASME/ASEE 28th Joint Propulsion Conference and Exhibit, AIAA-92-3622.

Wendt, B.J., 1999, "Advanced Inlet Flow Control Test Program," Test requirements document, NASA Lewis Research Center.

Wendt, B.J., and Reichert, B.A., 1996, "Vortex Ingestion in a Diffusing S-Duct Inlet," Journal of Aircraft, Volume 33, Number 1.

Appendix A: Uncertainty Analysis

As with all experimental work, there is uncertainty in the data acquisition process and the resulting calculations. In this work, the total pressure measurements for the AIP total pressure data and the static pressure measurements for the Mach number calculation were acquired using two Scanivalve DSA 3017 with 0-5 psid transducers. The accuracy of the transducers is reported as 0.05% full scale, or 0.0025psid.

The Mach number is calculated using:

$$M = \sqrt{\left(\frac{2}{\gamma - 1}\right)\left[\left(\frac{P_o}{P}\right)^{(\gamma-1)/\gamma} - 1\right]}$$

The uncertainty in the Mach number can then be found using propagation of uncertainty:

$$u_M = \sqrt{\left[\frac{\partial M}{\partial P_o} * u_{P_o}\right]^2 + \left[\frac{\partial M}{\partial P} * u_P\right]^2}$$

Using propagation of uncertainty, the Mach number uncertainty is 0.000461.

Additional measurements were required for the mass flow injection rate. Because the mass flow injection rate was controlled using a closed loop control system, the uncertainty presented here is based on experimental repeatability results. There is also uncertainty due to the measurement devices themselves. The experimental repeatability yields an uncertainty of 0.05598 lbm/s.

Vita

Angela C. Rabe

Angela C. Rabe was born on January 28, 1978 in Dayton, OH to Douglas and Darlene Rabe. She attended Carroll High School in Dayton, Ohio graduating valedictorian in 1996. She graduated *Summa Cum Laude* from Virginia Tech in May 2000 with a Bachelor of Science in Mechanical Engineering. The author has accepted a position as an Associate Aerospace Engineer with the Air Force Research Laboratory at Wright-Patterson Air Force Base in Fairborn, OH.